REPORT DOCUMENTATION PAGE

Form Approved
OMB No 0704-0188

1. AGENCY USE ONLY (Leave blank)	2. REPORT DATE	3. REPORT TYPE AND DATES COVERED
	8 Dec 95	Final 1 Oct 91 - 14 May 95

4. TITLE AND SUBTITLE

A FUNDAMENTAL STUDY OF THE FIELD COMPRESSOMETER TEST

5. FUNDING NUMBERS

G-AFOSR 91-0424

6. AUTHOR(S)

S. Banerjee and R D. Holtz

7. PERFORMING ORGANIZATION NAME(S) AND ADDRESS(ES)

Department of Civil Engineering
Box 352700
University of Washington
Seattle, Washington 9895-2700

8. PERFORMING ORGANIZATION REPORT NUMBER

N/A

9. SPONSORING / MONITORING AGENCY NAME(S) AND ADDRESS(ES)

Department of the Air Force
Air Force Office of Scientific Research
Bolling Air Force Base, D.C. 20332-0001

NA

10. SPONSORING / MONITORING AGENCY REPORT NUMBER

AFOSR - 91-0424

11. SUPPLEMENTARY NOTES

12a. DISTRIBUTION / AVAILABILITY STATEMENT

Approved for public release,
distribution unlimited

19960618 015

13. ABSTRACT (Maximum 200 words)

The project consisted of both theoretical and experimental research components. The theoretical research involved the development of a simple elasto-plastic constitutive model based on incremental plasticity and double-hardening concepts to model the behavior of geomaterials. The model has been tested under general loading conditions and has reproduced experimental results reasonably well. It has also been implemented in a finite element program to facilitate the analysis of practical soil-structure interaction problems such as the screw-plate compressometer (SPC) test. An optimization scheme has been developed to aid in parameter identification.

Significant improvements in the test equipment and experimental procedures were made in order to take advantage of the SPC''s full potential. Initial laboratory work indicated that the use of small load increments and low strain levels provided useful data for interpreting soil response to buried circular plates similar to the field compressometer. Proof testing indicated that the new drill rods and a tension cable reference system performed very well, and installation was much simpler and faster than previously. The deformation measuring system was improved. The interaction of the drilling rods with the surrounding soil was an important factor in prototype field SPC testing. Soil stiffness and strength was found to control the load reaching the plate, and the stiffness of the soil controlled plate deformations. The load to the plate generally varied with time, depending on the rate of deformation and the relative stiffness of the various soil components. The use of friction reducers or drilling mud may reduce, but not entirely eliminate, the effect of friction. Such methods would also complicate the test.

14. SUBJECT TERMS	15. NUMBER OF PAGES
Screw plate, compressometer, in situ tests, constitutive models, granular soils, double hardening, elsto-plastic model	117
	16. PRICE CODE

17. SECURITY CLASSIFICATION OF REPORT	18. SECURITY CLASSIFICATION OF THIS PAGE	19. SECURITY CLASSIFICATION OF ABSTRACT	20. LIMITATION OF ABSTRACT
U	U	U	

NSN 7540-01-280-5500

Standard Form 298 (Rev 2-89)
Prescribed by ANSI Std Z39-18
298-102

DTIC QUALITY INSPECTED 1

Final Technical Report

on

A FUNDAMENTAL STUDY OF THE FIELD COMPRESSOMETER TEST

to

U.S. Air Force
Office of Scientific Research

Grant No. AFOSR 91-0424

by

S. Banerjee and R. D. Holtz
Department of Civil Engineering
University of Washington
Seattle, Washington

8 December 1995

Final Technical Report

on

A FUNDAMENTAL STUDY OF THE FIELD COMPRESSOMETER TEST

to

U.S. Air Force
Office of Scientific Research

Grant No. AFOSR 91-0424

by

S. Banerjee and R. D. Holtz
Department of Civil Engineering
University of Washington
Seattle, Washington

8 December 1995

Statement of Work

The project consists of both theoretical and experimental research components. The theoretical research involves the development of the numerical solutions to the boundary value problem and the data interpretation procedures. The experimental component includes possible improvements of the test apparatus and the instrumentation system and generating, under controlled laboratory conditions as well as field conditions, appropriate data for verification and evaluation of the identification procedures for the soil parameters.

The major tasks to be performed in order to complete the theoretical portion of the study include: a) improvement and refinement of the constitutive model, b) assessment and verification of the model, c) incorporation of the model into a numerical analysis scheme, d) solving the screw plate test problem as a boundary-value problem, and e) developing interpretation procedures for screw plate test results. Significant improvements in the test equipment, experimental procedures and interpretation of results need to be made in order to take advantage of the SPC's full potential. The primary improvements to be made to the test equipment and procedures involve: a) measurement of force at the elevation of the plate, b) improvement of the instrumentation for measurement of deformation and settlement of the plate so that digital signals can be utilized in a PC-based data acquisition system, c) measurement of induced pore water pressure on the plate, d) evaluation of the shape of the screwplate analytically and experimentally, e) incorporation of modern signal transmission systems for acquiring data from the transducers located on or near the plate.

List of Publications

The project generated several archival publications:

Banerjee, S., Davis, R. O, and Sribalaskandrajah, K (1992) "A Simple Double-Hardening Model for Granular Soils," Journal of Geotechnical Engineering, ASCE, Vol 118, No. 6, pp. 889-901.

Miller, G. R., Banerjee, S., and Sribalaskandarajah, K. (1992) "Interactive Analysis of Evolving Earth Structures," Proceedings of Fourth International Symposium on Numerical Methods in Geomechnics (NUMOG IV), Swansea, pp. 567-576.

Banerjee, S., and Sribalaskandarajah, K. (1994) "An Alternative Formulation for Volume Change Behavior," in Vertical and Horizontal Deformations of Foundations and Embankments, Proceedings of Settlement '94, Geotechnical Special Publication No. 40, Vol. 1, pp. 652-662.

Miller, G. R., Banerjee, S., and Sribalaskandarajah, K. (1995) "A Framework for Interactive Analysis for Computational Geomechnics," Computers and Geotechnics, Vol. 17, No. 1, pp. 17-37.

Sribalaskandarajah, K., and Banerjee, S. (1995) "An Improved Double-Hardening Model for Geomaterials," Journal of Geotechnical Engineering, ASCE, (submitted for publication).

Banerjee, S., and Sribalaskandarajah, K. (1996) "Volume-Change Relations of Soils," in preparation for submission to Journal of Geotechnical Engineering, ASCE.

Others are likely to be prepared from:

Sribalaskandarajah, K. (1996) "A Computational Framework for Dynamic Soil-Structure Interaction Analysis," PhD thesis, University of Washington (in preparation).

List of Personnel

The professional involved in the current research are:

Prof. S. Banerjee, University of Washington

Prof. R. D. Holtz, University of Washington

Mr. K. Sribalaskandarajah, PhD-candidate, University of Washington

Mr. J. Strout, PhD-candidate, NTH, Trondheim, Norway,
formerly at University of Washington

Contents of First Annual Technical Report (September 1992)

1. Screw Plate Compressometer Test -- Literature Review
2. Soil-Structure Interaction Analysis
3. Preliminary Experimental Results

Contents of Second Annual Technical Report (September 1993)

1. Double-Hardening Model for Cyclic Behavior of Soils
2. Development of a Prototype Field Compressometer Design and Preliminary Laboratory Results

Contents of this Final Technical Report (December 1995)

1. Study of Field Compressometer
2 An Improved Double-Hardening Model for Geomaterials
3. Prototype Field Compressometer

Study of Field Compressometer

by

K. Sribalaskandarajah

Introduction

As outlined in the previous interim reports, the understanding of the load-deformation behavior of soil as well as the interface between soil and the screw plate is essential in the study of field compressometer tests. In order to address these issues, a general elasto-plastic soil constitutive model (Sribalaskandarajah and Banerjee, 1995) has been developed and implemented in a new finite element program (Sribalaskandarajah, 1995) developed to model soil-structure interaction problems.

The new constitutive model for geomaterials proposed in this study is based on non-associative elasto-plastic "double hardening" concepts. The model employs two distinct yield functions, namely shear and volumetric, each describing the volumetric and shear mechanisms respectively, leading to a simple but general model. The number of model parameters is small, as compared to most of the general constitutive models, and these parameters are physically meaningful. A detailed description of the proposed model is presented in the paper (Sribalaskandarajah and Banerjee, 1995) and in the earlier related publications by the authors (Banerjee, Davis and Sribalaskandarajah, 1992; Banerjee and Sribalaskandarajah, 1994). The manuscript of the later paper (Sribalaskandarajah and Banerjee, 1995) is appended to this report.

The development of the finite element program (Sribalaskandarajah, 1995) mentioned above, utilizes object-oriented programming techniques in its development. This program has been developed with general dynamic soil-structure interaction problems in mind. As the primary purpose of the development of this program was the demonstration of the object-oriented programming applications in geomechanics, the element library currently available is not quite complete. Therefore, the analyses presented in this report are performed using plane strain elements instead the customary axisymmetric elements. Linear elastic and elasto-plastic Drucker-Prager constitutive models as well as the proposed

new model are incorporated in this analysis program. Also, the program is equipped with interface elements.

Numerical Modeling of Screw Plate Tests

In modeling of screw plate test, the screw has been tacitly assumed to be a flat plate, neglecting the three dimentional nature of the screw. The lack of good general three dimensional soil models also necessitates this assumption. However, the model we have developed is for general three dimensional loading conditions, and the finite element program also was developed for general three-dimensional elements. However, as mentioned earlier the element library is not that complete. Therefore, we will limit the analyses presented in this report to two-dimensional cases.

Figure 1 depicts a screw plate in experimental conditions. In the following analyses, it was assumed that the screw plate and the soil entrapped in the screw form an elastic composite. Assuming typical elastic properties for sand(E=10 MPa, ν=0.3, ρ=2000.0 kg/m^3) and steel(E=200 GPa, ν=0.3, ρ=7750.0 kg/m^3), and typical dimensions for the screw plate(diameter=300mm, pitch=60m, thickness of the plate=5mm), the elastic properties of the composite materials(E=10,910 MPa, ν=0.3, ρ=2480.0 kg/m^3) are determined. The vertical deformation of the screw plate subjected to the load pattern depicted in Figure 2, has been presented in the following analyses. Both linear elastic and the proposed elasto-plastic model were used in the analysis. The analyses were repeated with interface elements with a simple interface constitutive model(shear modulus=380 kPa) in either case. The damping in the structure is assumed to be of the Rayleigh damping type given by

$$C = \alpha_c M + \beta_c K \tag{1}$$

where, α_c and β_c are material constants. In this analysis, the values of these constants(α_c=0.0; β_c=.03) were chosen to reflect the realistic time-displacement behavior of the screw-plate test results.

In the linear elastic analysis, the half-space material is assumed to be linear elastic with typical elastic properties(E=10 MPa, ν=0.3, ρ=2000.0 kg/m^3). Figure 3 depicts the deformed shape of the mesh with perfect bonding between the plate and the sand. The deformed shape of the mesh with interface elements is being depicted in figure 4. Figure 5a presents the displacement-time history of the

screw plate and Figure 5b presents the load-displacement plot for the soil with particular properties.

In analyzing the problem with the elasto-plastic model proposed, the properties of the composite material are assumed to be same as used in the above analysis. Only the properties of the halfspace material are assumed to be inelastic(p_a=100 kPa; G_o=3.8 MPa; K_o=8.3 MPa; M_c=1.35; M_p=1.5; α=0.0515; β=1.0; ζ=1.0; e_o=0.7; e_{min}=0.55). The figure 6 presents the displacement time history of the screw plate as well as the load-displacement plot of the soil.

In summary, a simple elasto-plastic constitutive model based on incremental plasticity and double-hardening concepts has been developed to model the behavior of geomaterials. This model has been tested under general loading conditions and has reproduced experimental results reasonably well (Sribalaskandarajah and Banerjee, 1995). This model has also been implemented in a finite element program (Sribalaskandarajah, 1995) to facilitate the analysis of practical soil-structure interaction problems such as screw-plate tests.

References

Banerjee, S., Davis, R. O. and Sribalaskandarajah, K. (1992). Simple double-hardening model for geomaterials, *Journal of Geotechnical Engineering* **118**(6): 889–901.

Banerjee, S. and Sribalaskandarajah, K. (1994). An alternative formulation for volume-change behavior of soils, *in* A. T. Yeung and G. Y. Félio (eds), *Vertical and Horizontal Deformations of Foundations and Embankments; Proceedings of Settlement '94, Texas*, Vol. 1, ASCE, pp. 652–662. Geotechnical Special Publication No. 40.

Sribalaskandarajah, K. (1995). *A Computational Framework for Dynamic Soil-Structure Interaction Analysis(under preparation)*, PhD thesis, University of Washington.

Sribalaskandarajah, K. and Banerjee, S. (1995). An improved double-hardening model for geomaterials(submitted for publication), *Journal of Geotechnical Engineering* .

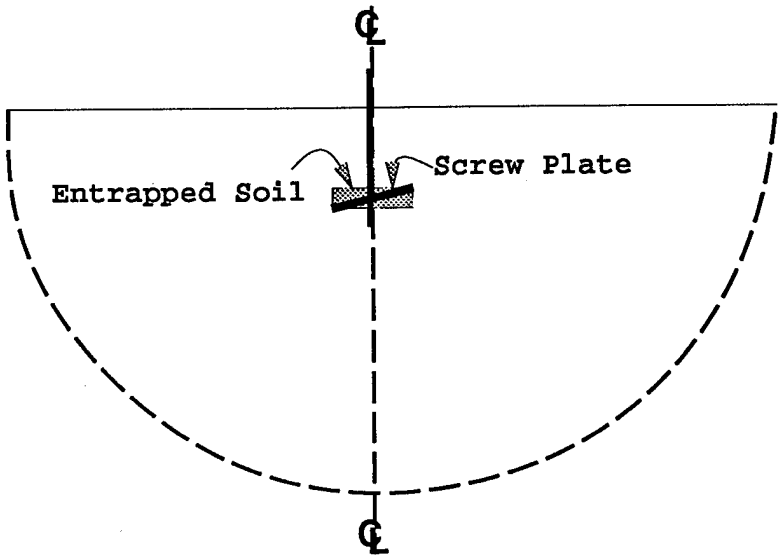

FIGURE 1: Screw Plate

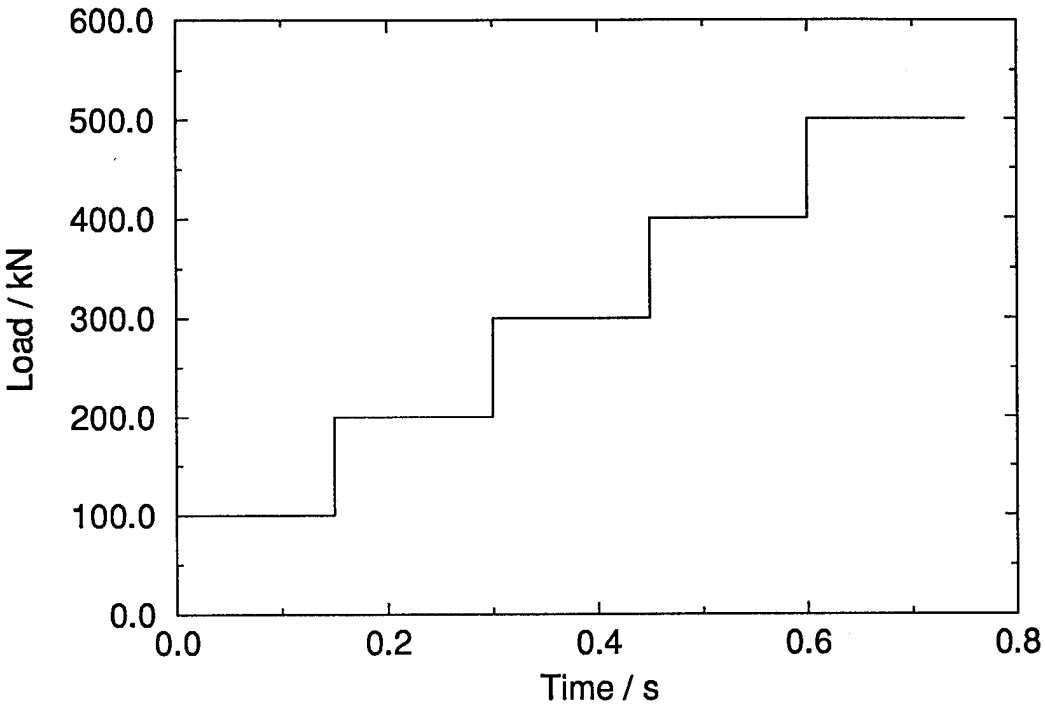

FIGURE 2: Load on Screw Plate

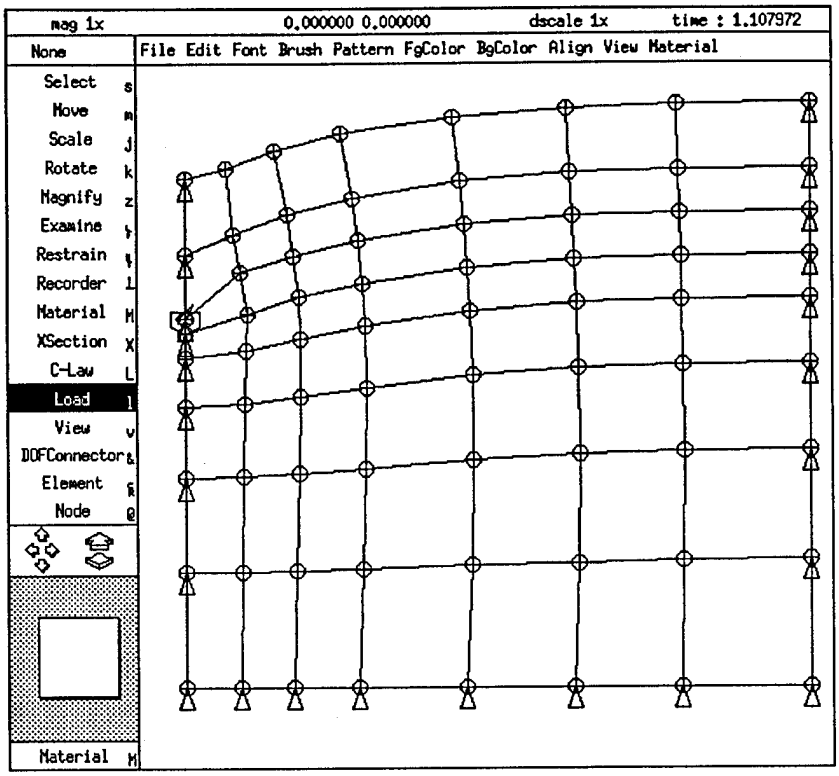

FIGURE 3: Deformed mesh under Screw-Plate loading with perfect bonding

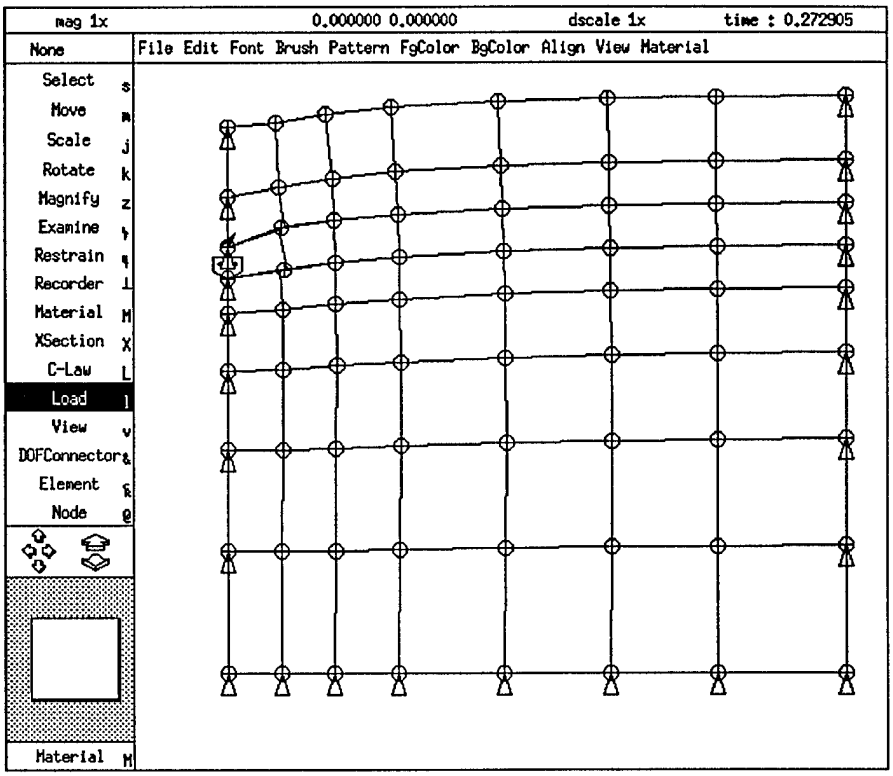

FIGURE 4: Deformed mesh under Screw-Plate loading with interface elements

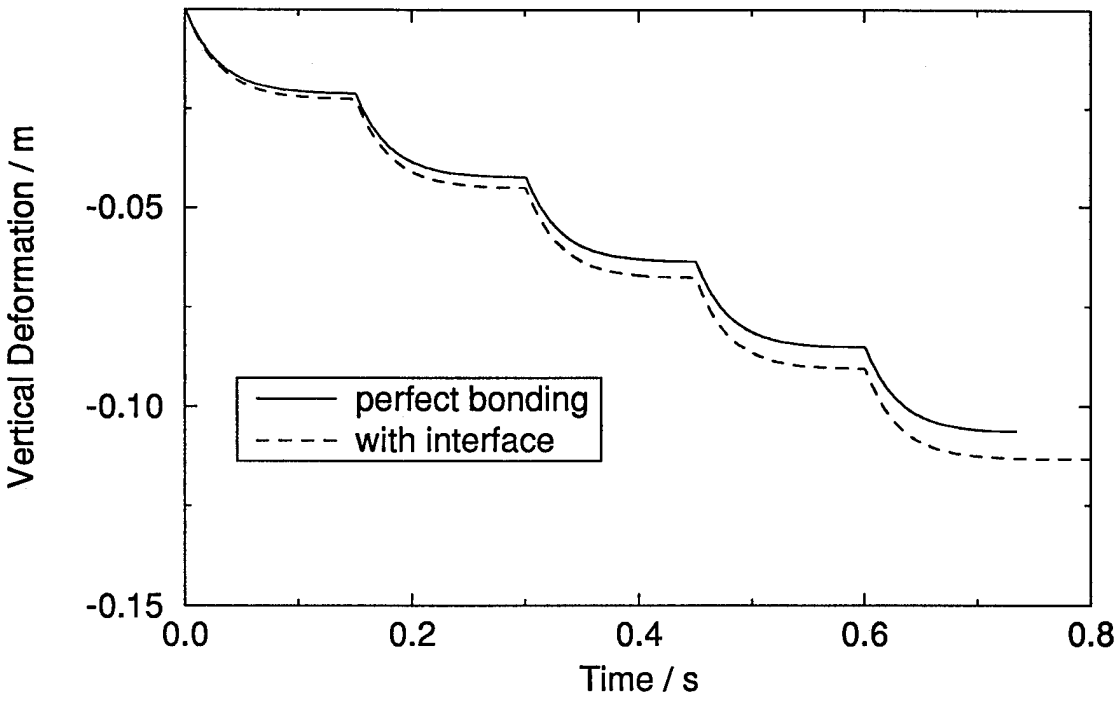

(A) Time-Settlement curve

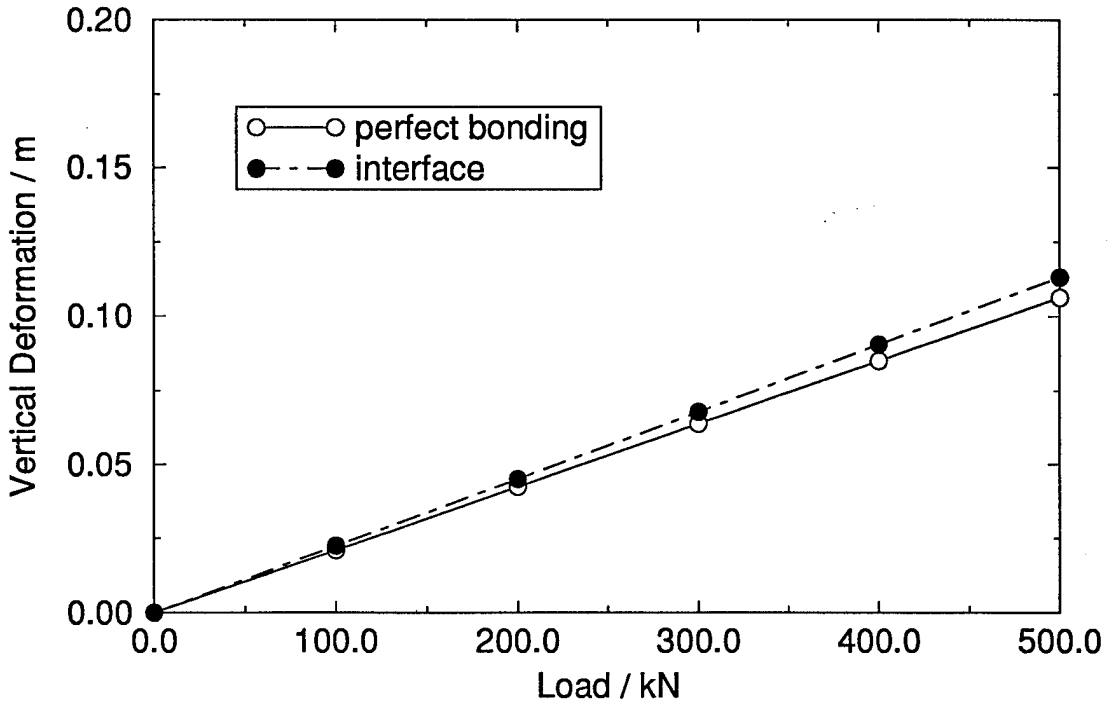

(B) Load-Settlement curve

FIGURE 5: Vertical displacement of the Screw Plate with linear elastic soil model

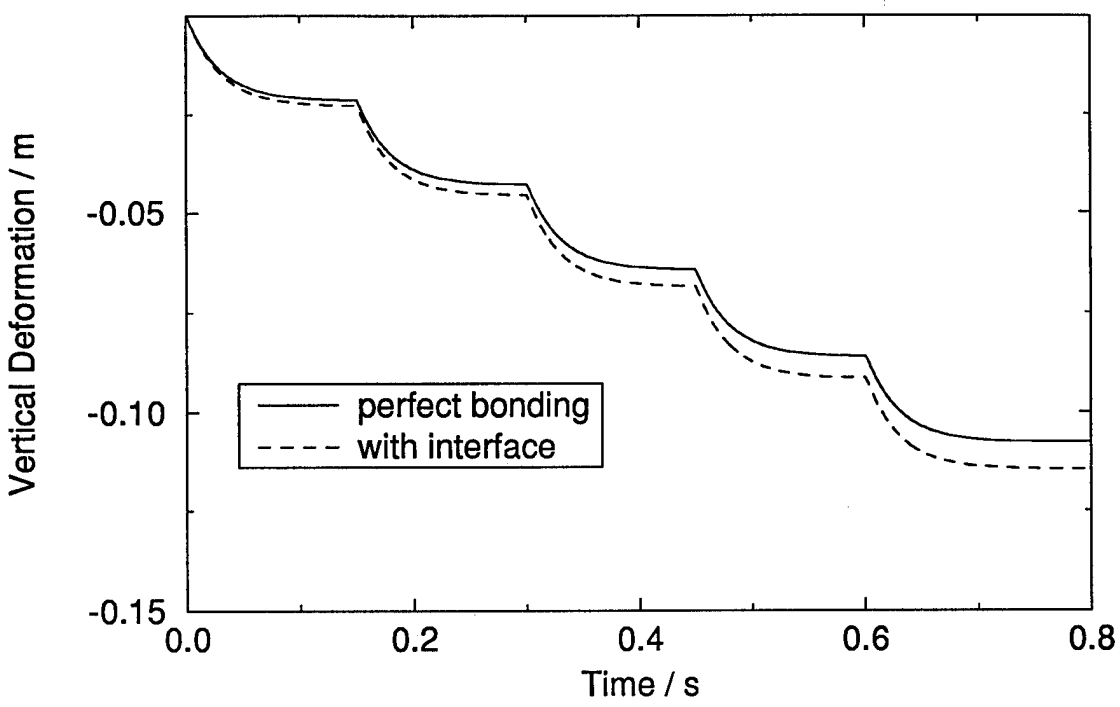

(A) Time-Settlement curve

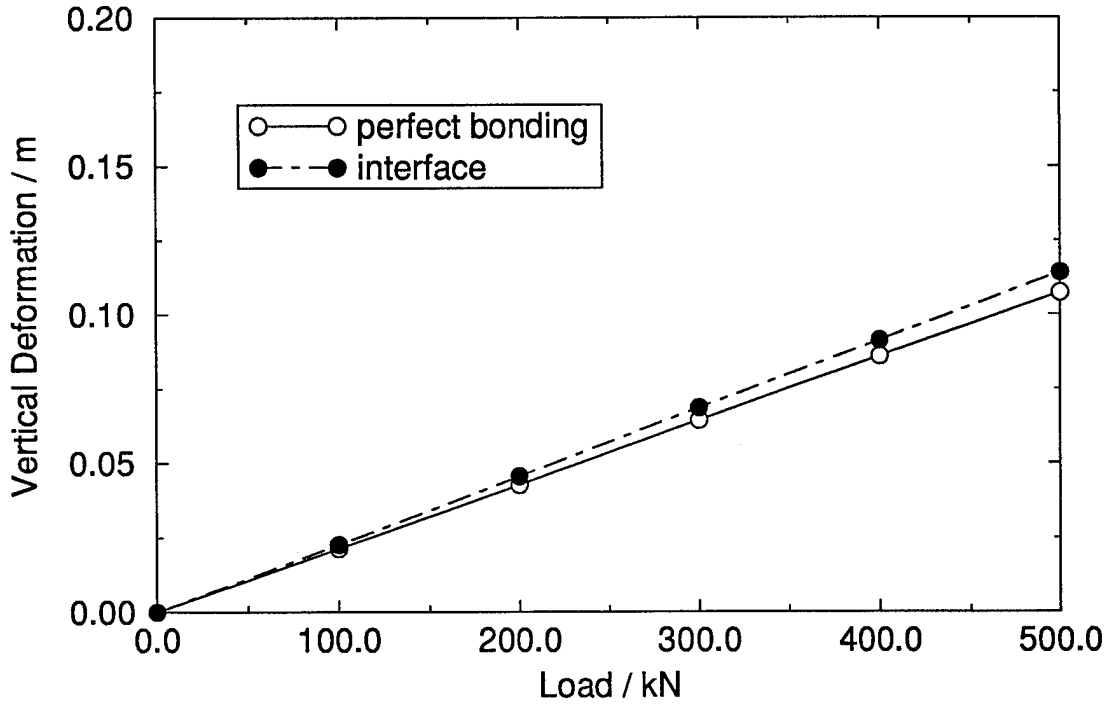

(B) Load-Settlement curve

FIGURE 6: Vertical displacement of the Screw Plate with non-linear elasto-plastic soil model

An Improved Double-Hardening Model for Geomaterials

By

Kandiah Sribalaskandarajah[1], Student Member, ASCE,

and

Sunirmal Banerjee[2], Member, ASCE

Abstract

This paper describes an advanced version of the model previously proposed by the authors. While the prior version of the model was shown to work for monotonic loading only, the proposed version is general enough to include any arbitrary loading conditions. The details of the model formulation, and the numerical performance of the model for both monotonic and cyclic loading tests have been presented. It is shown that experimental results can be adequately reproduced by the present model. Finally, a short description of the parameter identification based on optimization schemes is also included.

Introduction

A wide variety of macroscopic plasticity models have attempted to address the various complex aspects of the material behavior by incorporating more and more involved mathematical techniques. The capabilities of the models have been greatly enhanced by including concepts such as bounding and loading surfaces by Dafalias and Popov (1975), subloading surfaces by Hashiguchi (1986), kinematic and mixed hardening rules, nonassociated flow rules by Mroz and Pietruszczak (1983, 1983). None of these approaches were simple enough for the readers to be easily understood and implemented in their numerical schemes. The present approach is based on the multiple yield mechanisms originally proposed by Koiter (1953) and is an extension of the previous version proposed by the authors. Similar models which had used Koiter's generalized approach were mentioned in that paper (Banerjee, Davis & Sribalaskandarajah 1992). The present paper shows how it has been possible to extend the previous model to include any arbitrary loading response herein.

[1]Grad. Res. Asst., 233 More Hall, Dept. of Civil Engrg., Univ. of Washington, Box 352700, Seattle, WA 98195-2700
[2]Prof., Civ. Engrg., 233 More Hall, Dept. of Civil Engrg., Univ. of Washington, Box 352700, Seattle, WA 98195-2700

A Double-Hardening Model for Geomaterials

Preliminaries

The effective stress tensor is denoted by σ_{ij} and the strain tensor by ϵ_{ij}. The invariants of the effective stress tensor are denoted by

$$\begin{aligned} J_1 &= \sigma_{ii} \\ J_2 &= \frac{1}{2}(J_1^2 - \sigma_{ik}\sigma_{kj}) \\ J_3 &= \frac{1}{6}(2\sigma_{ij}\sigma_{jk}\sigma_{ki} - 3J_1\sigma_{ij}\sigma_{ji} + J_1^3) \end{aligned} \tag{1}$$

The invariants of the strain tensor, defined in a similar manner, are denoted by I_1, I_2, and I_3. The deviatoric effective stress tensor is denoted as $s_{ij}(= \sigma_{ij} - \frac{J_1}{3}\delta_{ij})$, the deviatoric strain tensor is denoted as $e_{ij}(= \epsilon_{ij} - \frac{I_1}{3}\delta_{ij})$, and the invariants of the deviatoric stress tensor are denoted as

$$\begin{aligned} J_1' &= s_{ii} = 0 \\ J_2' &= \frac{1}{2}s_{ij}s_{ji} \\ J_3' &= \frac{1}{3}s_{ij}s_{jk}s_{ki} \end{aligned} \tag{2}$$

The yield and potential functions are functions of stress and are conveniently viewed in the principal stress space(Figure 1). As shown in Figure 1a, the Space Diagonal, also known as the hydrostatic axis, is oriented at equal angles to the three principal stress axes. Any plane that is perpendicular to the space diagonal is called a deviatoric plane (Figure 1b) and the deviatoric plane that passes through the origin is known as the π-plane.

For an arbitrary state of stress given by the principal stress values, σ_1, σ_2, and σ_3, the projection of the stress vector on the hydrostatic axis is called the mean effective stress or octahedral normal stress, $\sigma_m(= \frac{J_1}{3})$. The projection of the stress vector on the deviatoric plane is given by the vector $\langle s_1, s_2, s_3 \rangle$; where, s_1,s_2, and s_3 are the components of the deviatoric principal stress tensor. The magnitude of this projection is called octahedral shear stress and is given by $\sqrt{2J_2'}$. In the Figure 1, the angle θ between the major principal axis and the stress vector on the deviatoric plane is known as the Lode angle and

is related to the invariants by

$$\cos(3\theta) = \frac{3\sqrt{3}J_3'}{2(J_2')^{3/2}} \tag{3}$$

Strain Decomposition

In the incremental theory of elasto-plasticity, it is assumed tacitly that the total strain increment, $d\epsilon_{ij}$, due to any stress increment, $d\sigma_{ij}$, can be decomposed into a reversible(elastic) component, $d\epsilon_{ij}{}^e$, and an irreversible(plastic) component, $d\epsilon_{ij}{}^p$, i.e.

$$d\epsilon_{ij} = d\epsilon_{ij}{}^e + d\epsilon_{ij}{}^p \tag{4}$$

These elastic and plastic incremental strain components are discussed individually next in detail.

Elastic Strains

In general, soils exhibit predominantly plastic strains and thus it is sufficient to employ a simple linear isotropic elastic constitutive law, such as isotropic Hooke's law, to describe the elastic behavior of the material without losing much accuracy. Employing isotropic Hooke's law implies that the elastic strains are not coupled, i.e., the changes in elastic distortional stress do not affect the elastic volumetric strain and the change in elastic volumetric stress does not affect the elastic distortional strains. Thus the elastic shear strains as well as the elastic volumetric strain could be expressed as

$$de_{ij}{}^e = \frac{ds_{ij}}{2G} \tag{5}$$

$$d\epsilon_{ii}{}^e = \frac{d\sigma_{ii}}{3K} \tag{6}$$

where G is the elastic shear modulus and K is the elastic bulk modulus. According to the findings of Hardin and Drenevich (1972), the elastic shear modulus varies with a power of mean effective principal stress, $\sigma_m = \frac{\sigma_{ii}}{3}$. Although the shear modulus is traditionally defined by the secant shear modulus of the soil, the elastic shear modulus could be approximated by the initial tangent modulus, which is also the initial secant modulus. Therefore the elastic shear modulus should conform to the findings of Hardin and Drenevich:

$$G = G_o(\frac{\sigma_m}{\sigma_a})^{1-\beta} \tag{7}$$

in which σ_a is the atmospheric pressure; β is a material constant; and G_o is the reference value of shear modulus when $\sigma_m = \sigma_a$.

For a linear elastic material, the shear modulus and the bulk modulus are related by Poisson's ratio. Therefore, it is reasonable to expect the value of the Bulk modulus to have a similar variation with the mean effective principal stress as that of the Shear Modulus. Recently, in an attempt to describe the volume-change behavior of the isotropic swelling of soils, Banerjee and Sribalaskandarajah (1994) have shown that the bulk modulus, B, can be assumed to vary in a similar manner as in equation (7). This volume change behavior is usually assumed to be purely elastic, therefore the elastic bulk modulus could be expressed as a function of mean effective principal stress, σ_m, as

$$K = K_o(\frac{\sigma_m}{\sigma_a})^{1-\zeta} \tag{8}$$

where K_o is the reference value of bulk modulus when $\sigma_m = \sigma_a$, and ζ is a material constant.

Plastic Strains

The concept of "the theory of plastic potential", which assumes the existence of a single yield mechanism, was subsequently generalized by Koiter (1953) to include multiple yield mechanisms. If there are n such mechanisms and the associated yield functions as well as the potential functions are denoted by $F_k(s_{ij}) = 0, k = 1, n$ and $G_k(s_{ij}) = 0, k = 1, n$ respectively, then the plastic strain increments can be written as

$$d\epsilon_{ij}{}^p = \sum_{k=1}^{n} C_k H_k \frac{\partial G_k}{\partial \sigma_{ij}} \frac{\partial F_k}{\partial \sigma_{lm}} d\sigma_{lm} \tag{9}$$

where H_k is a nonnegative scalar function of stress, plastic strain, and strain history and C_k is a constant taking a value of "one" during the loading while taking a value of "zero" during the unloading.; i.e.

$$\left.\begin{array}{llll} C_k = 0 & F_k < 0 & \text{or} & \frac{\partial F_k}{\partial \sigma_{ij}} d\sigma_{ij} < 0 \\ C_k = 1 & F_k = 0 & \text{and} & \frac{\partial F_k}{\partial \sigma_{ij}} d\sigma_{ij} \geq 0 \end{array}\right\} \tag{10}$$

In soil plasticity studies, Prevost and Hoeg (1975) employed this concept with two separate yield mechanisms to describe the volumetric and shear behaviors of the soil. For such a model, which is

also known as "double hardening model", equation (9) can be written as the

$$d\epsilon_{ij}^{p} = C_v H_v \frac{\partial G_v}{\partial \sigma_{ij}} dF_v + C_d H_d \frac{\partial G_d}{\partial \sigma_{ij}} dF_d \tag{11}$$

where the subscript v is used to denote the volumetric mechanism, and the subscript d is used to denote the shear mechanism. Figure 2 shows the yield functions and potential functions for both mechanisms used in this study. The mathematical forms of these functions are outlined below.

Shear Yielding

The yield function for the shear mechanism is assumed to be given by

$$F_d = s_\eta(\eta - \eta_d) \tag{12}$$

where η_d is a constant describing the nature of the hardening, s_η is a parameter denoting the sign of $d\eta$, and η is the stress ratio defined in terms of the stress invariants as

$$\eta = s_\pi \frac{3\sqrt{3J_2'}}{J_1} \tag{13}$$

where s_π is the sign of the third deviatoric stress invariant J_3' and the value of $d\eta$ is

$$d\eta = \eta \left[\frac{dJ_2'}{2J_2'} - \frac{dJ_1}{J_1} \right] \tag{14}$$

In view of equation 12 and by the definition of s_η, it can be seen that the value of $\frac{\partial F_d}{\partial \sigma_{ij}} d\sigma_{ij}$ is always non-negative and therefore "unloading" is undefined in this mechanism. Therefore, the choice of yield function ensures that this mechanism always induces plastic strains whenever there is a change in η, i.e.

$$C_d = 1.0 \qquad \text{for any } d\eta \tag{15}$$

The flow potential function of the shear mechanism, G_d, is assumed to be of the following form

$$G_d = s_\eta \, \eta + M_c(\theta) \, \ln\left(\frac{J_1}{(J_1)_d} \right) = 0 \tag{16}$$

where, $(J_1)_d$ is a constant and M_c is the absolute value of the ultimate stress ratio, i.e.

$$M_c = |\eta|_{ultimate} \tag{17}$$

For the special case of triaxial conditions, the potential function given by equation 16 becomes identical to the yield function used in the original Cam-Clay model (Roscoe, Schofield & Wroth 1958). Also, the shape of the potential function depends on the direction of loading and the state of stress. This is illustrated in Figure 3a for a cyclic triaxial compression test. The stress path is shown as the solid straight line and the evolution of the potential function is depicted for states of stress marked on the stress path. The potential function is concave downward when $d\eta > 0$ and concave upward when $d\eta < 0$.

The parameter M_c is, in general, a function of Lode angle, θ, and thus describes the anisotropic behavior of the soil. In order to study the variation of the parameter M_c with respect to Lode Angle, the failure criterion proposed by Matsuoka and Nakai (1974) is closely examined, because this failure function was derived by considering the mechanical aspects of the shearing mechanism. It is expressed as

$$\frac{J_1 J_2}{J_3} = c \tag{18}$$

where, c is a material constant. In view of equation (17) and by the definition of η, the value of M_c can be expressed in terms of the stress ratio at failure, η_f as

$$M_c = s_\eta \, \eta_f \tag{19}$$

Therefore, in view of the definitions of stress ratio and Lode Angle, equation (18) could be expressed in terms of M_c as

$$c = \frac{27(9 - M_c^2)}{2 s_\pi \, s_\eta \cos(3\theta) M_c^3 - 9 M_c^2 + 27} \tag{20}$$

The above equation can be used to estimate the value of c from the value of the parameter M_c. By rearranging we arrive at a cubic equation for M_c in terms of θ as

$$2 s_\pi \, s_\eta \, c \cos(3\theta) M_c^3 - 9(c-3) M_c^2 + 27(c-9) = 0 \tag{21}$$

By taking derivatives with respect to θ, equation (21) can be rearranged as

$$\frac{\partial M_c}{\partial \theta} = \frac{s_\pi \, s_\eta \, c M_c^2 \sin(3\theta)}{[s_\pi \, s_\eta \, c M_c \cos(3\theta) - 3(c-3)]} \tag{22}$$

Further, from the definitions of Lode angle, θ, the partial derivative of θ with respect to σ_{ij} can be expressed as

$$\frac{\partial \theta}{\partial \sigma_{ij}} = \frac{\cot(3\theta)}{3}\left[\frac{3}{2J_2'}s_{ij} - \frac{1}{J_3'}(s_{ik}s_{kj} - \frac{2}{3}J_2'\delta_{ij})\right] \tag{23}$$

From equation (22) and equation (23), we get

$$\frac{\partial M_c}{\partial \sigma_{ij}} = \frac{s_\pi \, s_\eta \, c M_c^2 \cos(3\theta)}{3\,[s_\pi \, s_\eta \, c M_c \cos(3\theta) - 3(c-3)]}\left[\frac{3}{2J_2'}s_{ij} - \frac{1}{J_3'}\left(s_{ik}s_{kj} - \frac{2}{3}J_2'\delta_{ij}\right)\right] \tag{24}$$

With simple algebra, the first invariant of the above tensor, $\frac{\partial M_c}{\partial \sigma_{ij}}$, can be shown to vanish, i.e.

$$\frac{\partial M_c}{\partial \sigma_{ii}} = 0 \tag{25}$$

The derivative of the potential function, G_d with respect to σ_{ij}, i.e., $\frac{\partial G_d}{\partial \sigma_{ij}}$, is a second order tensor and can be expressed as a sum of the deviatoric tensor component and an isotropic tensor component, as

$$\frac{\partial G_d}{\partial \sigma_{ij}} = D_{ij} + d\,\delta_{ij} \tag{26}$$

where D_{ij} and d are the deviatoric tensor and the first invariant of the tensor $\frac{\partial G_d}{\partial \sigma_{ij}}$, respectively and their values are given by

$$D_{ij} = \left[\frac{s_\eta \, \eta}{2J_2'}s_{ij} + \ln\left(\frac{J_1}{(J_1)_d}\right)\frac{\partial M_c}{\partial \sigma_{ij}}\right] \tag{27}$$

$$d = \frac{M_c - s_\eta \, \eta}{J_1} \tag{28}$$

Volumetric Yielding

The volumetric yield function, F_v is assumed to be given by

$$F_v = J_1 - (J_1)_v = 0 \tag{29}$$

where $(J_1)_v$ is a constant determining the nature of the hardening.

In view of equation (12) and the volumetric yield function given by equation (29), the volumetric loading is assumed to occur when dJ_1 is positive, while unloading is assumed to occur when dJ_1 is negative. Therefore, the value C_v as in equation (11) is given by

$$\left.\begin{array}{ll} C_v = 1.0 & dJ_1 > 0 \\ C_v = 0.0 & dJ_1 < 0 \end{array}\right\} \tag{30}$$

The plastic strains are assumed to occur only due to virgin loading and reloading and the volumetric unloading induces purely elastic strains, however, the yield surface expressed by equation (29) is assumed to remain valid even during unloading. In other words, the yield surface is assumed to collapse or degrade during unloading.

The potential function of this mechanism, G_v, is assumed to be of the form

$$G_v = J_1 + \frac{27 J_2'}{J_1 M_p^2} - (J_1)_c = 0 \tag{31}$$

where $(J_1)_c$ is a constant and M_p is the ultimate value of stress ratio, η. For the special case of triaxial conditions the above potential function is identical to the one used in the modified cam-clay model (Roscoe & Burland 1968). The family of potential functions during a cyclic triaxial compression test is illustrated in Figure 3b.

The parameter M_p is assumed to change with the plastic distortional strain history in an incremental form such that the ultimate value of M_p is in fact equal to the value of M_c. This use of a different parameter for the ultimate value of stress ratio evolving with the loading history allows us to model the strain-softening behavior of the soil. The incremental variation is assumed to be given by

$$dM_p = \eta(M_c - \eta)(M_p^2 - M_c^2) dW^p \tag{32}$$

where, dW^p is the change in the plastic distortional work given by

$$dW^p = e_{ij}{}^p \, d\sigma_{ij} \tag{33}$$

Since both the parameters M_c and M_p denote the ultimate stress ratio, it is reasonable to assume that the

variation of M_p with respect to σ_{ij} is of the same form as that of that of the parameter M_c. Therefore, in view of equation 34, we get

$$\frac{\partial M_p}{\partial \sigma_{ij}} = \frac{s_\pi\, s_\eta\, c M_p^2 \cos(3\theta)}{3\left[s_\pi\, s_\eta\, c M_p \cos(3\theta) - 3(c-3)\right]} \left[\frac{3}{2J_2'} s_{ij} - \frac{1}{J_3'}\left(s_{ik}s_{kj} - \frac{2}{3}J_2'\delta_{ij}\right)\right] \tag{34}$$

With simple algebraic manipulations, it can be shown that the first invariant of the above tensor, $\frac{\partial M_p}{\partial \sigma_{ij}}$, vanishes, i.e.

$$\frac{\partial M_p}{\partial \sigma_{ij}} = 0 \tag{35}$$

The derivatives of the volumetric potential function, G_v with respect to σ_{ij}, i.e., $\frac{\partial G_v}{\partial \sigma_{ij}}$, is a second order tensor and can be expressed as the sum of isotropic and deviatoric components as

$$\frac{\partial G_v}{\partial \sigma_{ij}} = V_{ij} + v\,\delta_{ij} \tag{36}$$

where, V_{ij} and v are the deviatoric tensor and the first invariant of the tensor $\frac{\partial G_d}{\partial \sigma_{ij}}$ respectively and are given by

$$V_{ij} = \frac{1}{M_p^2}\left[\frac{27}{J_1}\, s_{ij} - \frac{2\eta^2\, J_1}{M_p}\frac{\partial M_p}{\partial \sigma_{ij}}\right] \tag{37}$$

$$v = \frac{M_p^2 - \eta^2}{M_p^2} \tag{38}$$

Hardening parameters

The hardening moduli for volumetric yielding, H_v, and for shear yielding, H_d, were chosen to be functions of the stress and strain state parameters as well as the model parameters as

$$H_v = \frac{M_p}{9(M_p + |\eta|)}\left[\frac{\alpha(I_{1m} - I_1)}{\sigma_a} - \frac{1}{K}\right] \tag{39}$$

$$H_d = \exp\left(\frac{-I_1}{I_{1m} - I_1}\right)\left[\frac{|\eta - \eta_r|\, J_1^2}{27G}\frac{M_p}{(M_p - \eta)}\right]\left(\frac{J_1}{\sigma_a + \sigma_p}\right)^{\beta} \tag{40}$$

where, α is a material parameter that describes the total volume-change behavior due to the change in J_1 (Banerjee & Sribalaskandarajah 1994); η_r is the value of η at the previous shear reversal; I_{1m} is the maximum value of the first strain invariant, I_1; and σ_p is the excess pore pressure. The value of

I_{1m} can be expressed in terms of the initial void ratio, e_0 and the minimum void ratio, e_{min} as

$$I_{1m} = \frac{e_0 - e_{min}}{1 + e_0} \tag{41}$$

In view of the incremental elasto-plastic theory(equation (4)) and the model outlined in the previous section using equations (11), (12), (16), (29), and (31), the incremental elastic strain components can be expressed as

$$d\epsilon_{ij}{}^e = d\epsilon_{ij} - C_v H_v \left(V_{ij} + v\delta_{ij}\right)\, dJ_1 - C_d H_d\, s_\eta \left(D_{ij} + d\delta_{ij}\right)\, d\eta \tag{42}$$

Taking the first invariant of the incremental elastic strain tensor and considering the generalized Hooke's law(equation (6)), one obtains from equation (42)

$$dJ_1 = 3K \left(d\epsilon_{ii} - 3C_v H_v v\, dJ_1 - 3C_d H_d\, s_\eta d\, d\eta\right) \tag{43}$$

Now, considering the definition of the second deviatoric invariant, J_2', of the stress tensor given by equation (2), one gets

$$dJ_2' = s_{ij} ds_{ij} \tag{44}$$

Substituting for ds_{ij} from equation (5), we arrive at

$$dJ_2' = 2G\, s_{ij}\, de_{ij}{}^e \tag{45}$$

In view of equation (42), equation (45) can be rearranged as

$$dJ_2' = 2G\, \left[s_{ij}\, de_{ij} - C_v H_v s_{ij} V_{ij}\, dJ_1 - C_d H_d\, s_\eta s_{ij} D_{ij}\, d\eta\right] \tag{46}$$

In view of equations (25) and (35), the following simplifications can be derived.

$$s_\eta s_{ij} D_{ij} = \eta \tag{47}$$

$$s_{ij} V_{ij} = \frac{2\eta^2\, J_1}{M_p^2} \tag{48}$$

Substituting these expressions, equation (46) can further be simplified as

$$dJ_2' = 2G\left[s_{ij}\,de_{ij} - \frac{2C_v H_v \eta^2 J_1}{M_p^2}\,dJ_1 - C_d H_d \eta\,d\eta\right] \tag{49}$$

In view of equation (14), substituting for the term dJ_2' in terms of $d\eta$ and dJ_1, the above equation can be rewritten as

$$\left[C_d H_d G\,\eta + \frac{J_2'}{\eta}\right]\,d\eta + \left[\frac{J_2'}{J_1} + \frac{2C_v H_v G \eta^2 J_1}{M_p^2}\right]\,dJ_1 = G s_{ij} de_{ij} \tag{50}$$

Rewriting equation (43), we get

$$[9C_d H_d\,s_\eta K d]\;d\eta + [1 + 9C_v H_v K\,v]\;dJ_1 = 3K\,d\epsilon_{ii} \tag{51}$$

Equations (50) and (51) form a set of simultaneous equations in terms of the two unknowns $d\eta$ and dJ_1. These unknowns can be explicitely solved for as

$$dJ_1 = \frac{v_s\,r_s - s_s\,r_v}{v_s\,s_v - s_s\,v_v} \tag{52}$$

$$d\eta = \frac{s_v\,r_v - v_v\,r_s}{v_s\,s_v - s_s\,v_v} \tag{53}$$

where

$$\begin{aligned} s_v &= \frac{J_2'}{J_1} + \frac{2C_v H_v G \eta^2 J_1}{M_p^2} \\ s_s &= C_d\,H_d\,s_\eta\,G\eta + \frac{J_2'}{\eta} \\ v_v &= 1 + 9C_v\,H_v\,Kv \\ v_s &= 9C_d\,H_d\,s_\eta\,K\,d \\ r_s &= G\,s_{ij}\,de_{ij} \\ r_v &= 3K\,d\epsilon_{ii} \end{aligned} \tag{54}$$

The incremental effective stress tensor can be written in terms of dJ_1 and $d\eta$ as

$$\begin{aligned} d\sigma_{ij} &= \frac{dJ_1}{3}\left(1-\frac{2G}{3K}\right)\delta_{ij} + \\ & 2G\left\{d\epsilon_{ij} - C_v H_v\left(V_{ij}+v\delta_{ij}\right)\, dJ_1 + C_d H_d\, s_\eta\, \left(D_{ij}+d\delta_{ij}\right)\, d\eta\right\} \end{aligned} \tag{55}$$

Computation of incremental strain from incremental stress

The choice of components of incremental stress as primary variables does not require any assumptions regarding the drainage conditions. However, the drainage conditions have an impact on how the incremental strains are computed. This is because during undrained drainage conditions excess pore pressure is induced, and the effective stress tensor is therefore different from the total stress tensor. Due to the effective stress principle, the incremental effective stress tensor, $d\sigma_{ij}$, can be expressed in terms of the incremental total stress tensor, $d{\sigma_{ij}}^t$, and the incremental pore pressure, $d\sigma_p$, as

$$d\sigma_{ij} = d{\sigma_{ij}}^t - d\sigma_p\delta_{ij} \tag{56}$$

Drained

Since excess pore pressure is not generated during fully drained conditions, the incremental effective stress tensor is identical to the incremental total stress tensor. Thus, one can readily calculate the values of dJ_1 and $d\eta$ from the the incremental stress and the incremental elastic and plastic strain tensors can be evaluated explicitly. The incremental strain tensor can be expressed as

$$d\epsilon_{ij} = \frac{ds_{ij}}{2G} + \frac{d\sigma_{ii}}{9K}\,\delta_{ij} + C_v H_v\left(V_{ij}+v\delta_{ij}\right)\, dJ_1 + C_d H_d\, s_\eta\, \left(D_{ij}+d\delta_{ij}\right)\, d\eta \tag{57}$$

Undrained

In practice, components of effective stress are difficult to control, therefore the components of incremental total stresses are considered as the primary variables. Although the components of incremental total stress are known, due to the development of pore pressure, the components of incremental effective stress remain unknown. However, the first invariant of the incremental strain tensor is zero due

to the drainage conditions. Therefore, in view of the equations (50)-(55) one can arrive at

$$d\eta = \frac{-v_v}{v_s}\, dJ_1 \tag{58}$$

Substituting for $d\eta$ from equation (14) and eliminating dJ_2' in view of equation (44), the above equation simplifies to

$$dJ_1 = \frac{\eta\, J_1\, v_s}{2J_2'\,(v_s\eta - v_v J_1)}\, s_{ij}\, ds_{ij} \tag{59}$$

where

$$ds_{ij} = d\sigma_{ij}^t - \frac{d\sigma_{ii}^t}{3}\,\delta_{ij} \tag{60}$$

Substituting equation (59) into equation (58), the value of $d\eta$ can be expressed as

$$d\eta = \frac{-\eta\, J_1\, v_v}{2J_2'\,(v_s\eta - v_v J_1)}\, s_{ij}\, ds_{ij} \tag{61}$$

Using equations (59)-(61), the values of dJ_1 and $d\eta$ can be calculated. Thus, the values of incremental strain tensor and the incremental effective stress tensor are expressed in terms of dJ_1 and $d\eta$ as

$$\begin{aligned} d\epsilon_{ij} &= \frac{ds_{ij}}{2G} + \frac{dJ_1}{9K}\,\delta_{ij} + \\ &\quad C_v H_v\,(V_{ij} + v\delta_{ij})\; dJ_1 + C_d H_d\, s_\eta\,(D_{ij} + d\delta_{ij})\; d\eta \end{aligned} \tag{62}$$

$$d\sigma_{ij} = ds_{ij} + \frac{dJ_1}{3}\,\delta_{ij} \tag{63}$$

The practical usefulness of the model presented in this paper depends on the actual performance as well as the ease with which the model parameters are identified for a given soil. The model parameters could be identified either by devising simple experiments reflecting the influence of each individual parameters or by using numerical techniques to match experimental data. In this study, the latter approach is employed and the method used is outlined in the next section.

The model proposed herein handles general three dimensional loading conditions. But, most of the reliable experimental studies of the behavior of soils are limited to specific loading conditions such as, triaxial, one-dimensional compression, direct shear, and pure shear. Among these experiments the triaxial tests are the most common, therefore, the model performance in this study is essentially limited

to the performance of the proposed soil model under monotonic and cyclic triaxial loading conditions.

Parameter Estimation Using Optimization

The response of any plasticity model can not be expressed analytically, as the formulation of the models are inceremental and complex. Hence, the model response has to be computed and expressed numerically. On the other hand, the observed model response is almost always numerical. Using the model estimates and the observed values, a numerical scheme using the optimization techniques to estimate the model parameters minimizing the error in the computed response is described. Computed results obtained from this numerical technique and observed results are presented and discussed for monotonic and cyclic loading conditions.

A numerical scheme based on the optimization techniques is outlined in this section to estimate the numerical values of the parameters of the model presented in the previous chapter. The objective of the scheme is to find a set of model parameters reproducing the experimental results with minimum error. The total error can be expressed in terms of the observed and computed values of the experiment. This error function serves as the objective function in a minimization algorithm and a solution is found by minimizing the objective function over the acceptable range of the model parameters. In otherwords, the goal of the numerical scheme presented in this section is to locate the "global minimum" of the objective function and the corresponding model parameters.

The algorithms used in the optimization schemes of this type of non-linear objective functions are iterative in nature. The algorithms start with an initial estimate, proceeding to find a sequence of newer estimates, each representing an improvement over the previous estimates. These algorithms are broadly classified as, direct search methods, gradient and second deriveative methods, and non-linear least square methods. Of these algorithms the direct search methods are the simplest methods of optimization. These algorithms require only the function values to direct the search, while gradient based methods require the knowledge of the gradients as well. Although, direct search methods are less efficient then gradient based methods, they are simple and easier to implement. These algorithms are well suited for applications in which the objective functions are non-smooth or non-diffentiable, or the derivatives are discontinuous. On the other hand, nonlinear least squares methods are well suited for minimization problems with nonlinear least squares objective functions, which are expressed as a

sum of suqares of $n(> n_p)$ nonlinear functions.

$$F(\boldsymbol{P}) = \sum_{i=1}^{n} \left[F_i^2\right] \tag{64}$$

Where, $\boldsymbol{P}$ is the vector of parameters the objective function depends on and n_p is the length of the vector $\boldsymbol{P}$.

The model performance and observed performance in this study are numerical in nature. Therefore, the gradients of the observed and computed functions have to be computed using finite difference assumptions and any one of the above optimization algorithms can be used to minimize the objective function. But, since the objective function in this study is naturally expressed as a sum of squares of nonlinear functions, a minimization using the non-linear least squares algorithm (Dennis, Gay & Welsch 1981*a*, Dennis, Gay & Welsch 1981*b*) is used in this study.

In general the objective function can be expressed as a function of the experimentally observed and the computed variables, mean total stress, shear stress, volumetric strain, shear strain, and excess pore pressure. Noting that the model presented is based on effective stress principle and the value of effective stress can be estimated from the values of mean total strees and excess pore pressure, the variables of interest can be limited to the four variables, mean effective stress, p, shear stress, $q(= \sqrt{3J_2'})$, volumetric strain, $\epsilon_v(= \epsilon_{ii})$, and shear strain, ϵ_q. These variables in general are independent of each other. But, depending on stress path and drainage conditions, the values of some of these variables are known or are interrelated. The observed values of these variables, mean effective stress, shear stress, volumetric strain, and shear strain are denoted with a superscipt "o" as, p_i^o, q_i^o, $\epsilon_{v_i}^o$, and $\epsilon_{q_i}^o$, respectively are recorded during an experiment at discrete intervals. In addition, since the model is incremental in nature, it is not possible to express the model prediction explicitly as a function of the model parameters and the state parameters. Hence, the predicted values of the above variables, denoted with a superscript "c" as, p_i^c, q_i^c, $\epsilon_{v_i}^c$, and $\epsilon_{q_i}^c$, respectively are computed numerically at discrete points at which the experimental values of these variables were recorded.

During drained triaxial loading, no excess pore pressure is being developed and the ratio between incremental mean effective stress and incremental shear stress is a constant determined by the type of triaxial loading, such as axial compression/extension, lateral compression/extension, constant mean stress, constant shear stress, and constant shear stress ratio, that the soil sample is being subjected to.

Considering that the experiment is done on a prescribed stress path, the natural choice of independent variable is either the mean effective principal stress or the shear stress. Hence, the variables volumetric strain and shear strain, can be expressed as functions of model parameters and mean effective principal stress.

On the other hand, during undrained triaxial loading no volumetric strain is developed. But due to the development of excess pore pressure, the ratio between incremental mean effective stress and incremental shear stress is not a constant. Therefore, the choice of shear strain as the primary variable seems to be most logical choice in this case. The variables, mean effective stress and shear stress can be expressed as functions of model parameters and shear strain. The following subsections describe the optimization schemes under these two different choices of primary variables.

Drained triaxial loading

Let's consider a drained axial compression test in which the results are expressed in terms of the mean effective stress, as shown in the figure 4. Since the primary variable is mean effective stress and the stress path is axial compression, the observed parameters, p_i^o and q_i^o, are identical with the computed parametrs, p_i^c and q_i^c, producing no errors. The objective function, F, which is a function of model variables, $G_o, K_o, \alpha, \beta, \zeta, M_c$, and M_p, and the state variables, e_0 and e_{min}, therefore can be expressed in terms of the variables, $\epsilon_{v_i}^o$, $\epsilon_{q_i}^o$, $\epsilon_{v_i}^c$, and $\epsilon_{q_i}^c$, i.e.,

$$F(\boldsymbol{P}) = \sum_{i=1}^{n} \left[(\epsilon_{v_i}^o - \epsilon_{v_i}^c)^2 + (\epsilon_{q_i}^o - \epsilon_{q_i}^c)^2 \right] \tag{65}$$

where, n is the total number of observed points, and the vector $\boldsymbol{P}$ is a collection of the model parameters and the state parameters as

$$\boldsymbol{P} = < G_o, K_o, \alpha, \beta, \zeta, M_c, M_p, e_o, e_{min} >^T \tag{66}$$

The values of $\boldsymbol{P}$ can be estimated by minimizing the above objective function, using standard optimization techniques.

Using the above error function given in the equation 65, the optimization techniques will yield a reasonable set of parameters, if the magnitudes of volumetric strain and shear strain data are of the

same order. On the other hand, if the volumetric strain and shear strain data follow distinctly different patterns and magnitudes, then the model parameters obtained will reflect an unreasonable weighting towards the variable with the larger magnitude and towards the range at which the large magnitudes occur. This problem could be overcome by estimating the error function with normalized values of the observed data as

$$F(\boldsymbol{P}) = \sum_{i=1}^{n} \left[\left(\frac{\epsilon_{v_i}^o - \epsilon_{v_i}^c}{(\epsilon_{v_i}^o)_{max}} \right)^2 + \left(\frac{\epsilon_{q_i}^o - \epsilon_{q_i}^c}{(\epsilon_{q_i}^o)_{max}} \right)^2 \right] \tag{67}$$

where, $(\epsilon_{v_i}^o)_{max}$ is the maximum absolute value of the observed volumetric strain, and $(\epsilon_{q_i}^o)_{max}$ is the maximum absolute value of the observed volumetric strain.

Undrained triaxial loading

In an undrained triaxial compression test, the choice of shear strain as primary variable is quite convenient as has been discussed earlier. The figure 5 shows observed and computed results of an undrained triaxial compression test. As has been discussed earlier, the values of $\epsilon_{v_i}^o$ and $\epsilon_{v_i}^c$ are zero and $\epsilon_{q_i}^o$ is equal to $\epsilon_{q_i}^c$. Therefore, the objective function can be viewed as an error function in terms of the variables, p_i^c, q_i^c, p_i^o, and q_i^o, as

$$F(\boldsymbol{P}) = \sum_{i=1}^{n} \left[(p_i^o - p_i^c)^2 + (q_i^o - q_i^c)^2 \right] \tag{68}$$

Performance of the Model

Monotonic Behavior

The performance of the proposed model under monotonic loading conditions is discussed in this subsection, by comparing the observed experimental performance from published sources (Tatsuoka & Ishihara 1973, Tatsuoka & Ishihara 1974*b*) with the predicted performance. The model performance is predicted with the model parameters obtained with the numerical optimization outlined above, minimizing the error between the observed and predicted data.

Figure 6 presents the experimental results (Tatsuoka & Ishihara 1973) and the predicted results of drained triaxial compression tests on soil samples with three different initial confining pressures. The observed and predicted volumetric strain (figure 6a) and shear strain (figure 6b) compare very rea-

sonably. Similar comparision of observed and experimental data for undrained triaxial compression test is presented in figure 7. Close agreement of the observed and predicted stress paths in conjunction with the strain levels is noted. It should also be noted that the values of the model parameters are within a resonable limit, as bounded optimization is used to limit the solution to within a reasonable range. Therefore, the reasonable matches of observed and predicted data noted above, favorably evaluates the performance of the model for drained and undrained monotonic triaxial compression tests. Figures 8 and 9 show the experimental results (Tatsuoka & Ishihara 1974*b*) and predicted results for drained stress paths given by the figures 8a and 9a. The observed and computed volumetric strains for the above stress paths are depicted in the figures 8b and 9b, respectively. The corresponding shear strains are depicted in the figures 8c and 9c. The above stress paths comprise a combination of axial compression, axial extension and constant shear triaxial loading paths. The model parameters used in the computed results are obtained by the optimization procedure outlined above. These figures show excellent agreement between observed and computed data. This demonstrates the proposed model's validity under a complex loading path with stress reversal.

Cyclic Behavior

The performance of the proposed model under cyclic loading is examined by simulating the qualitative behavior observed in the experimental data from published sources (Tatsuoka & Ishihara 1974*a*, Ishihara, Tatsuoka & Yasuda 1975). The simulations included cyclic triaxial tests under stress controlled and strain controlled test conditions with drained and undrained drainage conditions. Although the experimental results and the calculated model results are shown side by side for easy comparision, no attempt was made to identify the values of the model parameters corresponding to the soil in question.

Figure 10a and figure 11a show the experimental results (Tatsuoka & Ishihara 1974*a*) of a stress controlled drained test on a loose sand sample subjected to triaxial compression and extension between constant amplitudes of stress ratios, while the figures 10b and 11b show the behavior produced by the proposed model. The volumetric strain change is depicted in the figure 10 and it is observed that the volumetric deformation during the initial cycles is predominantly plastic, and in the subsequent cycles it is essentially elastic. Similar observation could be made with respect to the shear strains(figure 11) as the hysteresis exhibited becomes smaller with each cycle. The figure 12 shows a sample of the same sand subjected to the same test between larger amplitudes of stress ratios producing larger volumetric

deformation. More importantly, much of the volumetric deformation in this case is plastic.

Figure 13a and figure 14a show the experimental results (Tatsuoka & Ishihara 1974*a*) of a strain controlled drained test on a loose sand sample subjected to triaxial compression and extension between constant amplitudes of shear strains. With each additional cycle the sample sustains higher value of stress ratios and therefore higher value of shear stresses. This explains why the response is a combination of responses that were discussed in the previous paragraphs. The figure 13b and 14b show the behavior produced by the proposed model.

Figures 15a and 16a show the experimental results (Ishihara et al. 1975) of a stress controlled undrained test on a loose sand sample subjected to triaxial compression and extension between constant amplitudes of shear stresses. Due to porepressure buildup, the range of stress ratio increases with each aditional cycle. The initial buildup of the excess pore pressure is small and the rate of porepressure increase is slowly increasing with each additional cycle. However, when the stress ratio approaches the value of the critical state parameter the rate of increase becomes siginificantly large. In the subsequent cycles either liquefaction or cyclic mobilty is observed. This behavior is reproduced by the model in figure 15b. As to the shear strain, the magnitude of the shear strain increases with each cycle, however, the increase is significantly large after the liquefaction is initiated. The area of the hysteretic loop exhibited also becomes significantly larger. This behavior is reproduced in the figure 16b by the proposed model.

Figure 17a and figure 18a show the experimental results (Ishihara et al. 1975) of a strain controlled undrained test on a loose sand sample subjected to triaxial compression and extension between constant amplitudes of shear strains. Unlike in drained conditions the shear stress is decreasing with each cycle and therfore the cyclic shear modulus(secant) decreases. This is depicted in the figure 18c and the 5igures 17b and 18b show that the model behavior is in agreement with the experimental behavior.

Summary

An incremental plasticity approach based on double hardening concepts is presented in this paper to model the behavior of geomaterials. The present work extends the simpler model by the authors for monotonic triaxial loading conditions. The proposed model is extended to include general, three di-

mensional loading conditions. It is not irrelevant to note that a three dimensional finite element program, which has been created by the first author, uses this model efficiently even for earthquake problems.

In summary, the present model can be categorized as a non-associative plasticity model based on multiple yielding concepts of Koiter (1953). Two separate yielding mechanisms are used in this model, each characterizing the volumetric and shear yielding behavior of the geomaterial. The complete set of the equations expounding the model is included in this paper so that they can be incorporated in numerical techniques. A numerical scheme utilizing advanced optimization techniques to identify the model parameters is also briefly described here. Finally this paper includes the comparisions of model predictions and experimental results. It is shown that the experimental results are adequately represented by the present model.

Acknowledgements

This investigation was funded in part by grants from the N.S.F(Grant Nos., MSM-8657628, MSM-9203140, and MSS-9112243) and from the Air Force Office of Scientific Research(Grant No. AFOSR-91-0424). The authors are indebted to Dr. Roberto O. Davis, whose association made the original model possible. Finally, the active participation of Prof. Gregory R. Miller is greatly appreciated.

References

Banerjee, S., Davis, R. O. & Sribalaskandarajah, K. (1992), 'Simple double-hardening model for geomaterials', *Journal of Geotechnical Engineering* **118**(6), 889–901.

Banerjee, S. & Sribalaskandarajah, K. (1994), An alternative formulation for volume-change bahavior of soils, *in* A. T. Yeung & G. Y. Félio, eds, 'Vertical and Horizontal Deformations of Foundations and Embankments; Proceedings of Settlement '94, Texas', Vol. 1, ASCE, pp. 652–662. Geotechnical Special Publication No. 40.

Dafalias, Y. F. & Popov, E. P. (1975), 'A model of nonlinearly hardening materials for complex loading', *Acta Mech.* **21**(3), 173–192.

Dennis, J. E., Gay, D. M. & Welsch, R. E. (1981*a*), 'An adaptive nonlinear least-squares algorithm', *ACM Transactions on Mathematical Software* **7**(3), 348–368.

Dennis, J. E., Gay, D. M. & Welsch, R. E. (1981*b*), 'Algorithm 573 NL2SOL - an adaptive nonlinear least-squares algorithm [E4]', *ACM Transactions on Mathematical Software* **7**(3), 369–383.

Hardin, B. O. & Drnevich, V. P. (1972), Shear modulus and damping in soils: Design equations and curves, *in* 'Proceedings of ASCE', Vol. 98(SM6), pp. 603–624.

Hashiguchi, K. (1986), Elastoplastic constitutive model with a subloading surface, *in* 'Proceedings of the International Conference on Computational Mechanics', Springer–Verlag.

Ishihara, K., Tatsuoka, F. & Yasuda, S. (1975), 'Undrained deformation and liquefaction of sand under cyclic stresses', *Soils and Foundations* **15**(1), 29–44.

Koiter, W. T. (1953), 'Stress-strain relations, uniqueness, and variational theorems for elasto-plastic materials with a singular yield surface', *Quart. Appl. Math.* **11**(3), 350–.

Matsuoka, H. & Nakai, T. (1974), 'Stress-deformation and strength charateristics of soil under three different principal stresses', *Transactions of JSCE* **6**, 108–109.

Mroz, Z. & Pietruszczak, S. (1983), 'A constitutive model for sand with anisotropic hardening rule', *International Journal for Numerical and Analytical Methods in Geomechanics* **7**(3), 305–320.

Pietruszczak, S. & Mroz, Z. (1983), 'On hardening of anisotropy of Ko-consolidated clays', *International Journal for Numerical and Analytical Methods in Geomechanics* **7**(1), 19–38.

Prevost, J. H. & Hoeg, K. (1975), 'Effective stress-strain-strength model for soils', *Journal of Geotechnical Engineering* **101**(3), 257–288.

Roscoe, K. H. & Burland, J. B. (1968), On the generalized stress-strain behavior of "wet" clay, *in* 'Engineering Plasticity', Cambridge University Press, Cambridge, U.K., pp. 535–609.

Roscoe, K. H., Schofield, A. N. & Wroth, C. P. (1958), 'On the yielding of soils', *Geotechnique* **8**(1), 22–53.

Tatsuoka, F. & Ishihara, K. (1973), Stress path and dilatancy performance of a sand, *in* 'Proceeding of 8th International Conference in Soil Mechanics and Foundation Engineering', Vol. 1, pp. 419–424.

Tatsuoka, F. & Ishihara, K. (1974*a*), 'Drained deformation of sand under cyclic stresses reversing direction', *Soils and Foundations* **14**(3), 51–65.

Tatsuoka, F. & Ishihara, K. (1974*b*), 'Yielding of sand in triaxial compression', *Soils and Foundations* **14**(2), 63–76.

Notations

α Material constant describing the volume change behavior during isotropic compression

β Material constant describing the power relation of elastic bulk modulus

ϵ Strain tensor

$\epsilon_{vi}{}^{c}$ Computed volumetric strain

$\epsilon_{qi}{}^{c}$ Computed shear strain

$\epsilon_{vi}{}^{o}$ Observed volumetric strain

$\epsilon_{qi}{}^{o}$ Observed shear strain

η Stress ratio

η_d A constant describing the nature of hardening in shear yield mechanism

η_f Stress ratio at failure

η_r Value of stress ratio at the previous stress reversal

σ Effective stress tensor

σ_m Mean effective stress

σ_a Reference mean efective stress

σ_p Excess pore pressure

θ Lode angle

ζ Material constant describing the power relation of elastic shear modulus

C_d Switch (1/0) for shear yielding mechanism

C_v Switch (1/0) for volumetric yielding mechanism

c material constant in Matsuoka and Nakai's failure criterion

D_{ij} Deviatoric part of the derivatives of the potential function for shear mechanism with respect to stress tensor.

d First invariant of the derivatives of the potential function for shear mechanism with respect to stress tensor.

e Void ratio

e_o Initial void ratio

e_{min} Minimum void ratio

$F_k, k = 1, n$ Yield functions

F_d Yield function for shear yielding mechanism

F_v Yield function for volumetric yielding mechanism

G Elastic shear modulus

G_o Reference value of elastic shear modulus

$G_k, k = 1, n$ Potential functions

G_d Potential function for shear yielding mechanism

G_v Potential function for volumetric yielding mechanism

H_d Hardening parameter for shear yielding mechanism

H_v Hardening parameter for volumetric yielding mechanism

I_1 First invariant of the effective strain tensor

I_{1m} Maximum value of the first invariant of the effective strain tensor

J_1 First invariant of the effective stress tensor

J_2 Second invariant of the effective stress tensor

J_3 Third invariant of the effective stress tensor

J_1' First invariant of the effective stress tensor

J_2' Second invariant of the effective stress tensor

J_3' Third invariant of the effective stress tensor

$(J_1)_v$ A constant describing the nature of hardening in volumetric yield mechanism

K Elastic bulk modulus

K_o Reference value of elastic bulk modulus

M_c Absolute value of the ultimate stress ratio at failure

M_p Absolute value of the ultimate stress ratio

p_i^c Computed mean effective stress

q_i^c Computed shear stress

p_i^o Observed mean effective stress

q_i^o Observed shear stress

s Deviatoric effective stress tensor

s_η Sign of the change in stress ratio, η

s_π Sign of the third deviatoric stress invariant, J_3'

V_{ij} Deviatoric part of the derivatives of the potential function for volumetric mechanism with respect to stress tensor

v First invariant of the derivatives of the potential function for volumetric mechanism with respect to stress tensor.

dW^p Change in the plastic distortional work

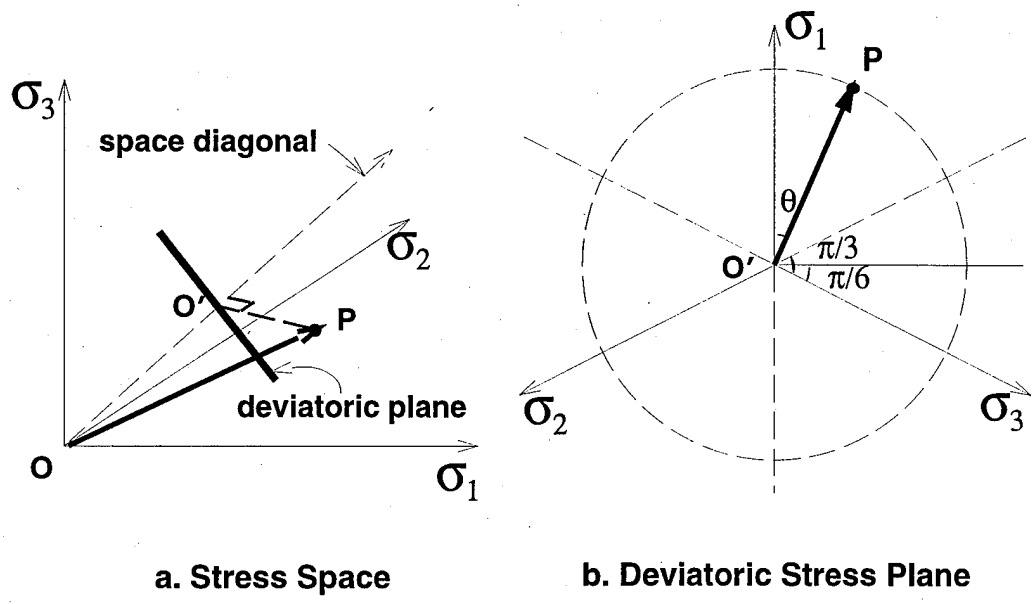

FIGURE 1: Stress Space and its Geometric Interpretation

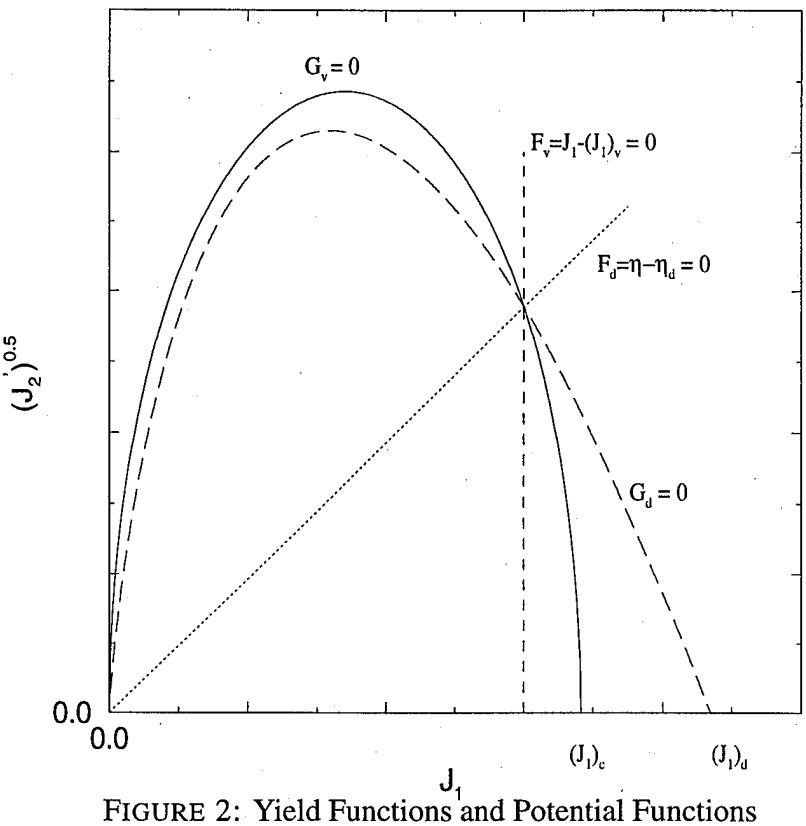

FIGURE 2: Yield Functions and Potential Functions

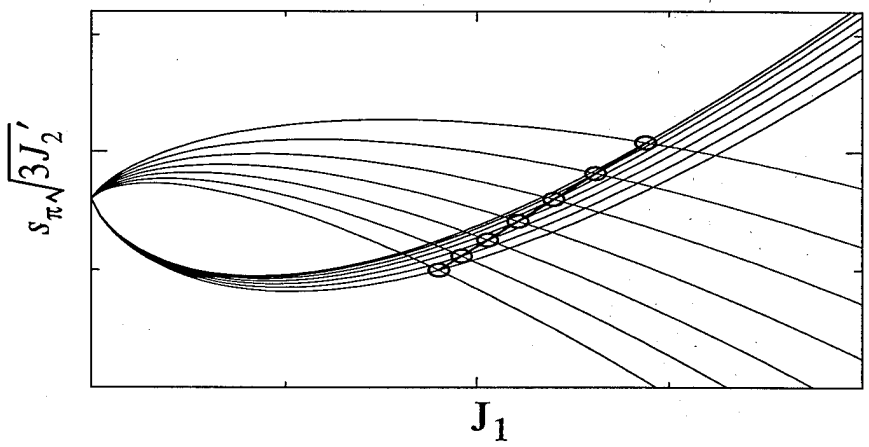

a). Shear Mechanism

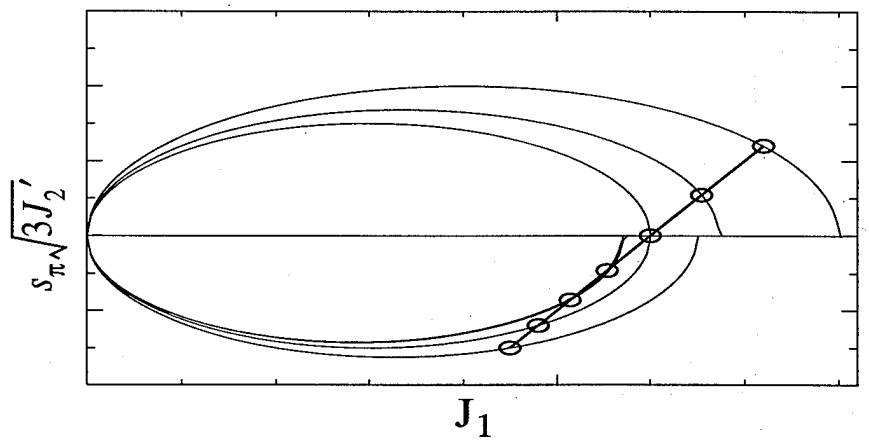

b). Volumetric Mechanism

FIGURE 3: Evolution of Potential functions during cyclic triaxial compression test

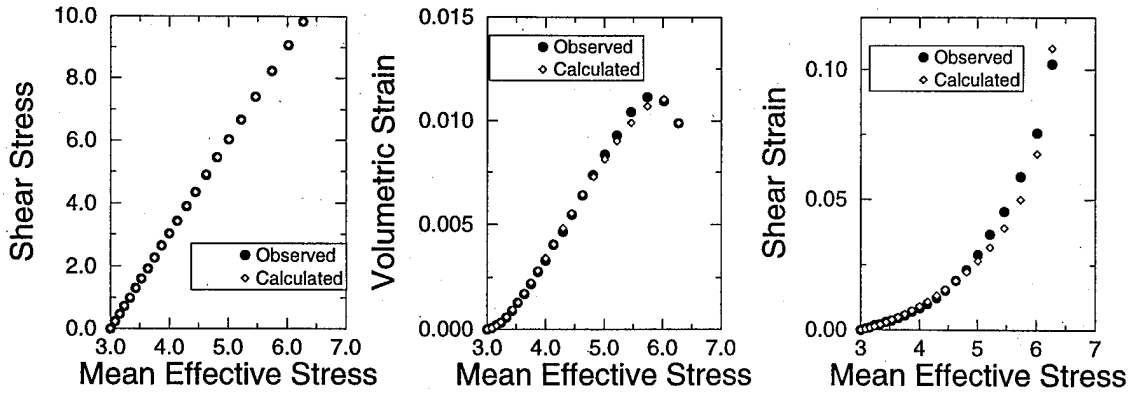

FIGURE 4: Results of a drained monotonic axial compression test

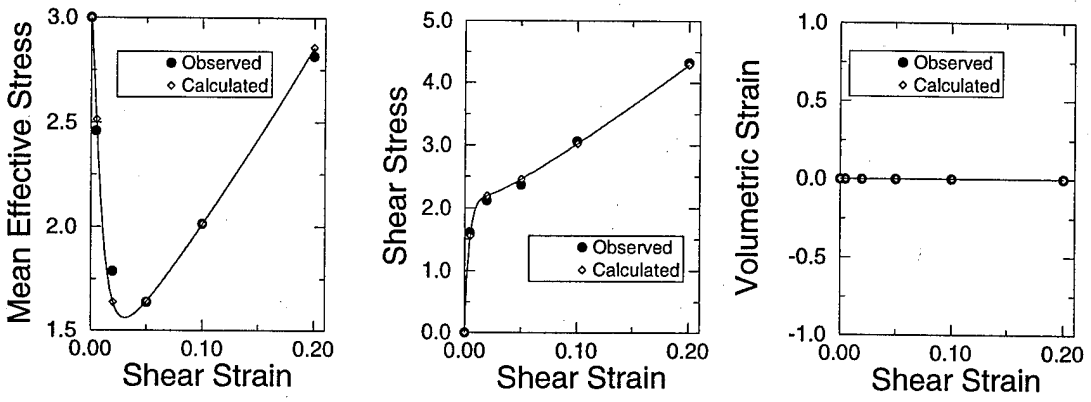

FIGURE 5: Results of a undrained monotonic axial compression test

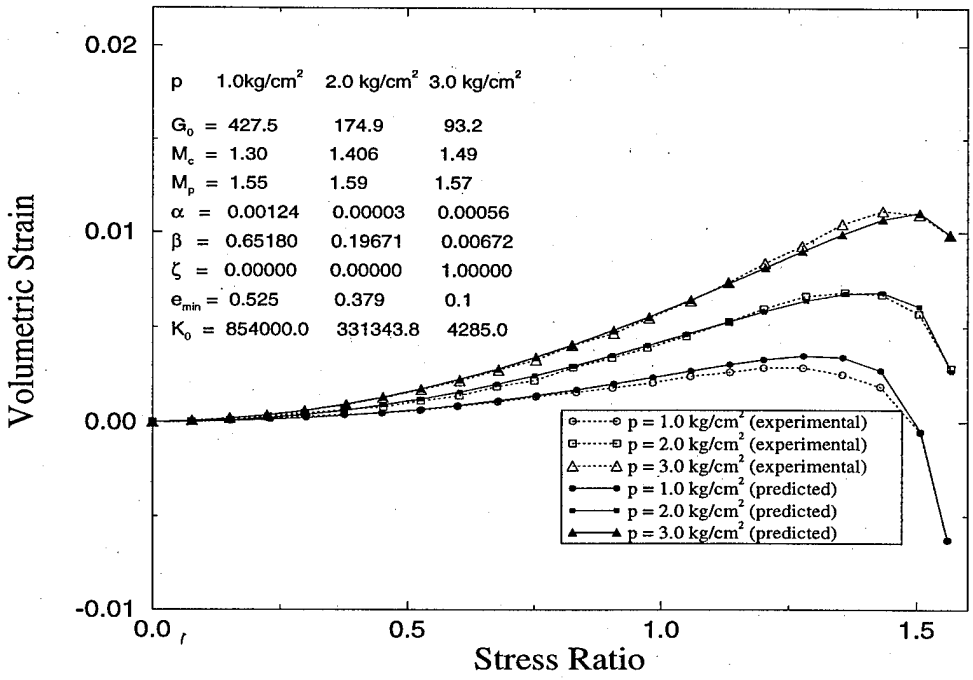

(A) Volumetric Strain

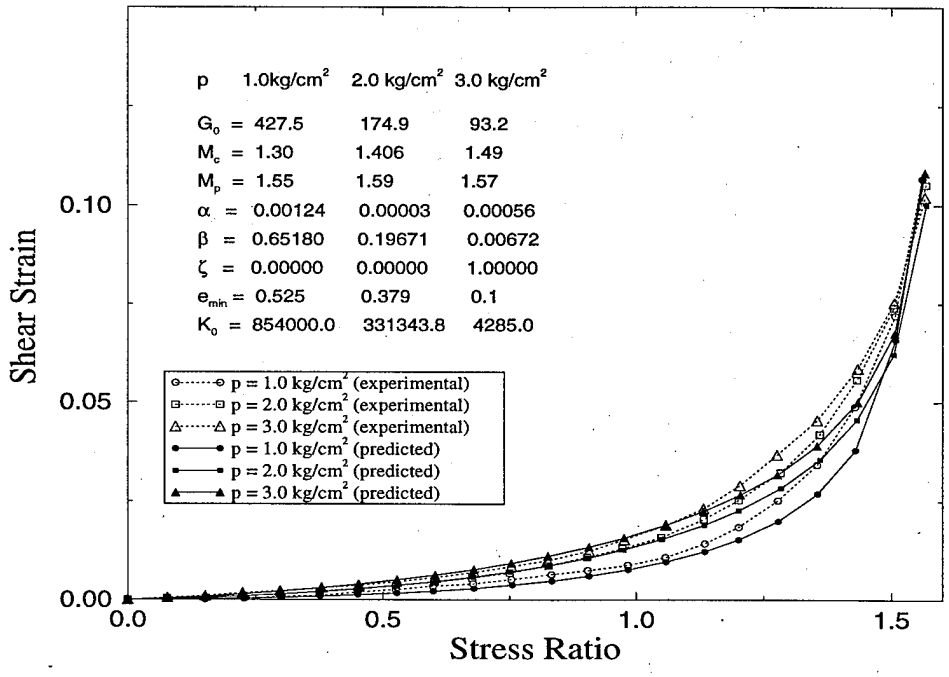

(B) Shear Strain

FIGURE 6: Comparision between Computed and Experimental results of drained axial compression tests(after Tatsuoka and Ishihara, 1973)

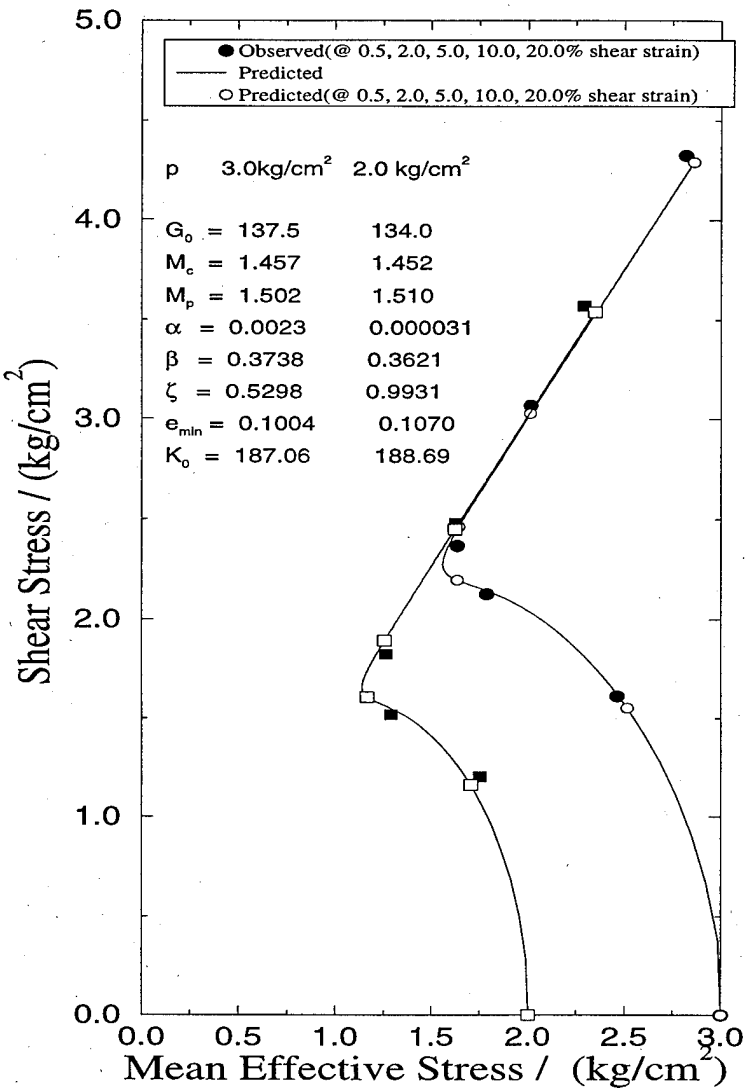

FIGURE 7: Comparision between Computed and Experimental results of undrained axial compression tests(after Tatsuoka and Ishihara, 1973)

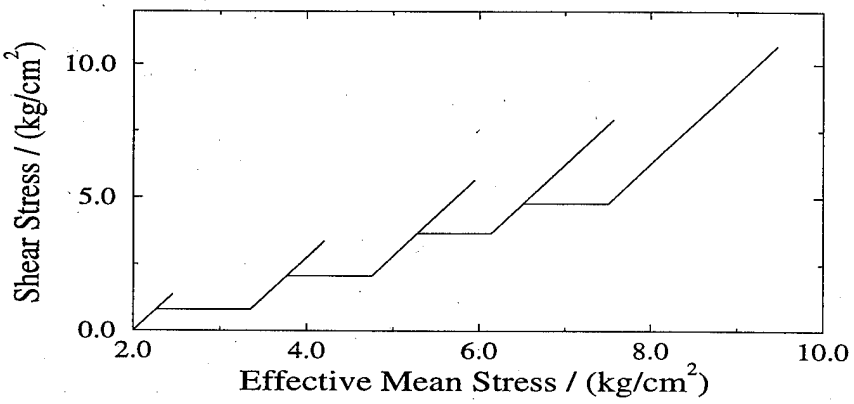

(A) Stress Path

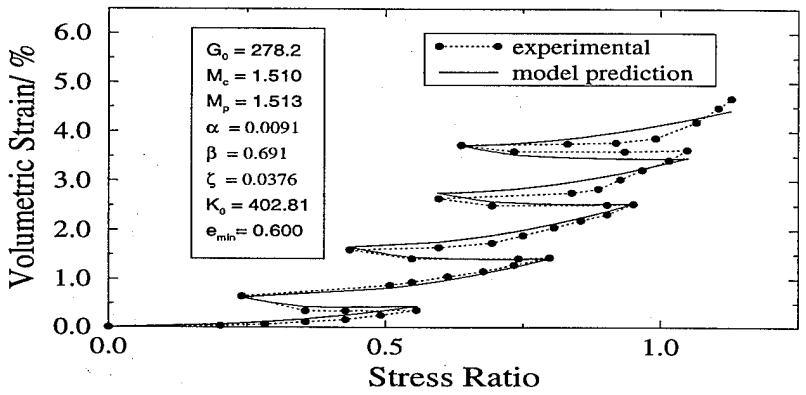

(B) Volumetric Strain

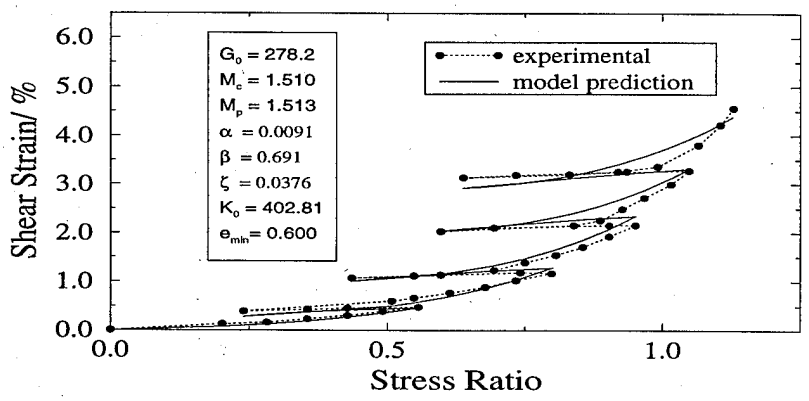

(C) Shear Strain

FIGURE 8: Comparision between Computed and Experimental results (after Tatsuoka and Ishihara, 1974) for Fuji Sand

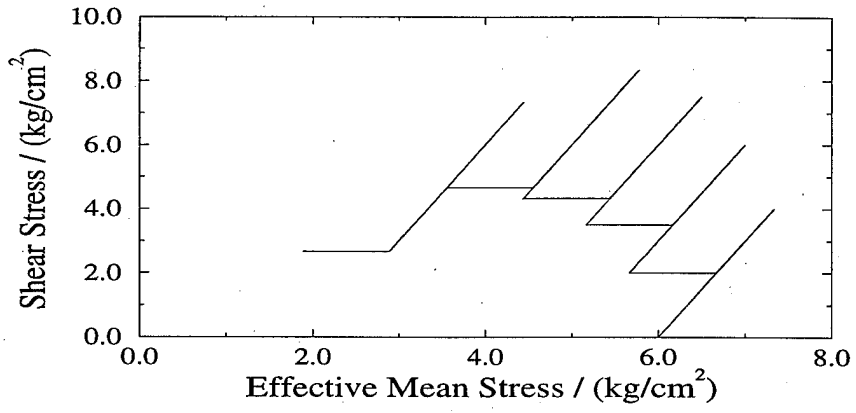

(A) Stress Path

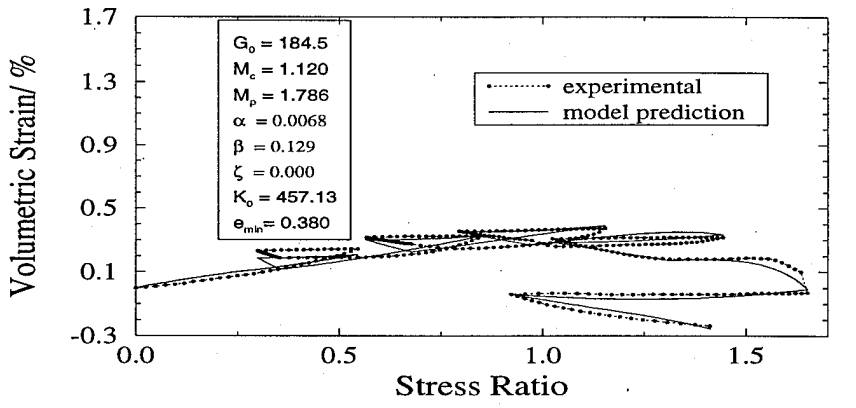

(B) Volumetric Strain

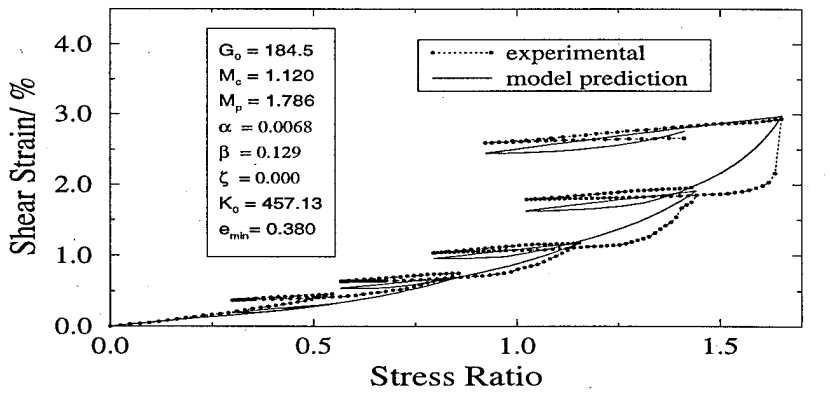

(C) Shear Strain

FIGURE 9: Comparision between Computed and Experimental results (after Tatsuoka and Ishihara, 1974) for Fuji Sand

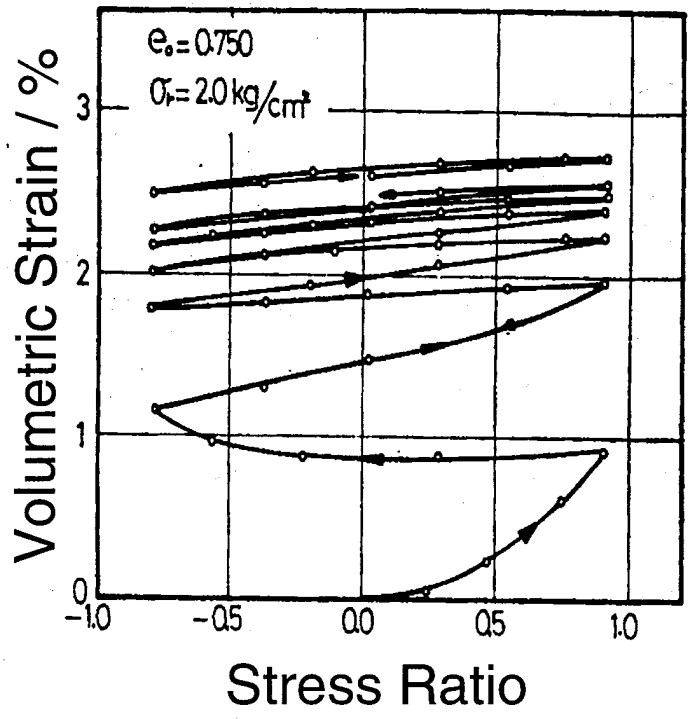

a). Experimental (after Tatsuoka and Ishihara, 1974)

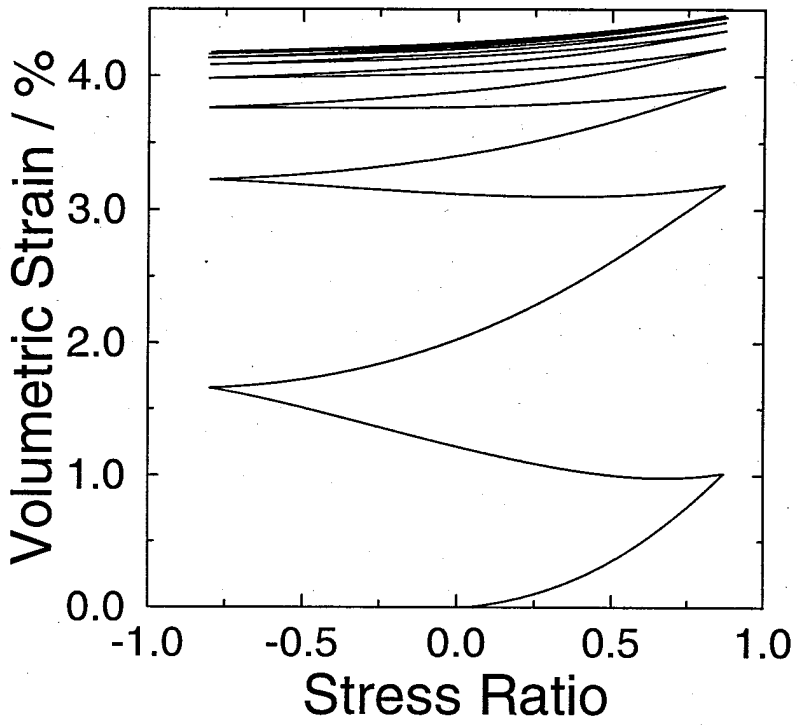

b). Model behavior

FIGURE 10: Volumetric strain against Stress ratio under stress controlled drained cyclic triaxial test with medium amplitude of stress ratio

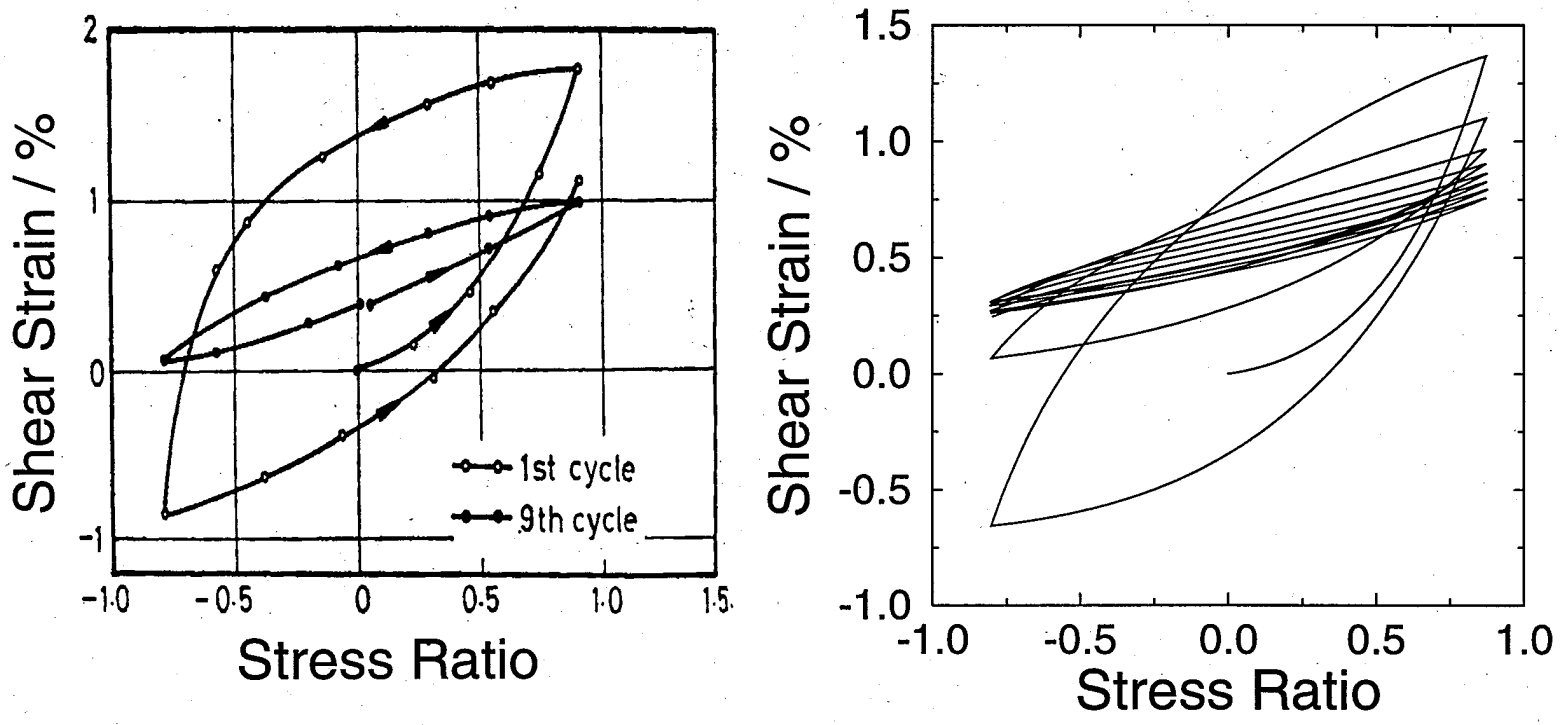

a). Experimental (after Tatsuoka and Ishihara, 1974)

b). Model behavior

FIGURE 11: Shear strain against Stress ratio under stress controlled drained cyclic triaxial test with medium amplitude of stress ratio

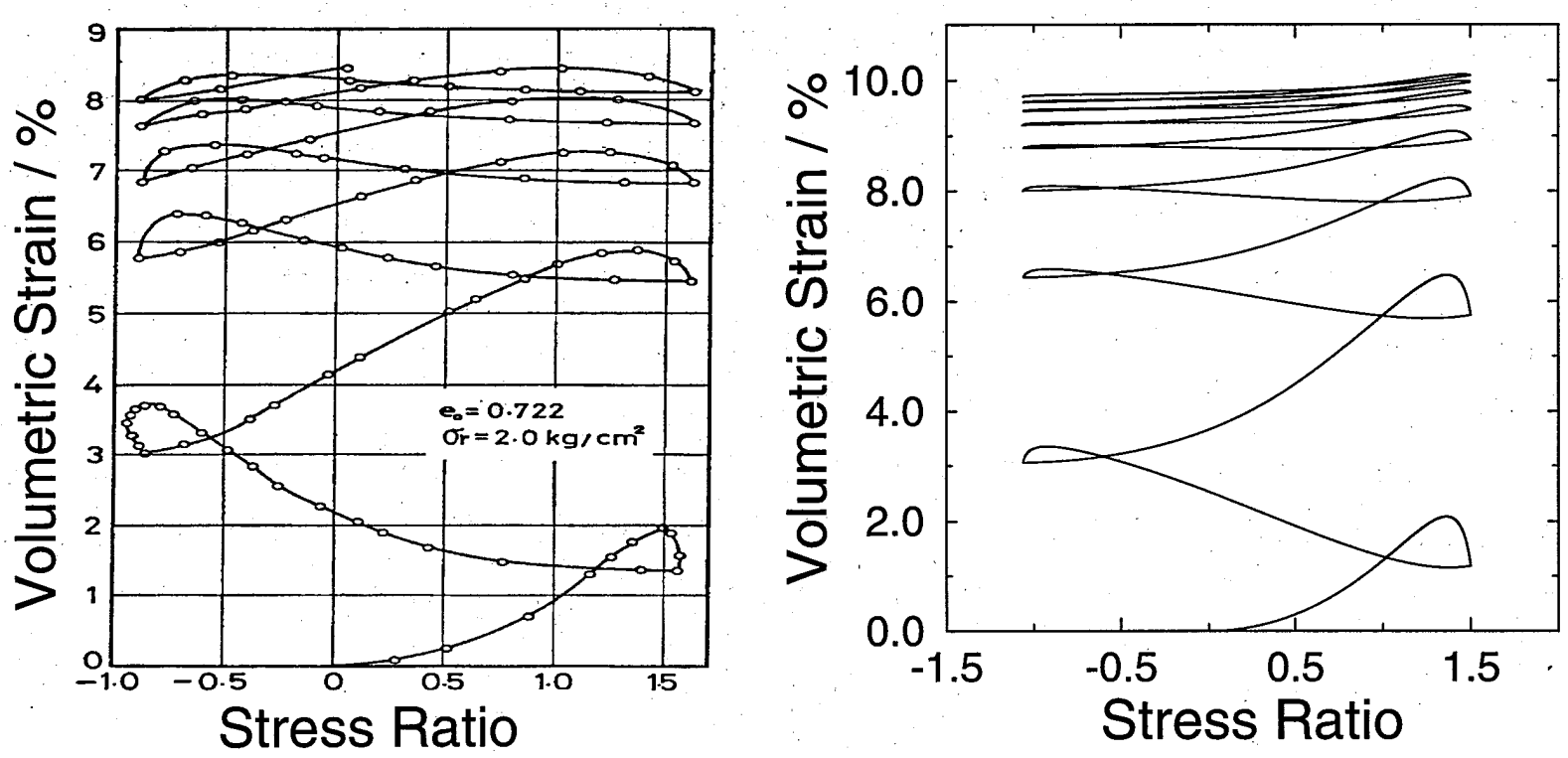

a). Experimental (after Tatsuoka and Ishihara, 1974)

b). Model behavior

FIGURE 12: Volumetric strain against Stress ratio under stress controlled drained cyclic triaxial test with large amplitude of stress ratio

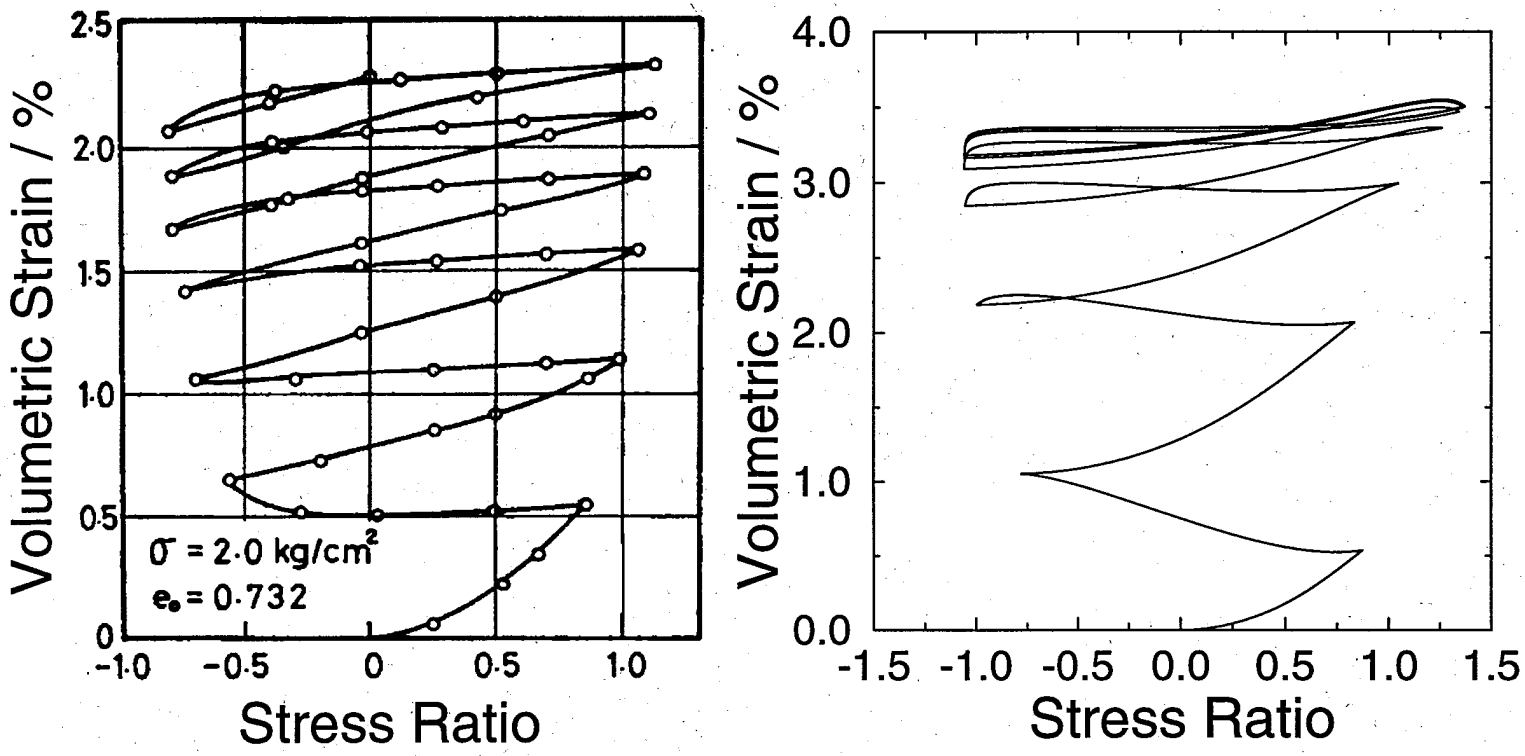

a). Experimental (after Tatsuoka and Ishihara, 1974)

b). Model behavior

FIGURE 13: Volumetric strain against Stress ratio under constant amplitude strain controlled drained cyclic triaxial test

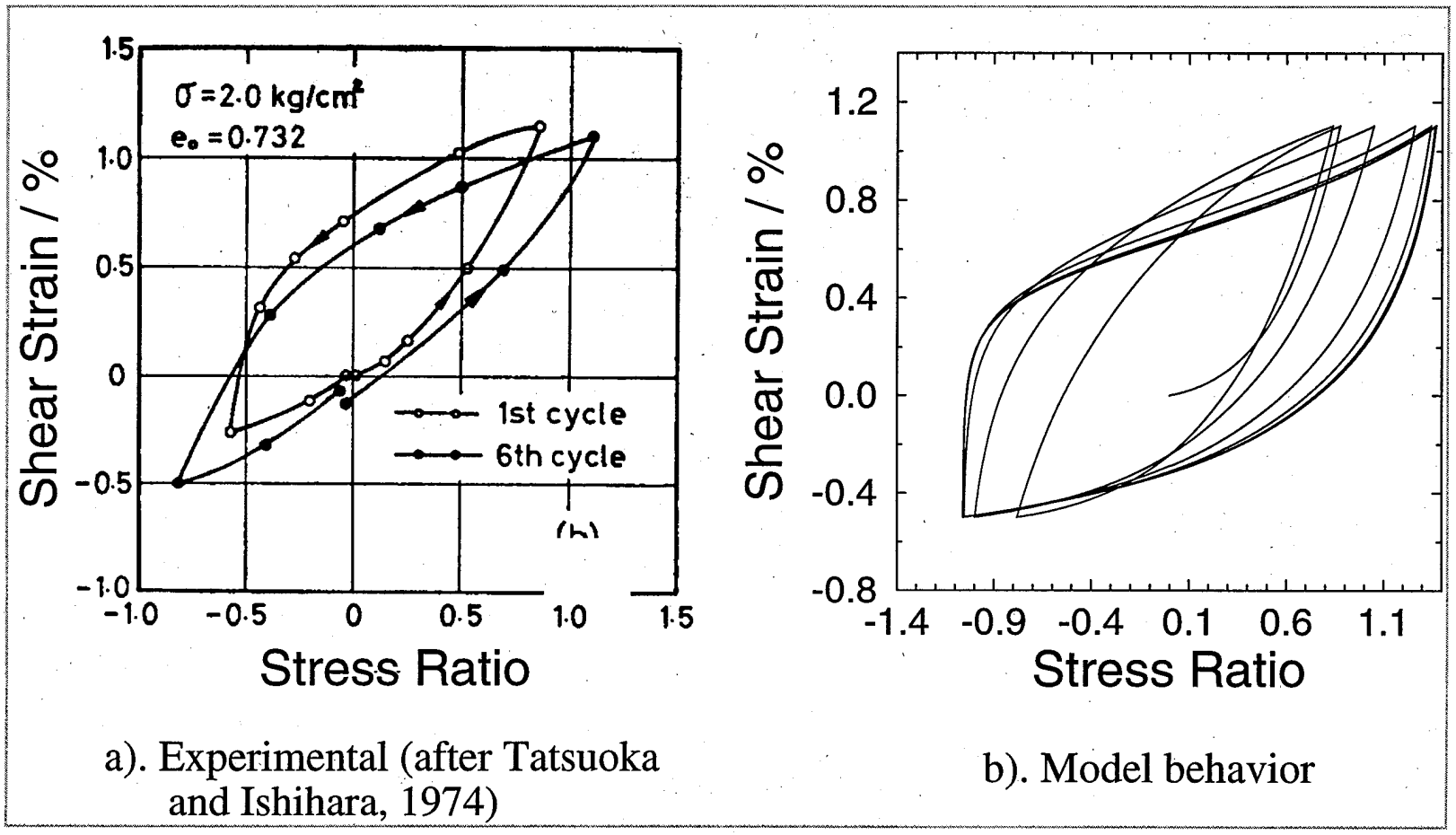

a). Experimental (after Tatsuoka and Ishihara, 1974)

b). Model behavior

FIGURE 14: Shear strain against Stress ratio under constant amplitude strain controlled drained cyclic triaxial test

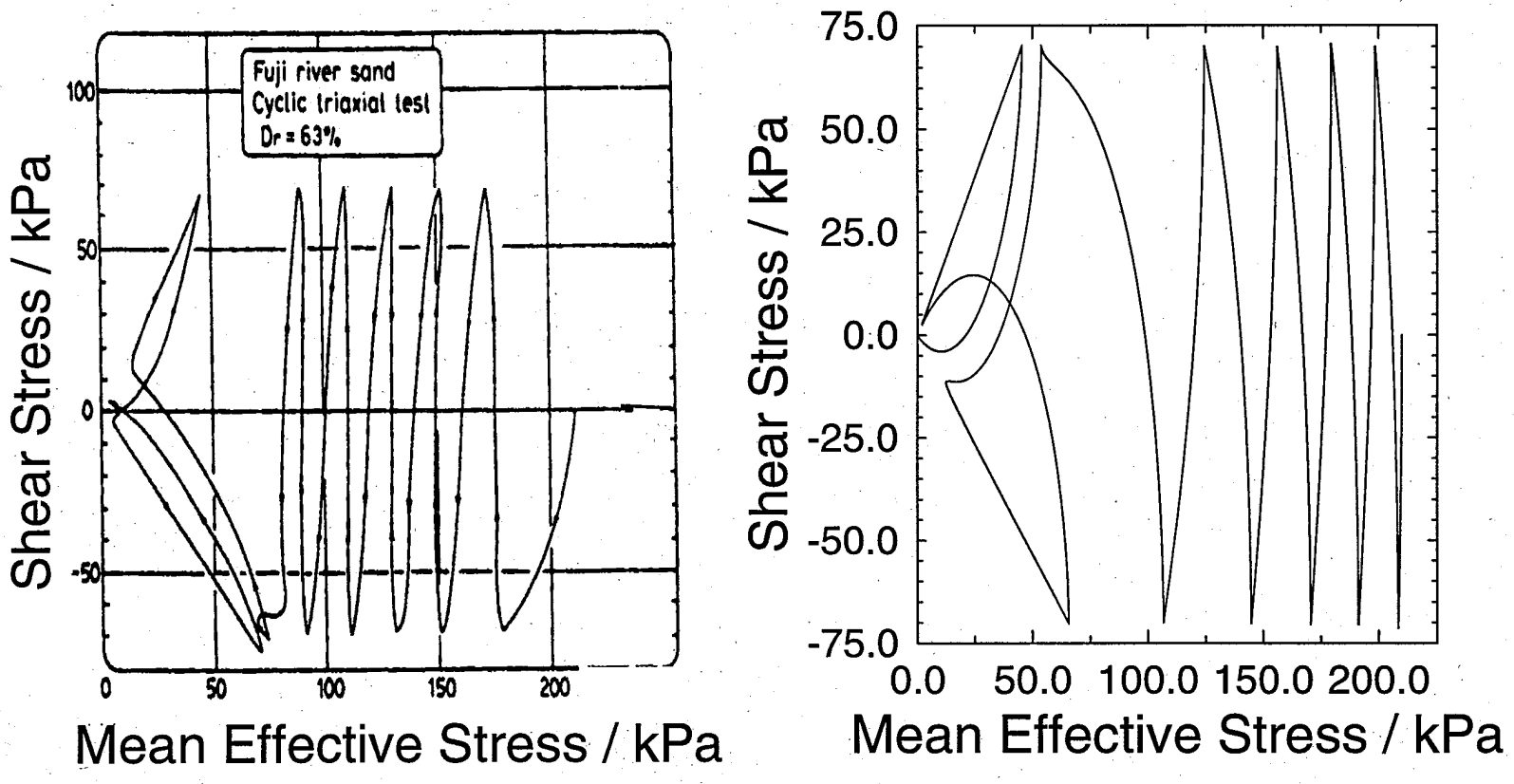

a). Experimental (after Ishihara et. al., 1975)

b). Model behavior

FIGURE 15: Shear stress against Mean effective Stress under constant amplitude stress controlled undrained cyclic triaxial test

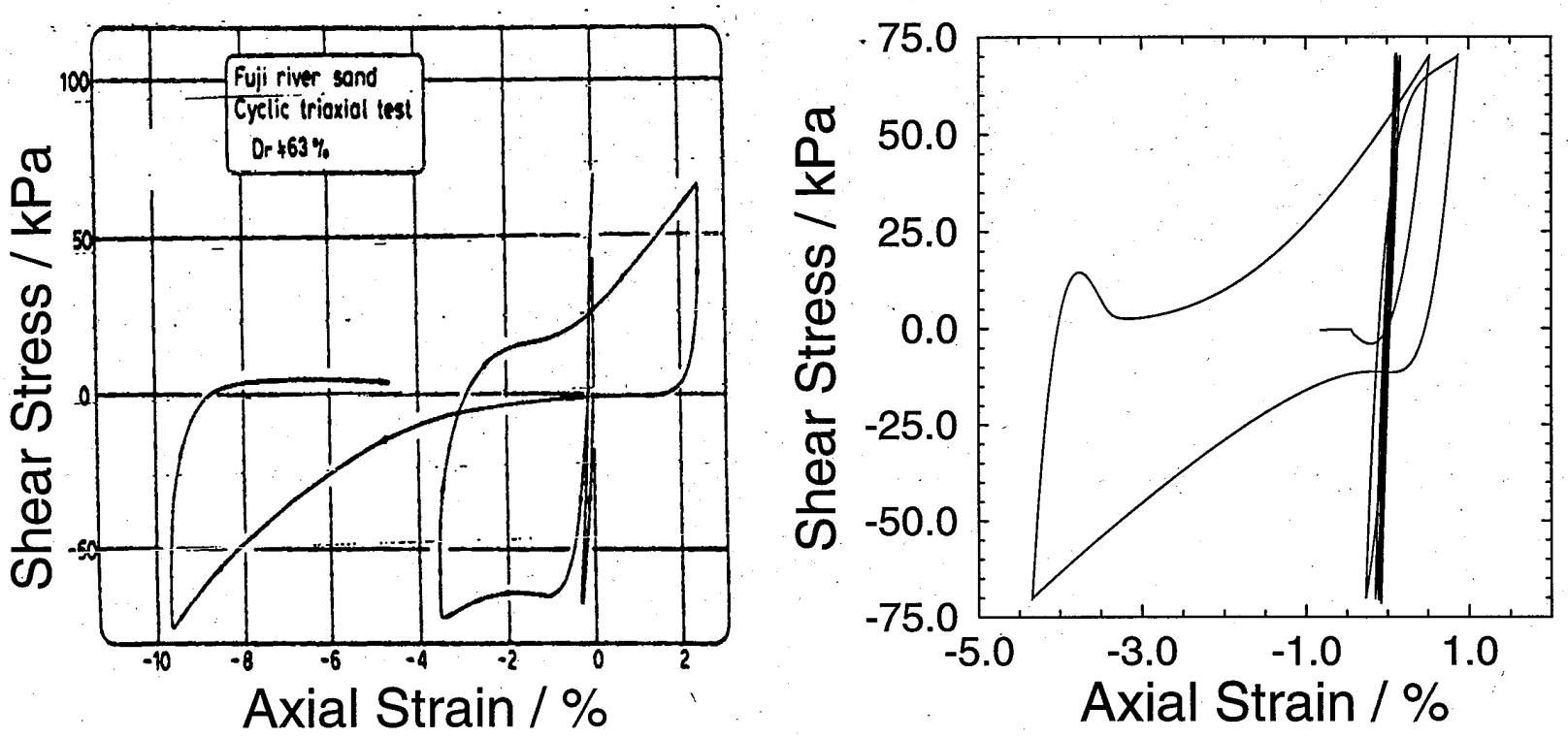

a). Experimental (after Ishihara et. al., 1975)

b). Model behavior

FIGURE 16: Shear stress against Axial Strain under constant amplitude stress controlled undrained cyclic triaxial test

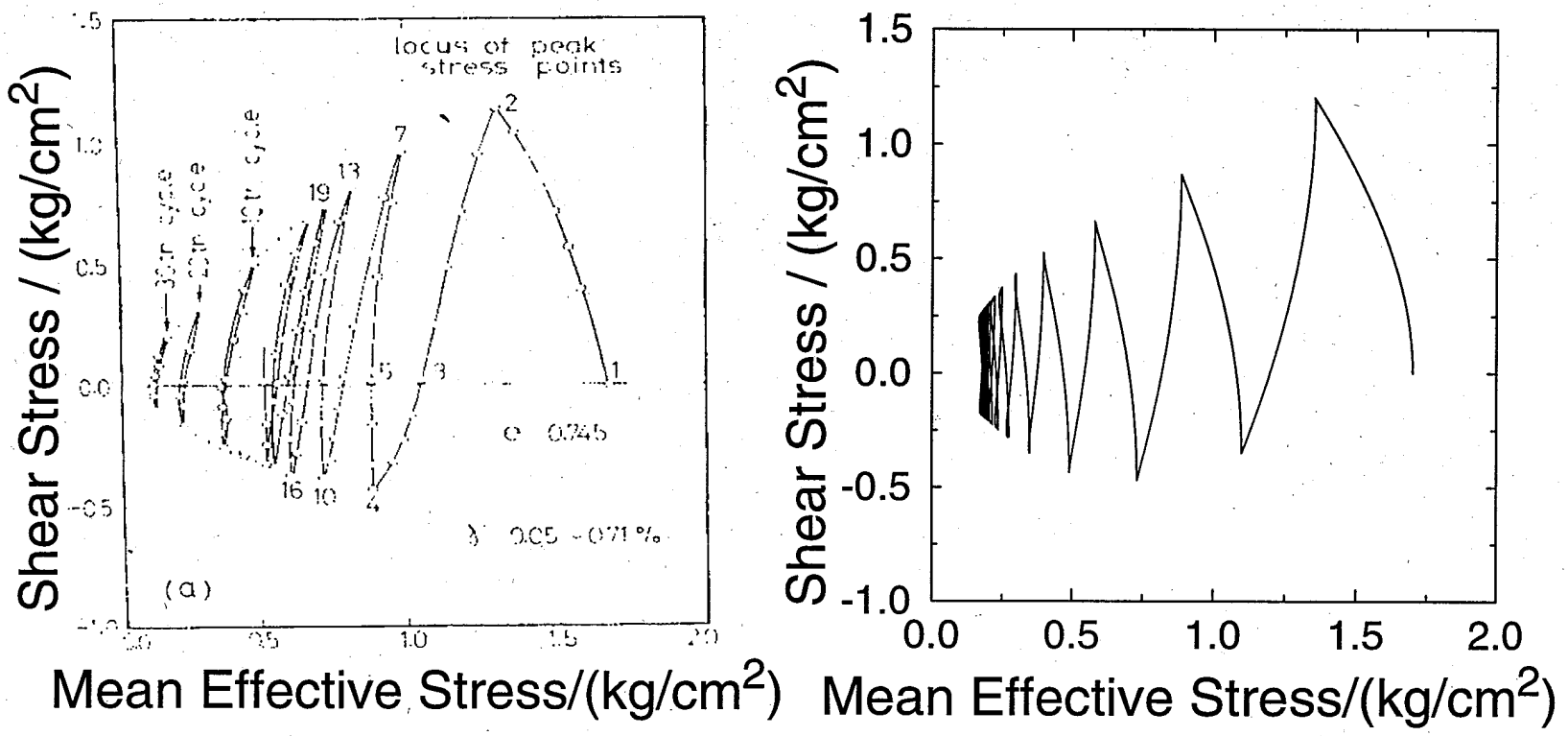

a). Experimental (after Ishihara et. al., 1975)

b). Model behavior

FIGURE 17: Shear stress against Mean effective Stress under constant amplitude strain controlled undrained cyclic triaxial test

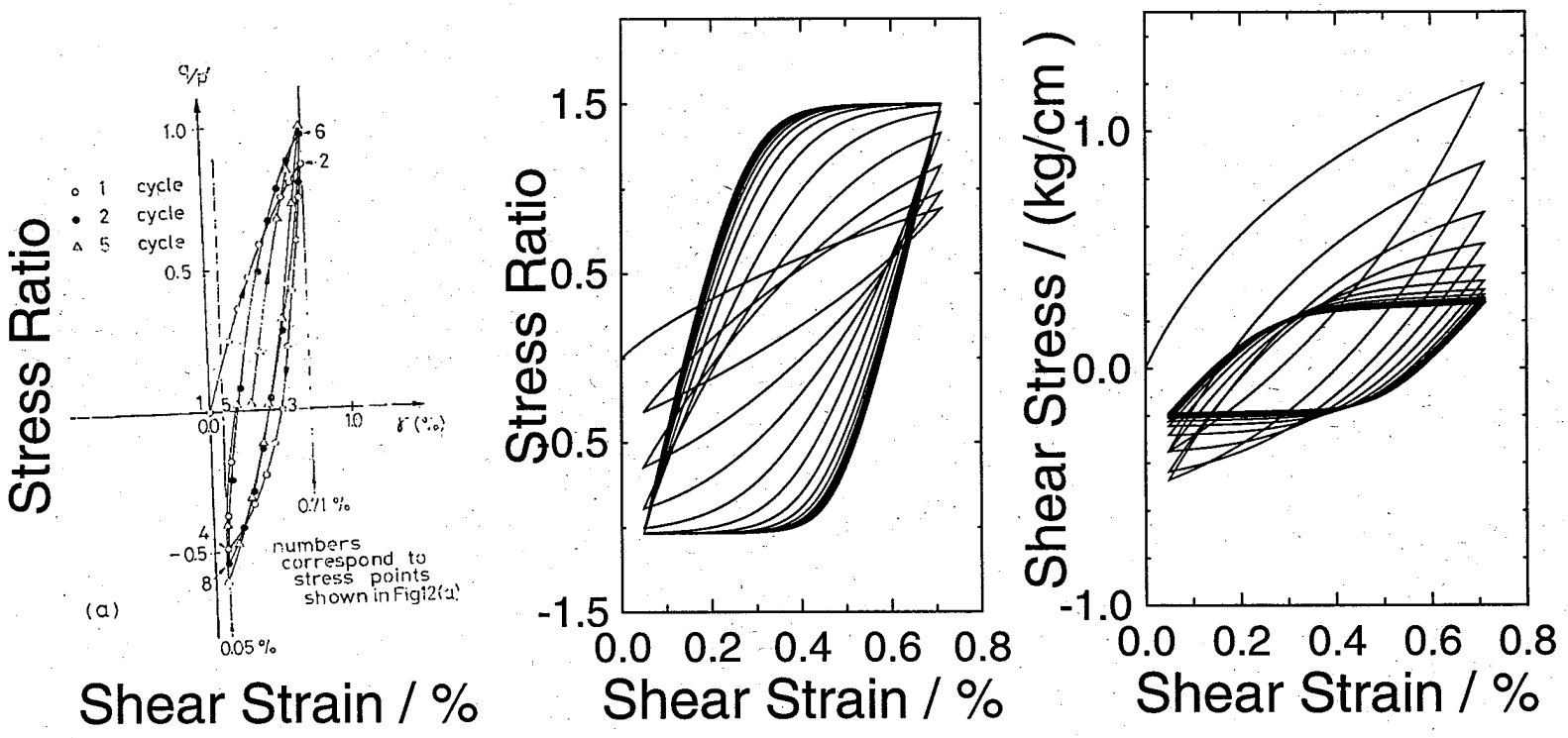

a). Experimental (after Ishihara et. al., 1975)

b). Model behavior

c). Model behavior

FIGURE 18: Shear stress against Axial Strain under constant amplitude strain controlled undrained cyclic triaxial test

Final Report
Prototype Field Compressometer

Geotechnical Engineering Program
Norwegian Institute of Technology

November 1994

Joint research effort between the University of Washington and the Norwegian Institute of Technology. Project funding by the United States Air Force (AFOSR - 91 - 0424) and the Geotechnical Division of the Norwegian Institute of Technology. Research stipend provided by the Valle Scholarship and Scandinavian Exchange Program, University of Washington.

TABLE OF CONTENTS

NOTE: These appendices are available upon request from:

Professor R. D. Holtz
Department of Civil Engineering
Box 352700
University of Washington
Seattle, WA 98195-2700 USA
Telephone: (206) 543-7614
Fascimile: (206) 685-3836
E-mail: holtz@u.washington.edu

LIST OF TABLES

LIST OF FIGURES

1.0 INTRODUCTION

The development of the field compressometer began in 1965 at the Norwegian Institute of Technology (NTH), and the final mechanical version of the device was completed in 1966 (Janbu and Senneset, 1973). In the following 5 years, Master's students at the NTH performed research to develop the analytical basis for the device. The current focus on the field compressometer is to render the instrument simpler and less expensive to use. By the installation of additional instrumentation, the amount and quality of the data may also be improved.

1.1 Objective

The objective of this project is to support the theoretical study of the field compressometer through experimental research. This experimental component consists of:

1. Measurement of the deformation patterns in soil beneath an embedded circular plate
2. Development of the field compressometer instrumentation
3. Laboratory and field proofing of the modified field compressometer
4. Gathering of existing field compressometer research data sets

1.2 Scope of Work

1.2.1 Measurement of deformation patterns

The measurement of the deformation patterns occurring in the soil beneath an embedded circular plate will provide a physical indication of the stress and strain processes underway during screw plate testing. The measurements will consist of the horizontal and vertical movements of various discrete points within the soil mass beneath the plate.

1.2.2 Development of the field compressometer

The physical development of the field compressometer consists of additional instrumentation as well as re-evaluation of the loading scheme and means for determining deformations.

The instrumentation of the field compressometer consists of the addition of a load cell directly in the instrument. In addition, the mechanical details of installing pore pressure measurements are being considered. The load cell will provide a direct means for determining load at the plate level, and the pore pressure transducer will provide a means for determining pore pressure dissipation characteristics.

1.2.3 Development of experience

Experience is developed by laboratory and field investigations using the field compressometer. The laboratory program includes the measurement of the overall vertical deformations of circular bearing plates as discussed in Section 1.2.1.

1.2.4 Historical data

A wealth of data exists at the NTH regarding previous screw plate testing both in the field and in the laboratory. The data available from field tests include documented test sites as well as performance data on structures constructed at locations where screw plate testing as well as other in situ testing has been performed. Since the fundamental aspects of the test is unchanged (geometry, loading procedure, etc.) the historical data is usable both for comparison with the data collected from the prototype instrument as well as adding to the available information for the development of constitutive models or analytical techniques.

2.0 FIELD COMPRESSOMETER EXPERIENCE AT THE NTH

This section presents a very brief overview of the available data and the nature of the research of the early investigators. The early work with the field compressometer was performed using the instrument shown in Figure 1. The available data from these investigations are included in the referenced appendices.

2.1 Fundamental Research

2.1.1 Berle (1968) and Fremstad (1968)

The focus of the work by Berle (1968) centers around the development of an analytical theory for interpreting field compressometer data. This interpretation technique is currently used in Norway for obtaining estimates of the constrained modulus. The estimate of the constrained modulus is described in Section 3.

Berle (1968) performed a short series of field tests to verify the interpretation technique. Additional field and laboratory tests were performed by Fremstad (1968). Several field compressometer tests were performed and settlement predictions were made for two typical geotechnical problems. The settlement predictions were then checked by constructing and instrumenting a small footing and a large fill.

The field tests were performed in the Øysand region (southwest of Trondheim), Drammen (southwest of Oslo) and a site in Trondheim. The available data for each of these sites is presented in Appendices B through D.

The laboratory tests were performed in Hokksund sand at various porosities and various depths using traditional loading schemes as well as cyclic loading. A review of the soil properties and test results for the Hokksund sand are listed in Appendix E. In addition, the deformation of 6 points on the screw shaped blade itself were measured under loads as high as 40 t/m^2. These deformations are shown in Figure 2.

2.1.2 Enlid (1970)

Enlid (1970) developed the Norwegian interpretation technique for estimating time rate of consolidation. The basis of the theory is axial and radial drainage of the soil directly beneath the plate during loading. The developed theory was subsequently checked using field test data and oedometer test data for sites in Stjørdal (east of Trondheim) and Steinkjer (northeast of Trondheim).

The useable data includes complete field compressometer data, routine laboratory data, oedometer test data, and measured settlements for a civil engineering project constructed at the Steinkjer site. This data is presented in Appendices F and G.

3.0 NORWEGIAN INTERPRETATION OF THE FIELD COMPRESSOMETER TEST

The procedures outlined in the following sections are currently used in Norway for the interpretation of field compressometer results. Estimates of moduli or consolidation coefficients presented in this document have been made using these techniques.

3.1 Deformation Estimates

3.1.1 The modulus concept

The existing analytical approach is based on the modulus concept. The constrained modulus M is defined directly from the oedometric stress-strain curve as:

$$M = \frac{d\sigma'}{d\epsilon} \qquad (1)$$

The relative deformation occurring at a depth is given by rearranging Equation (1) and integrating over the change in stress:

$$\epsilon = \int_{\sigma_o'}^{\sigma_o'+\Delta\sigma'} \frac{d\sigma'}{M} \tag{2}$$

The modulus can be described via a general formulation incorporating stress level and soil type as:

$$M = mp_a\left(\frac{p}{p_a}\right)^{1-a} \tag{3}$$

Where

M = modulus (kPa)

m = modulus number (dimensionless)

a = deformation exponent (dimensionless)

p_a= reference pressure of 100 kPa

The selection of the deformation exponent *a* is based on experience; approximate values for various soil types is shown in Table 1.

Table 1 Approximate values for the exponent *a*

a	Soil model	Soils
1	Equivalent elastic	Undisturbed tills, morainic soils, OC clay, undrained loading of clay, small compressive strains of sand
0.5	Equivalent elastic-plastic	Gravels, sands and coarse silt
0	Equivalent plastic	NC clay, fine silt, swelling of sand
<0	Sensitive	Sensitive soils

Equations (2) and (3) can be combined, and the integral solved to obtain ($\Delta p = \Delta\sigma$):

$$\epsilon = \frac{1}{ma}\left[\left(\frac{p'}{p_a}\right)^a - \left(\frac{p_o'}{p_a}\right)^a\right] \tag{4}$$

Equation (4) provides the basis for the modulus approach for ordinary soils and conditions.

3.1.2 Modulus approach as applied to the field compressometer

An idealization of the field compressometer installed in situ is shown in Figure 3. The plate settlement can be estimated by calculating the displacements in n discrete soil layers over the depth H and summing:

$$\delta = \sum_{i=1}^{n} \delta_i = \frac{H}{n}\sum_{i=1}^{n} \epsilon_i \tag{5}$$

Combining Equations (4) and (5) yields:

$$\delta = \frac{H}{n}\sum_{i=1}^{n} \frac{1}{ma}\left[\left(\frac{p_i'}{p_a}\right)^a - \left(\frac{p_{oi}'}{p_a}\right)^a\right] \tag{6}$$

With the addition of several multiplicative terms (the net result of which equal 1), Equation (6) can be rearranged to obtain:

$$\delta = \frac{B}{m}\frac{q_n}{p_a}\left\{\frac{1}{n}\frac{H}{B}\frac{p_a}{q_n}\sum_{i=1}^{n}\frac{1}{a}\left[\left(\frac{p_i'}{p_a}\right)^a - \left(\frac{p_{oi}'}{p_a}\right)^a\right]\right\} \tag{7}$$

The dimensionless settlement number S can be defined by:

$$S = \frac{h}{n}\frac{p_a}{q_n}\sum_{i=1}^{n}\frac{1}{a}\left[\left(\frac{p_i'}{p_a}\right)^a - \left(\frac{p_{oi}'}{p_a}\right)^a\right] \tag{8}$$

Where h = the ratio H/B

H = depth to plate

B = diameter of plate

Using the definition for the settlement number S Equation (7) can be rewritten as:

$$\delta = S\frac{Bq_n}{mp_a} \tag{9}$$

An alternate arrangement of Equation (9) can be used to obtain the modulus number where settlement data is known:

$$m = S\frac{Bq_n}{\delta p_a} \tag{10}$$

Figure 4 presents a graphical solution of the expressions for S.

3.1.3 Calculation of the modulus number

The data obtained from the field compressometer consists of time-deformation curves for increasing loads at depth. An estimate of the deformation corresponding to 100 percent consolidation is made using an accepted technique, such as Taylors construction. The resulting data is used to plot a load-deformation curve for the test depth.

The in situ vertical stress is then estimated, and a straight line is drawn from this pressure tangent to the load deformation curve as shown in Figure 5. The deflection and the corresponding nominal pressure p_n is taken at a midpoint on the tangent line. The settlement number S is taken from the graph for the appropriate soil type and value of p_n, and the corresponding modulus number is calculated.

3.2 Time Rate of Consolidation Estimates

The estimate of the time rate of consolidation coefficient is based on a radially draining oedometric model as shown in Figure 6. The cylinder is assumed to be permeable through the sides and impermeable through the top and bottom surfaces. The radius of the cylinder is taken as the radius of the screw plate.

From Terzaghi's three dimensional consolidation theory, the rate of change of excess pore pressure is given by:

$$\frac{\partial u}{\partial t} = c_r\left[\frac{\partial^2 u}{\partial r^2}+\frac{1}{r}\frac{\partial u}{\partial r}\right] + c_v\frac{\partial^2 u}{\partial z^2} \tag{11}$$

Where

$$c_r = \frac{k_r M}{\gamma_w} \qquad c_v = \frac{k_c M}{\gamma_w} \tag{12}$$

Assuming that the permeability coefficient and the modulus are constant, and considering that no flow occurs in the z direction, this equation reduces to:

$$\frac{\partial u}{\partial t} = c_r\left[\frac{\partial^2 u}{\partial r^2} + \frac{1}{r}\frac{\partial u}{\partial r}\right] \tag{13}$$

The boundary conditions can be stated as:

For $t = 0$ and $0 \le r < R$ $\quad u = \Delta p$

For $0 \le t \le \infty$ and $r = R$ $\quad u = 0$

For $0 \le t \le \infty$ and $r = 0$ $\quad \partial u/\partial r = 0$

For $t = \infty$ and $0 \le r \le R$ $\quad u = 0$

which lead to a solution of the differential equation as:

$$U = 1 - 4\sum_{n=1}^{\infty} \frac{1}{B_n^2} e^{-B_n^2 T_r} \tag{14}$$

Where B_n is a root of Bessel's function and the time factor T_r is given by:

$$T_r = \frac{c_r t}{R} \tag{15}$$

This solution is identical to the solution for an oedometer with radial drainage. For 90% consolidation, the factor T_r is 0.335 (Mc Kinley, 1961), and the radial consolidation coefficient c_r is:

$$c_r = T_{90} \frac{R^2}{t_{90}} = 0.335 \frac{R^2}{t_{90}} \tag{16}$$

4.0 DEVELOPMENT OF THE PROTOTYPE FIELD COMPRESSOMETER

The design of the prototype is based on three objectives: To simplify the use of the device, to improve the quantity and quality of the data, and to modernize the data acquisition from the device. These objectives represent the fundamental goal of the development of a new field compressometer -- to develop a tool which is practical and useful in ordinary field investigations and not limited to research applications.

Although many aspects of the field compressometer are being reconsidered, the fundamental principle underlying the device remains unchanged: the load-settlement interaction of a screwed down bearing plate. The prototype is therefore a refinement to the original device, rather than a fundamental change in the test itself. The results obtained from the prototype should be directly comparable to the existing body of data from previous screw plate testing.

4.1 Original Field Compressometer Developed at the NTH

The original version of the field compressometer was depicted in Figure 1. Figure 3 showed the field compressometer installed in situ. The field compressometer consists of three principle

components: The bearing plate, the load system and the instrumentation. Each of these components is briefly discussed below.

4.1.1 Bearing plate

The bearing plate consists of a bearing surface formed as a single helical screw with a diameter of 16 cm and a rise of 4.5 cm. The plate is constructed of cast iron for economy and simplicity of construction. The plate is attached to the body of the field compressometer via a weakened center screw. Four pins are included in the resulting joint to resist torsion during installation. The plate is abandoned at depth at the completion of the test series by breaking the center screw in tension. As a result, the plate itself does not carry any instrumentation.

4.1.2 Load system

The load system for the compressometer is a hydraulic jack contained within the body of the device at depth. The load is given by a reaction of the jacks against the drill rods and a reaction frame at the surface. The jack is located immediately above the level of the plate, as indicated in Figure 1. The reaction system for the jack is shown in Figure 3.

The hydraulic jack is located at the level of the plate to eliminate the effect of shaft friction of the drill rods. The jack is activated using compressed nitrogen supplied through pneumatic tubing from the surface. The pneumatic tubing is threaded through an inner set of hollow rods within the drill rods.

The pressure in the jack is controlled using a pressure accumulator and a precision manometer. The load acting on the plate is calculated from the pressure supplied to the hydraulic jack.

4.1.3 Instrumentation

The instrumentation for the field compressometer consists of a pair of dial gauges and a pressure gauge. The dial gauges measure the vertical movement of the plate relative to a reference beam at the ground surface. The hollow inner rod containing the pneumatic tubing for the jack is used as to transfer the movements of the plate to the surface. This rod is fixed to the ram in the hydraulic jack and is free to move vertically within the drill rods. The reference beam is supported independently of the reaction frame. The pressure in the jack is used to calculate the load applied to the plate.

4.2 Prototype Field Compressometer

The principle improvements planned for the original field compressometer are direct measurement of load at the level of the plate, simplification of the load application, simplification of the deformation measurement system, and modernization of the data acquisition system and the inclusion of pore pressure measurements. In addition, the prototype is fully recoverable at the completion of the test series.

The prototype field compressometer is discussed in the following sections. The prototype is sketched in Figure 7. Figure 8 shows the field set up to be used for the first round of field tests.

4.2.1 Bearing plate

The external shape of the bearing plate is relatively unchanged from the original design. A slight lengthening of the tip (approximately 5-7 mm) below the blade will be required to accommodate the pore pressure transducer. This change in geometry should not significantly effect the test results. The filter for the transducer will be installed in the plate assembly. The filter will be located on the cylindrical stem of the bearing plate as shown in Figure 7.

4.2.2 Load system

The addition of a load cell at the level of the plate has simplified the loading system required to run the field compressometer test. Since the load at the level of the plate is directly measured, it is possible to apply the load directly to the drill rods at the ground surface. The load can be applied using a hydraulic ram reacting against the drill rig. The simplification in load application is the result of the elimination of the in situ hydraulic jack, pneumatic cables, inner rods, pressurized gas cylinders, and the reaction frame.

The use of a drill rig for installation and extraction of the field compressometer necessitates the use of stronger drill rods. The drill rods are required to withstand compression, tension and torsion in both directions. The connections used for the drill rods are detailed in Figure 9.

4.2.3 Instrumentation

The instrumentation for the prototype consists of a load cell immediately above the plate, an LVDT located at the ground surface and a pore pressure transducer on body of the bearing plate blade. The data collected are pore pressures beneath the plate, load on the plate and vertical

deformations of the plate. The data collected at the level of the plate is transmitted to the surface using electrical cables threaded through the drill rods. The data are automatically recorded using a data acquisition system.

The load at the level of the plate is measured using the load cell. The load cell was manufactured and instrumented at the NTH. The load cell has been calibrated up to 40 kN.

The vertical deformation of the plate is measured using an LVDT and a simple reference system as shown in Figure 10. The system uses the same premise of a fixed reference level as in the original system. However, the proposed system has several advantages.

A distinct advantage is the decreased complexity of the reference system. This should reduce the time required for set up and adjustment of the reference level. In addition, since the data is collected electronically rather than visually, the reference level can be set to any convenient height. The reference level can be set sufficiently high to keep it clear of the work area. Another advantage is the elimination of movement in the reference level due to thermal effects. The effect of elastic deformation of the drill rod is negligible.

The data generated by the pore pressure transducer, the load cell and the LVDT are recorded using a portable PC running a proprietary data acquisition program developed for the field compressometer.

4.3 Load cell calibration

The load cell in the prototype was calibrated using a calibration device originally developed for the CPT. This device was used for a coarse calibration, and a finer calibration of the first 2 kN range of the load cell was conducted using dead weights.

5.0 PRELIMINARY LABORATORY TESTS

5.1 Facilities

5.1.1 Foundation laboratory

The Geotechnical Division of the NTH has a rather unique facility for testing large scale (or full scale) models in a controlled laboratory environment. This laboratory consists of large concrete tank (4 x 4 x 3 m), 80 tons of sand and an automated system for handling the sand.

The sand is placed in the tank by raining out of a mechanical spreader which passes back and forth over the tank at a steady rate of 8 cm/sec. The sand is delivered to the mechanical spreader

via a system of silos and conveyor belts. The sand is removed from the test tank through a number of chutes equipped with mechanical vibrators at the bottom of the tank. The sand is returned to the storage silos by conveyor belts. Emptying a full tank of sand requires approximately ten hours of continuous operation. Filling time varies depending on the porosity, and may range from 10 to 30 hours.

The raining of the sand (and consequently the porosity) is controlled by the diameter of nozzles placed in the bottom of the spreader. The available nozzles range in size from 5 to 20 mm. The corresponding porosities range from 37 to 43 percent. Experience gained at the NTH over years of operation has shown that the sand distribution system produces relatively uniform porosity throughout the depth of the tank.

5.1.2 Hokksund sand

The soil used in the model test facility is a quarry sand obtained from Hokksund, Norway. This sand has been geotechnically well documented. The properties of the sand are listed in Table 2, and the grain size distribution is shown in Figure 11. Additional geotechnical data for the sand is presented in Appendix E.

Table 2 Hokksund Sand

Routine Data					
Minimum porosity (%)	Maximum porosity (%)	Density soil solids (g/cm^3)	C_c	C_u	Water content %
36.4	48.7	2.712	1.23	2.04	0
Mineral Content, %					
Quartz	Feldspar (Sodium)	Feldspar (Potassium)	Mica	Amphibole	Other
35	25	20	10	5	5

5.2 Test Equipment

The principle pieces of required equipment are listed below. Minor appurtenances are not include in the discussion.

5.2.1 Bearing plates

The bearing plates have diameters of 16 cm and 30.7 cm, and have a thickness of 1 cm. The plates are common steel. The plates are concentrically attached to hollow steel rods. The rods have an outer diameter of 42 mm and an inner diameter of 38 mm.

Shaft friction is reduced to approximately zero by a plastic sheath (PVC pipe) surrounding the rod. The ends of the sheath are sealed by a circular steel shim that fits in between the inner wall of the PVC and the outer wall of the steel rod. The upper shim is removed prior to testing.

5.2.2 Field compressometer

The field compressometer will be used in essentially field configuration. The variation from field configuration will be the use of a drill rod modified to be used in the laboratory. The modified portion will remain above the soil surface throughout the test and will not alter the performance of the device.

5.2.3 Loading system

Two loading systems are used for the various test series. In the first system the load is applied using a hydraulic jack; in the second system it is applied using dead weights.

5.2.4 Measurement

Deformation measurements are taken using both dial gauges and an LVDT. The dial gauges used in the first two test series had a sensitivities of 0.1 mm; the gauge used in the last test series (small deformation series) had a sensitivity of 0.01 mm.

6.0 LABORATORY TEST RESULTS

The results from the various test series in the laboratories can be considered as two primary subjects. First is the deformation patterns occurring beneath flat circular bearing plates. The second is the load-deformation response of flat circular bearing plates and screw shaped bearing plates. These two areas are presented in turn below.

6.1 Deformation Patterns Beneath Circular Bearing Plates

Various tests were conducted to measure deformation patterns in the soil beneath bearing

plates. These tests were conducted as part of two separate test series. For both of these test series, the load was applied using a hydraulic jack.

In the first test series (conducted by Kvalsvik, 1991), three soil densities, two plate diameters and two embedment depths were used. In the second series (conducted by Hoff, 1993), three soil densities, one embedment depth and one plate diameter were used.

6.1.1 First experimental series

The plate diameters used in the first experimental series were 16 cm and 30.7 cm, which corresponds to bearing areas of 201 and 740 cm^2. The soil densities used were: a relatively loose soil with an average porosity of approximately 43 %, a medium density soil with a porosity of approximately 40 %, and a relatively dense soil with an average porosity of approximately 37 %. For each combination of plate diameter and soil density, two embedment depths were tested. For all combinations, the shallow depth of embedment was 1 m. For the tests in dense soil, the deep embedment depth was 1.5 m. For the other soil densities, the deep embedment depth was 2 m.

Measurements of the deformations were made by placing small metal plates (5 cm diameter) in the soil during filling of the tank. The plates were attached to copper wire which was run to the soil surface through flexible tubing and attached to dial indicators. A total of six plates (3 horizontal and 3 vertical) were used for measuring deformations under each bearing plate as indicated in Figure 12.

Although the deformations are measured in different locations, it is assumed that symmetry in the deformation pattern around the circular bearing plate exists. This assumption allows the reduction of the data to depict the horizontal and vertical displacement of three distinct points in two dimensions. The deformation data for this test series is presented in Figures 13-16. Figures 13 and 14 illustrate the deformations in true scale, Figures 15 and 16 present an amplification of the data.

6.1.2 Second experimental series

In the second series, the same soil densities are used for the loose and the dense cases, and a average approximate porosity of 38 percent is used in the medium case. For this test series only one diameter of bearing plate (16 cm) and one embedment depth (1 m) is used. In this test series the deformations occurring in a spatial distribution beneath the plate.

Figure 17 shows the measurement locations. The deformations were measured using Kvalsvik's (1991) method. Symmetry is assumed for presenting the data. In addition, the assumption is made that adjacent tests under controlled conditions will have the same deformation patterns. In the test series, only 6 deformation plates were placed beneath each bearing plate. However, the bearing tests were repeated four times in each density, and the aggregate data is presented together as the deformation pattern under a single bearing plate.

The deformation patterns measured in each density are indicated in Figures 18 - 20. The deformation data is presented in amplified form in Figures 21 through 23. For these plots, the initial point is indicated in true scale, and the subsequent vertical and horizontal deformations are increased by an order of magnitude.

6.2 Load-Deformation Response of Circular and Screw Shaped Bearing Plates

The load-deformation response of the various bearing plates and the screw shaped blade of the field compressometer were measured in all three of the experimental series. The first two series concentrated on larger loads, typically reaching a fully mobilized state with relatively large deformations occurring. The final test series focused on smaller loads and the corresponding deformations in an attempt to capture the approximately elastic response of the bearing plates during the initial stages of loading. A hydraulic jack applied the load, while dead weights applied the load in the low and medium density sand in the final test series. The capacity using this method was not sufficient for the dense condition, so a small hydraulic jack was used for the tests in the dense sand in the final series.

6.2.1 Large deformations

The first test series (Kvalsvik, 1991) did not incorporate tests with the screw shaped blade, rather it was intended to focus on the effect of changing the diameter of the bearing plate and the effect of embedment depth on the tests performed in the model test lab.

The vertical deformation of the bearing plates in the three soil densities for the first test series is depicted in Figure 24. Figure 25 presents the same data with a reduced range of vertical displacements axis. The data series marked with an asterisk are indicated as questionable by Kvalsvik (1991). Kvalsvik (1991) noted that for the 16 cm plate at 2 m embedment in the medium density soil, the dial gauge was disturbed during placement of the first load. This altered

the null point. The 30 cm plate at 2 m was indicated as having been placed poorly, resulting in difficulty in applying load to the bearing plate.

The results from the second test series are presented in Figures 26 through 28. In addition to the bearing plate tests, several field compressometer tests were also performed. This data is included in Figures 26 through 28. The field compressometer was installed by screwing into position.

6.2.2 Small deformations

The third test series utilized both bearing plates and the field compressometer. The intention of this test series was to examine the load deformation response of the two plate shapes to small stresses and strains in the surrounding soil. Small loads and little load steps were used for these tests.

At first, it was assumed that the hydraulic jack could be used to apply the loads. However, the first test in loose sand indicated control problems with the system under very small loads and load increments. The hydraulic pressure control was simply too coarse and the jack too large.

The alternate load scheme (using dead weights) increased the precision of the loading system. It was found, however, that in the dense condition, the mechanical management of the dead weights became a problem. A small high quality hydraulic jack replaced the dead weights to conduct the final three tests. The system proved very satisfactory, and will be used in future bearing plate tests in the laboratory.

Bearing plate, loose soil

Figures 29 and 30 present the bearing plate load-deformation data. The first test presented in Figure 29 was loaded using the large hydraulic jack system; the control problem is readily apparent. In Figure 30, which details the lower strain portion of the curves, it is evident that the soil in the first test appears to have higher strain at equivalent stress levels. This response may be due to disturbance during the installation of the jack and the weight of the jack itself.

In the previous test series, the jack had been mounted on top of the bearing plate rods. The installation of the jack was rather difficult due to the confined work area and the large mass of the jack (50 kg). Movements of the drill rod and impacts to the drill rod perhaps have affected this data. The weight of the jack on top of the drill rods is not included in the load applied to the

plate. If the stress due to the weight of the jack is considered (approximately 25 kPa), the entire curve shifts upwards and becomes coincident with the second test.

Field compressometer, loose soil

Three field compressometer tests were run at this density. The method for conducting the first two tests is identical to the second bearing plate test. In the third test, an alternate deformation measurement system was used. The alternate method eliminated the need to physically contact the load frame while reading the dial gauges. Copper wire and pulleys allowed the dial gauge to be placed well away from the load frame. As the data indicates, this alternate system did not work.

The data for the field compressometer tests are shown in Figure 31. In the second test, a small rebound loop occurs at 30 kPa and the loading continues to a higher level than in the first test. The reproduction of the data between the first and second tests is very good. In the third test (which used the alternate measuring scheme), the dial gauge did not initially respond but after some loading had occurred (and some deformation is assumed to have occurred) the dial gauge began registering deformation. It is possible that the initial deformations were lost due to slack in the wire. If the shape of the curve for the third test is compared to the first two, it is seen that both the shape of the curve and the proportional changes in deformation to load are very similar.

Bearing plate, medium sand

The bearing plate test results are shown in Figure 32. The initial portion of the curves are in good agreement and the overall slope of the curves is approximately 1.5 times that found in the loose sand. In the mid portion of the curves, however, the first test continues at approximately the same slope and the second test shows strain softening behavior.

Field compressometer, medium sand

The data for the field compressometer tests is presented in Figure 33. As can be seen in this figure, the shape of the curves and the rebound response does not appear to be consistent with the bearing plate results at this density nor with the results from bearing plate field compressometer tests in the loose soil. In addition, the curves are not characteristic of Hoff's (1993) field compressometer tests at the same density. This data will be further discussed in Section 8.

Bearing plate, dense sand

A small hydraulic jack applied the load for the tests in dense sand as the dead weights could not provide enough force. A small jack and a new mounting method eliminated the problems with load control and self weight.

The load deformation response of the bearing plates in the dense sand is shown in Figure 34. The data from the two tests do not correlate with each other very well. This may be due to disturbance of the second bearing plate. A fairly significant period of time passed between installation and testing. During this time, the laboratory was open for other activities. The first bearing place was protected within the steel load frame, however the second bearing plate was vulnerable. It is conceivable that the plate was disturbed in some way. These tests results should be verified by additional tests.

Further, the overall response does not match well with the overall response obtained by others (Kvalsvik, 1991 and Hoff, 1993). The initial portion of the load-deformation curve for the first test does compare favorably as the modulus number estimates in Section 6.3 show. The reduced stiffness portion of the curve also compares favorably; the primary difference is in the apparent yield point.

Because of the changes in the loading and data collection systems, it is possibly that unforseen system compliance has been brought into the picture. The compliance may manifest itself in distortion of the load frame, which in addition was the reference for the deformation measurements. It was assumed that the low load levels combined with the robustness of the load frame would yield a stable reference system. It is possible that this was not the case, and some system compliance was introduced. When the tests are repeated to resolve the variation between the two existing tests, the deformation system will be mechanically isolated from the load system.

Field compressometer, dense sand

A single test using the field compressometer in this density was run. The data is presented in Figure 35. Again, the data for the field compressometer test under laboratory conditions appears to be rather unusual. The initial stiffness is extremely low as is the stiffness in the rebound loops. It is interesting to note that the data (using this interpretation scheme) seems to indicate that the soil yields more energy during unloading than what is put into it during the loading cycle. This is further discussed in Section 8.

6.3 Modulus Estimates

Figure 36 shows modulus estimates from the three test series as well as from oedometer tests. The procedure used for estimate the modulus follows standard interpretation procedures for the oedometer data, and a consistent application of the field compressometer interpretation method for the bearing plate and field compressometer data. The interpretation used the stress associated with the first 1 mm of deformation of the plate to estimate the modulus number.

The figure shows that the modulus from the oedometer test is higher than for either the bearing plate or the field compressometer. The modulus number from the bearing plate tests seem to follow a fairly consistent trend -- decreasing with increasing porosity which is reasonable. The field compressometer data yielded lower moduli at the densest conditions, a peak for the medium tests and a modulus number consistent with the bearing plate tests at the highest porosity.

We can reasonably accept that the modulus values from the bearing plates are less than the oedometer tests, because the level of lateral confinement in the free field is probably is not equivalent to the level of lateral confinement in a steel oedometer ring. Further, we can also accept that the field compressometer data would yield higher modulus numbers, since the simple approach for interpretation does not incorporate the increase in mean effective stress around the blade during insertion. The stress increase results from both the physical displacement caused by the blade as well as the possibility of dilation in the soil. The modulus should be higher under higher confining stress.

The drastic decrease in the modulus number for the dense sand poses a problem. If the factors above are the only influencing factors, than the decrease in modulus is inexplicable. There must be other effects decreasing the modulus. Possible explanation is presented in Section 8.

6.4 Deformations Based on Elastic Theory and Finite Element Analysis

Elastic analyses using Nishida's (1966) solution as well as finite elements to predict the vertical centerline displacement of the embedded bearing plate are shown in Figure 37 (Hoff, 1993). The selection of the elastic parameters for both was based on oedometer test results.

This analysis was rather simplistic in approach and is perhaps inappropriate for this problem. The magnitude of the displacements (more than 4 cm) may be well beyond the elastic or semi elastic range, and the soil may be better described as in a state of failure.

Further analyses are not within the scope of this project; however a potential direction may be

proposed. Nordal (1983) has studied the elasto-plastic behaviour of soils using a finite element model. The study consisted of a strip load placed on a homogeneous soil deposit. Four cases are presented: Tresca criterion with and without self weight, Coloumb criterion with and without self weight. The stress distributions and the velocity fields developed by the finite element programs may be useful as a guide for further interpretation of the data from the test series using higher levels of deformation, and hence, large strain levels. An example of the results obtained by Nordal (1983) for the bearing capacity problem using Coulomb criteria and self weight is shown in Figure 38.

The data from the small deformation tests is probably more appropriate for an elastic analysis. However, this data has not been subjected to rigorous analysis at this time.

7.0 PRELIMINARY FIELD TESTS

7.1 Introduction

The first field use of the field compressometer is in a man made fill/natural silty clay deposit in a field near the laboratory. The fill material is known to be morainic material with a substantial clay fraction. These tests were to evaluate the set up and use of the field compressometer under field conditions. Emphasis was not placed on the actual data collected and the analysis of that data, rather it was placed on the convenience of having the support of the machine shop during the proof testing of the instrument. Although the laboratory was immediately at hand, the proof testing was approached as if the testing program was being conducted at a remote field site. All equipment was mobilized including the field trailer.

Tests were run at depths of 1 to 5 m in two profiles. In general, the initial tests went badly due to numerous minor problems. The minor problems included general inexperience with the device, calibration errors, electronic equipment failure and terrible weather conditions. These problems are easily corrected (or in the case of the weather, tolerated) and appropriate measures have been taken.

In addition to these minor problems, we found a problem with controlling the load applied by the drill rig. The original loading scheme had been to use the hydraulics on the drill rig to apply the load. During the tests it was determined that fine enough control could not be maintained. The Institute's drill rig is a piece of research equipment, and as such it is very well maintained and is in excellent condition. It is likely that control over the hydraulic systems in this rig is

better than what could be reasonably expected from equipment used in industry. As a result, it is not appropriate to develop the equipment to be dependent on the loading ability of the installation equipment. The use of a separate hydraulic ram to apply the forces may have to be evaluated.

These problems are depicted in Figures 39 through 42 which present data from one of the tests performed. Figures 39 and 40 are time histories of load and deformation for the first load increment which was simply the dead weight of the drill rig crosshead. Figures 41 and 42 indicate the time histories for the remaining hydraulically applied load increments. The data shown in these figures is not typical; in fact the data is the very best data available from the tests

The load in Figure 39 drops from an initial load of 150 kg (corresponding to a stress level of 75 kPa under the plate) to a final load of approximately 128 kg (64 kPa) at the end of the load increment. The decrease in the load at the plate occurs correspondingly to increasing deformations of the system shown in Figure 40.

Figure 41 and 42 show the response when the load is applied using the hydraulic system on the drill rig. The load was applied in three steps, the first at 300 kg, the second at 530 kg, and the third at 780 kg. The loads were not predetermined; we simply tried to adjust the hydraulic pressure in the system by small increments (which was not very successful). The plate was then unloaded in four steps. The variation in the load and its effect on the deformation is apparent from the figures.

The load applied to the plate must be maintained at a relatively constant level during each load step. In addition, the entire load increment should be applied over as short of a time interval as possible. These factors will become even more critical in later developments of the instrument which may include applications in cohesive soils for in situ consolidation tests.

It is readily apparent from this experience that a different approach must be taken for the application of the load to the field compressometer. The use of the hydraulic system on the drill rig does not provide adequate control of the load and the changes of load over time must be compensated for.

Further, there is apparently a more fundamental problem to be addressed: The effect of friction and load distribution throughout the soil system surrounding the entire field compressometer.

8.0 DISCUSSION

The results of the field compressometer tests in medium and dense sands resulted in rather peculiar data. The available data is the deformation of the system (measured from the top of the drill rod), the load at the top of the rod and the load at the plate.

Figure 43 presents this data in three separate plots. The first is the overall system response (load at the top of the rod and the measured deformations), the second is the plate response (load at the plate and the measured deformations), and the third is the difference between load at the top and the plate, which is the load taken by friction along the drill rods.

The first plot in the figure has the expected shape for a load-deformation curve, based on experience with the bearing plates in this soil. The soil has an initial stiff response, followed by less stiff response and rebound curves which recapture the initial stiffness.

The second plot represents the interesting data: The load at the plate versus deformation. However, we note first that the initial portion of the curve is not the stiffest, and that after some deformation the stiffness increases. Further, the rebound loops exhibit less stiff behavior than the virgin loading. The loops also indicate that the system has gained some extra energy.

The third plot shows the friction acting along the drill rods versus deformation. It is interesting that the load increases over 0.2 to 0.3 mm, reaches an ultimate value, and deformation continues at this ultimate value. When unloaded, the response is a fairly typically shaped rebound loop.

Plots of the friction versus deformation for all of the field compressometer tests run during the small deformations test series are presented in Figure 44. In this plot we see a common pattern in all of the tests - the soil along the rods deforms, picking up greater and greater load, until the maximum capacity is reached and the soil then deforms at constant load. The maximum load is generally reached at 0.2 to 0.3 mm of deformation.

The first indication of the effect of the friction came during installation, although the significance of the presence of the friction was not realized until the data was plotted in Figure 43 as discussed above. The pitch of the blade did not control the rate of penetration. The downward movement of the instrument during rotation was less than the pitch would indicate. This effect increased with increasing depth. This is the first indication of the effect of frictional forces.

Installation of the screw plate is a balancing of forces. The downward force is applied by the soil above the plate as it is compressed by the rotation and pitch of the blade. This force is resisted by friction acting along the drill rods. The blade advances when the force on the upper surface of the plate is great enough to fail the soil along the drill rod and to permit the drill rods to move downward.

The data for the field compressometer tests in both the medium and dense sands showed an initial deformation without significant load being taken by the plate itself (cf. Figures 33, 35 and 43). This deformation may be in part due to the gap remaining under the screw plate after installation where the blade does not advance at the same rate as the pitch of the blade would dictate.

Another source of deformation without any load at the plate may be displacement within the load cell itself. A small amount of vertical play is designed in the field compressometer in order to protect the load cell. The slack designed into the device is on the order of 0.1 to 0.2 mm. If the blade must pull the drill rods through the soil, the body of the field compressometer will be extended to include all of this play.

A third source of influence on the initial portions of the curve is the effect of the friction . As Figure 43 shows, the load on the plate is controlled by the stiffness and plastic deformations of the soil along the drill rods.

These mechanisms can be understood by thinking through the first load steps at the test depth. When a small load is applied (less than required for failure of the soil along the drill rods) the deformation of the system is controlled by the shear stiffness of the soil surrounding the drill rods. The small amount of deformation which does occur is absorbed by the slack in the load cell and the gap under the plate. The soil beneath the plate is not loaded. With increasing load, the shear deformations increase, eventually the plate begins to take load, and the system response then begins to reflect the response of both the soil around the drill rods and underneath the plate.

Once load reaches the plate, the load does not remain absolutely constant with time, even when using dead weights as the load source. The measured load decreases slightly over time. This was most noticeable in the field tests (cf. Figures 39 and 40). In order for the load to remain constant, the plate must be able to freely move as the deformations of the soil under the plate occur. However, the friction acting along the drill rods prevents the system from moving freely. Instead a complicated balancing of forces and soil stiffness occur. As the soil deforms, the load on the

plate decrease, and the load carried along the rods in friction increases. Additional load is taken as rod friction and the movement of the system, hence the changes in deformations measured at the surface, are controlled by the shear deformation and the shear failure that occurs along the drill rod. In order to restore load to the plate, the shear capacity of the drill rods must be exceeded and the drill rods must move downward through the soil.

These changes, although not particularly large relative to the load, may prove to be significant, especially in an insitu oedometric context for clays. Oedometric testing requires control over the boundary conditions, either through constant load, constant rate of strain, or constant pore pressure ratios. The variation in the load that occurs is a function of the strain rate of the soil, possibly pore pressure dissipation, ultimate capacity of the soil around the rod, slip mechanisms along the rod, and perhaps many other variables. Uncontrolled boundary conditions will compound the difficulty of the analytical solution and interpretation of in situ oedometer tests.

The field compressometer, in the prototype configuration, is actually testing the response of a soil system consisting of the soil surrounding the plate and the drill rods from plate level to the ground surface. The response of the system consists of shear stress along the drill rods, and vertical stress applied by the plate. This is a complicated system to analyze as the boundary conditions are unknown, or even where the boundaries of the problem actually are located. This is further complicated by the changes in load which occur. Perhaps the friction can be reduced using friction reducers or drilling mud. Again, the problem of increasing the complexity and reducing the desirability of the test comes into play.

These variations in the load can be monitored and corrected during the course of the field test. Perhaps a closed loop control system effectively connecting the load cell to the hydraulic jack via a pc would be able to maintain constant load at the plate level. However, this monitoring and control will only add complexity to the test. The objective of this research is to simplify and produce a useable field instrument, not to create a mechanical and computational nightmare.

9.0 SUMMARY AND CONCLUSIONS

9.1 General

The field compressometer was originally developed at the NTH during the mid 1960s as an in situ test to estimate the load - deformation response of difficult to sample soils. The design of the device incorporated the concept of simulating actual working stress - strain relationships

in the soil as closely as possible. Experience at the NTH has shown that the device does produce good test results and the engineering predictions made from the data provide reasonable estimates of actual settlement behavior. The testing technique does hold a lot of promise. However, the relative complexity of the test has prevented the development of much interest in the device.

It is reasonable to conclude that if the means for conducting the test are greatly simplified, the attractiveness of the test (an in situ plate load test) will increase to the research and consulting industry. The addition of other soil parameters available from the test (time rate of consolidation of clays, for example) will only add to the attractiveness of the instrument. Perhaps the field compressometer would then undergo the same rise in interest and research effort that the cone penetrometer test has experienced, and could potentially be developed into a commonly used field investigation tool.

9.2 Laboratory and Field Investigations

The initial work in the laboratory has indicated that the use of small load increments and low strain levels may provide interesting and useful data for interpreting soil response to buried circular plates. This is directly related to the problem of the field compressometer, which is essentially an in situ bearing plate test. The work provides sound data for developing interpretation procedures.

The proof testing indicated that the new drill rods and the tension cable reference system performed very well. The installation and removal of the field compressometer was very simple and much faster than the installation using the original equipment. The deformation system was also easy to set up and was stable throughout the test series.

9.3 Friction

The interaction of the drilling rods and the surrounding soil has proven to be an important factor in the prototype field compressometer. The stiffness and strength of the soil surrounding the drill rods control the load reaching the plate, and the stiffness of the same soil controls the deformation of the plate. the load to the plate can generally vary with time depending on the rate of deformation and the relative stiffness of the various soil components.

The use of friction reducers or drilling mud may reduce the effect of the friction, but is not likely to eliminate it. The use of such methods would also complicate the test.

9.4 Data

The data relevant to this study, as well as the data from related field compressometer studies, is presented in the appendices. A short glossary of Norwegian terms is included in Appendix A to assist in the interpretation of this data.

10.0 BIBLIOGRAPHY

Berle, Øyvind (1968). Development of the theory for the field compressometer with subsequent in situ tests and proof fills, Master's thesis, Geotechnical Division, Norwegian Institute of Technology, Trondheim, Norway (in Norwegian).

Enlid, Eystein (1970). A theoretical and experimental study of the field compressometer's useability for the in situ determination of load and time parameters, Master's thesis, Geotechnical Division, Norwegian Institute of Technology, Trondheim, Norway (in Norwegian).

Fremstad, D. (1968). Testing of the field compressometer in the laboratory and in situ. Predictions and analysis of a proof fill, Master's Thesis, Geotechnical Division, Norwegian Institute of Technology (in Norwegian).

Hoff, Inge (1992). The field compressometer - a theoretical and experimental study, Master's thesis, Geotechnical Division, Norwegian Institute of Technology, Trondheim, Norway (in Norwegian).

Janbu, Nilmar (1967). Settlement calculations based on tangent modulus concept, Bulletin Nr. 2, Geotechnical Division, Norwegian Institute of Technology, Trondheim, Norway.

Janbu, N. and Senneset, K. (1980). Field compressometer-principles and applications, Bulletin Nr. 8, Geotechnical Division, Norwegian Institute of Technology, Trondheim, Norway.

Kvalsvik, Hans Jonny (1991). Plate load tests in sand, Master's thesis, Geotechnical Division, The Norwegian Institute of Technology, Trondheim, Norway (in Norwegian).

McKinley, D. G. (1961). A laboratory study of rates of consolidation in clays with particular reference to conditions of radial pore water drainage, Proceedings, 5th International Conference on Soil Mechanics, Paris.

Nishida, Y. (1966). Vertical stress and vertical deformation of ground under a deep circular uniform pressure in the semi-infinite, Kanazawa University, Ishikawa-ken, Japan.

Nordal, Steiner (1983). Elasto-plastic behaviour of soils analyzed by the finite element method, Geotechnical Division, The Norwegian Institute of Technology, Trondheim, Norway.

Related papers

Janbu, N; Bjerrum, L. and Kjærnsli, B. (1956). Soil mechanics applied to some engineering problems, Publication Nr. 16, Norwegian Geotechnical Institute, Oslo, Norway (In Norwegian).

Janbu, N. (1967). Soil compressibility as determined by oedometer and triaxial tests, Bulletin Nr. 1, Geotechnical Division, Norwegian Institute of Technology, Trondheim, Norway.

Janbu, N. (1967). Consolidation of clay layers based on non-linear stress-strain, Bulletin Nr. 1, Geotechnical Division, Norwegian Institute of Technology, Trondheim, Norway.

Janbu, N. (1980). In situ measurement of soil properties - Discussions at ASCE specialty conference, Geotechnical Division, Norwegian Institute of Technology, Trondheim, Norway.

Janbu, N. (1980). Principles and analysis methods for the in situ measurement of soil parameters, Geotechnical Division, Norwegian Institute of Technology, Trondheim, Norway (in Norwegian).

Hauan, R. (1967). Experimental analysis of the methods for the measuring of in situ compressibility of cohesionless soils, Master's thesis, Geotechnical Division, Norwegian Institute of Technology, Trondheim, Norway (in Norwegian).

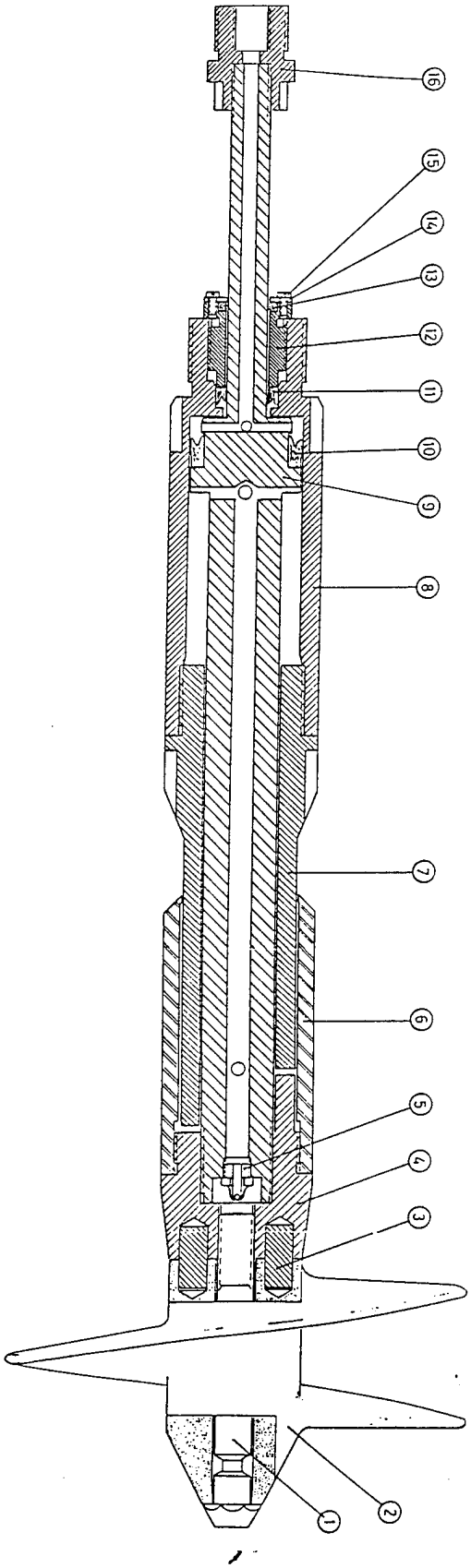

Figure 1 Field compressometer

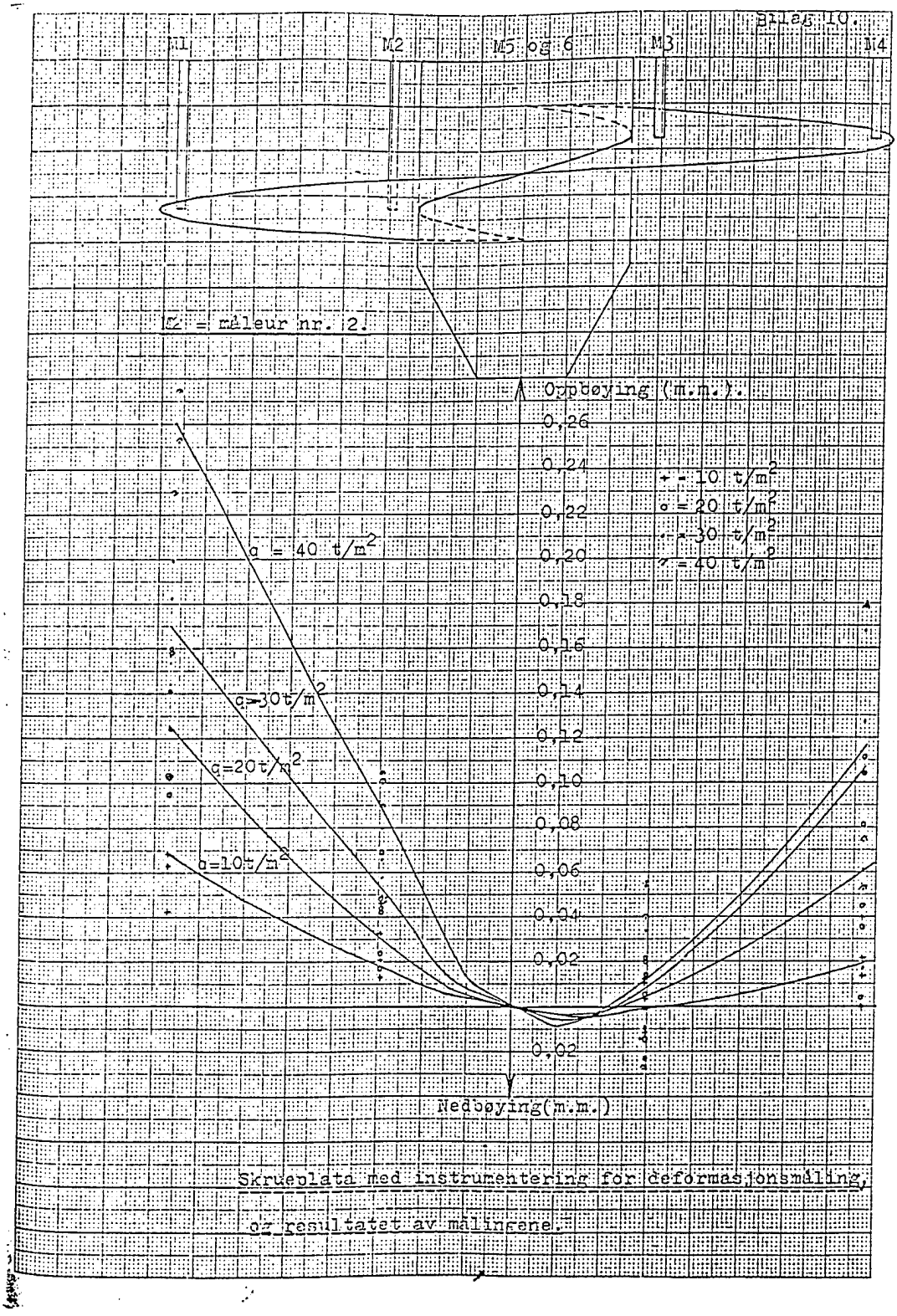

Figure 2 Deformation of field compressometer blade

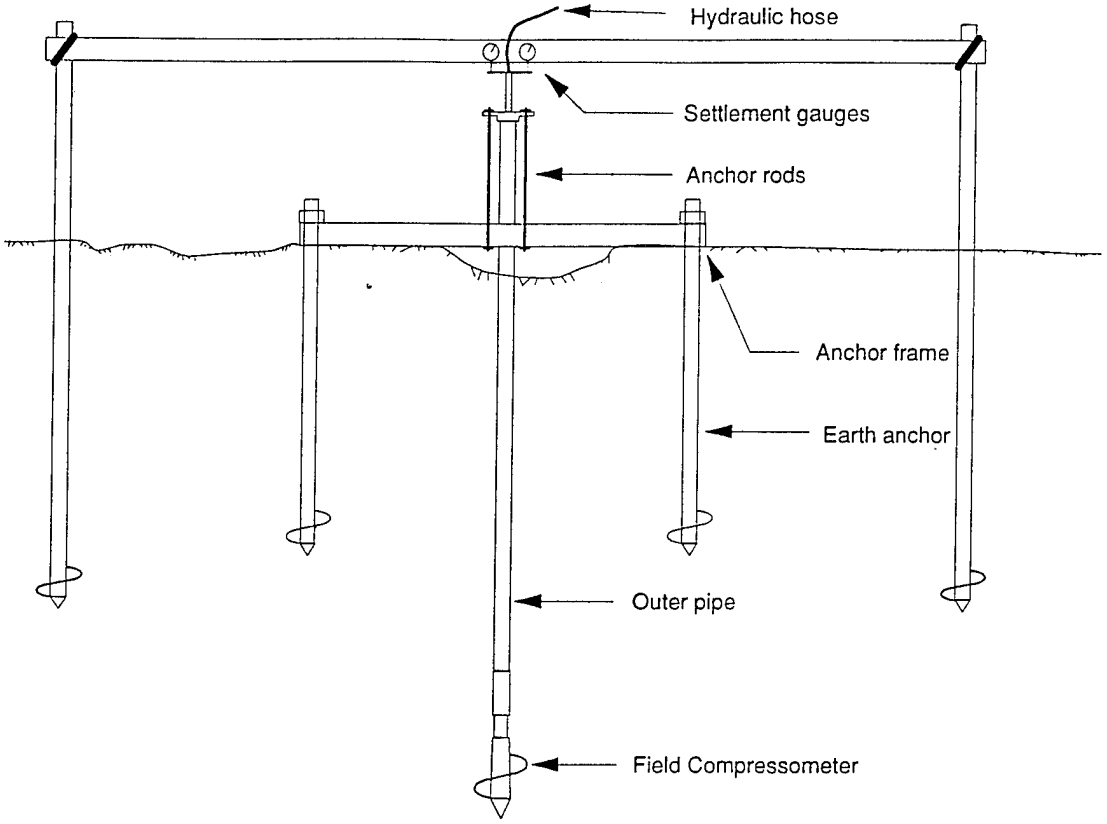

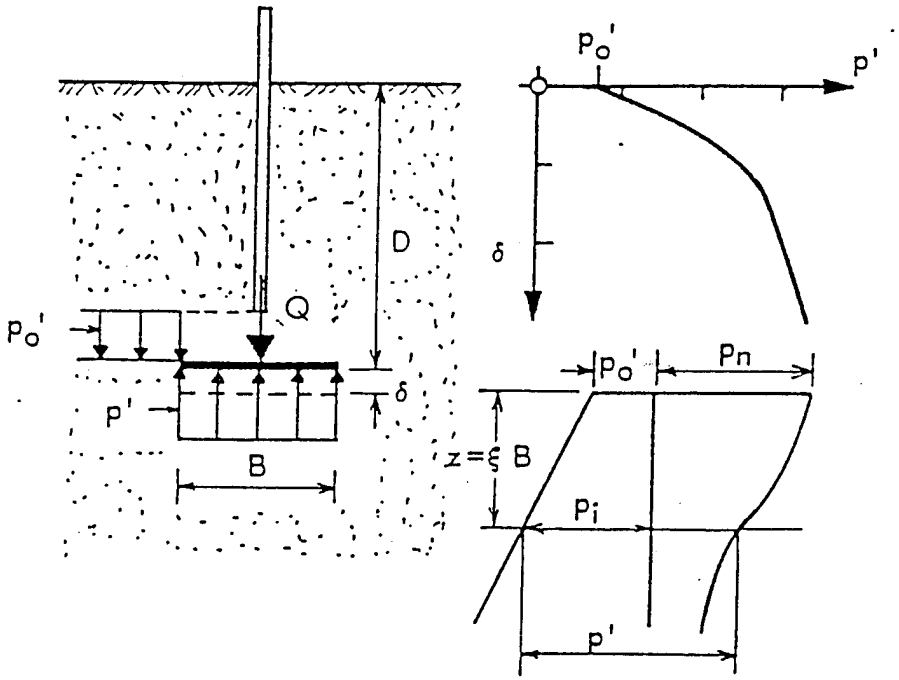

Figure 3 In situ installation and idealized loading condition for a buried plate

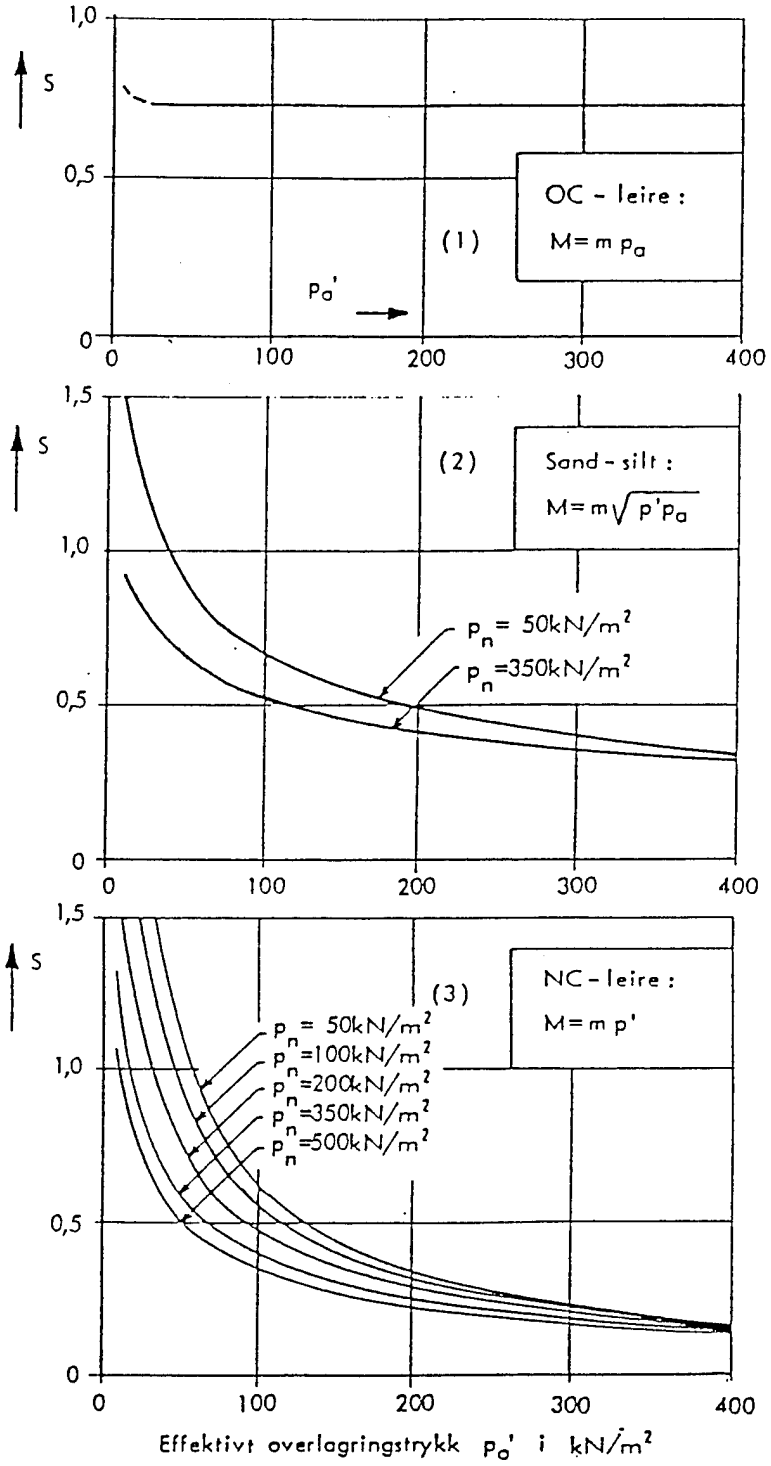

Figure 4 Settlement number S as a function of effective overburden and incremental stress for various soil types (Janbu and Senneset, 1973)

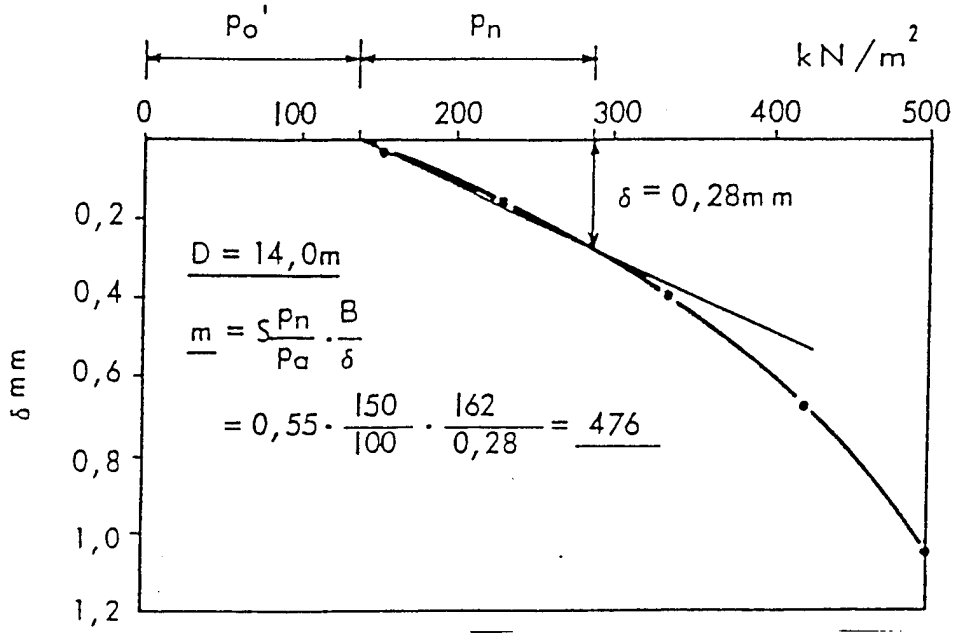

Figure 5 Example calculation of the modulus number m (Janbu and Senneset, 1973)

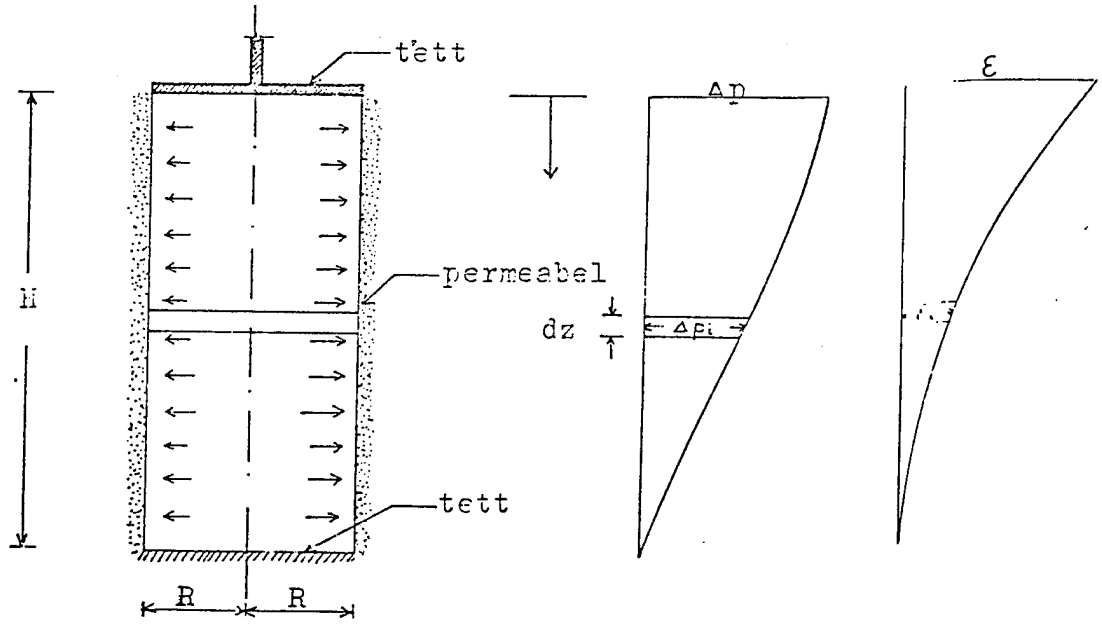

Figure 6 Radially draining oedometric model (Enlid, 1970)

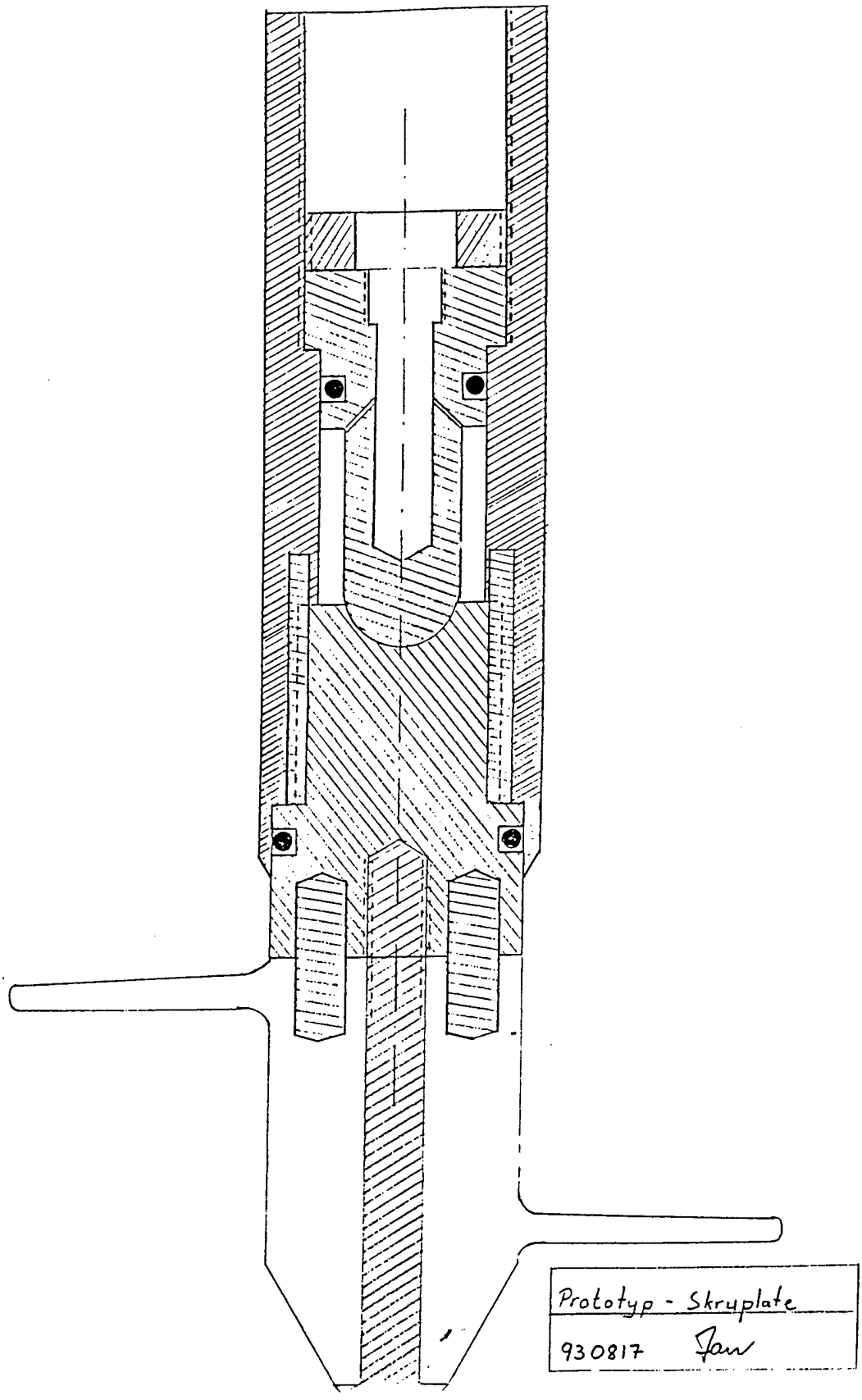

Figure 7 Prototype field compressometer

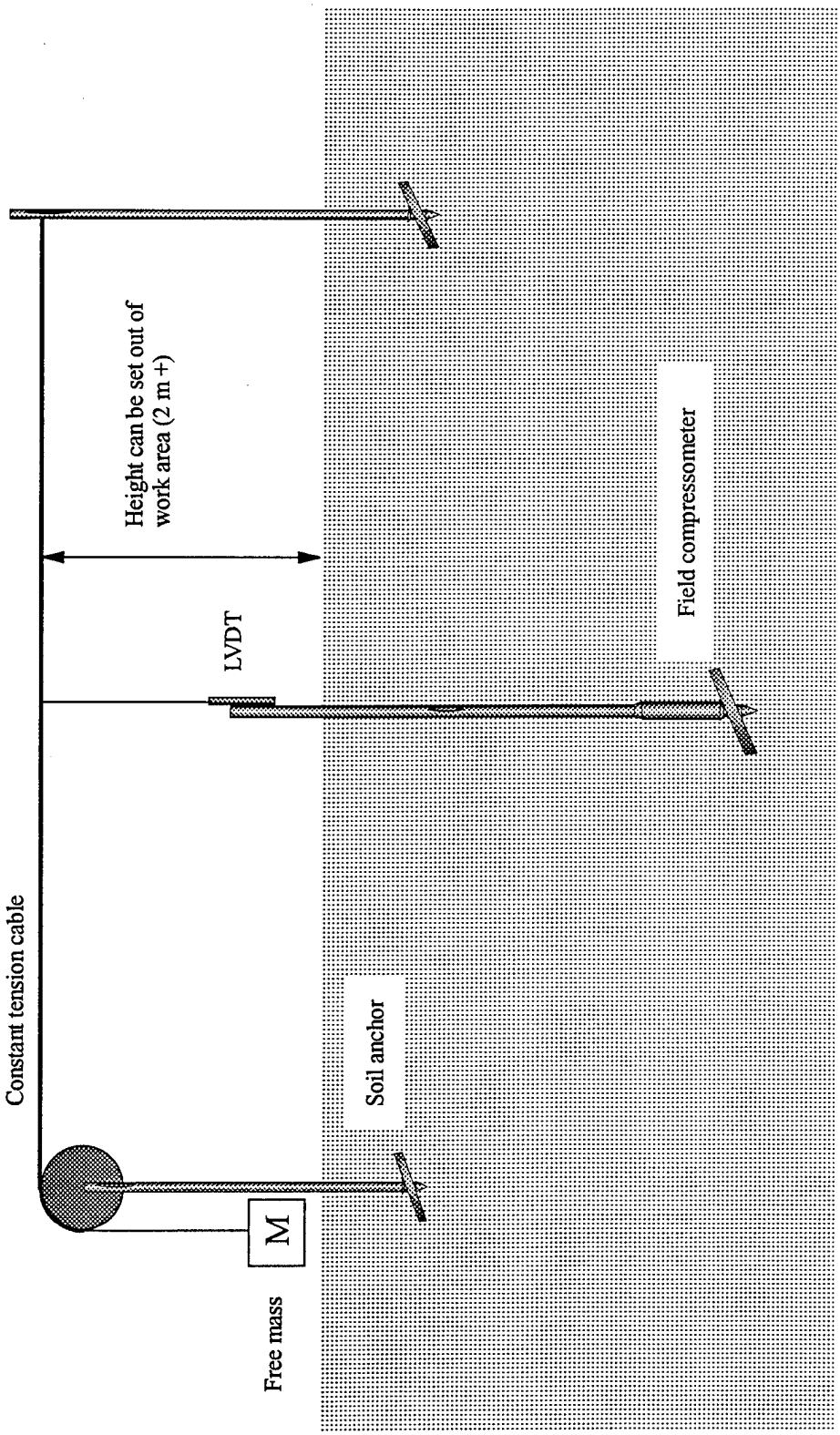

Figure 8 In situ configuration of the prototype field compressometer

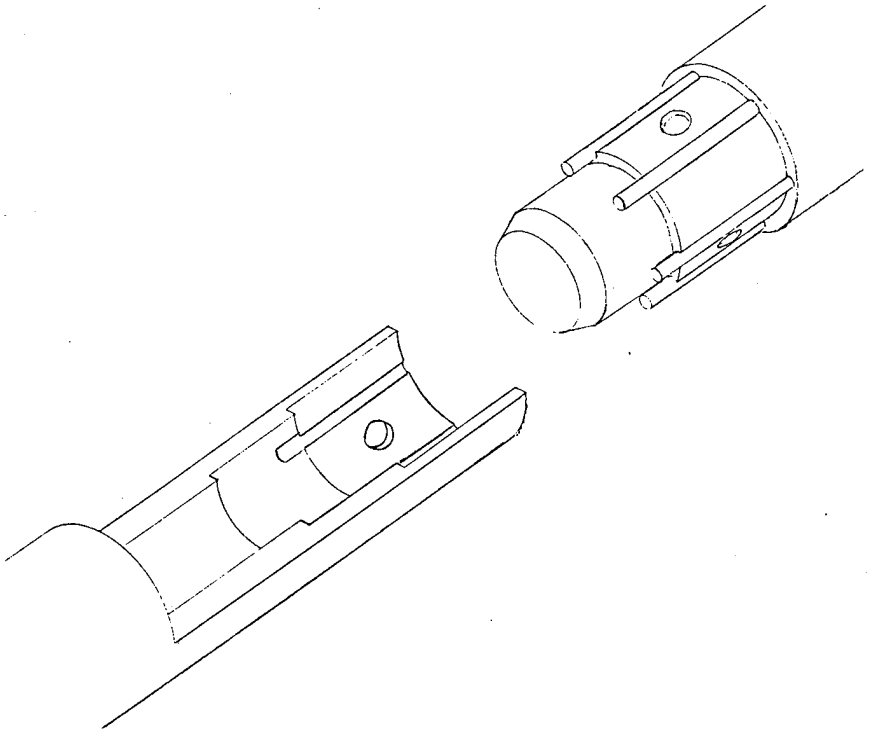

Figure 9 Detail of the drill rod connections

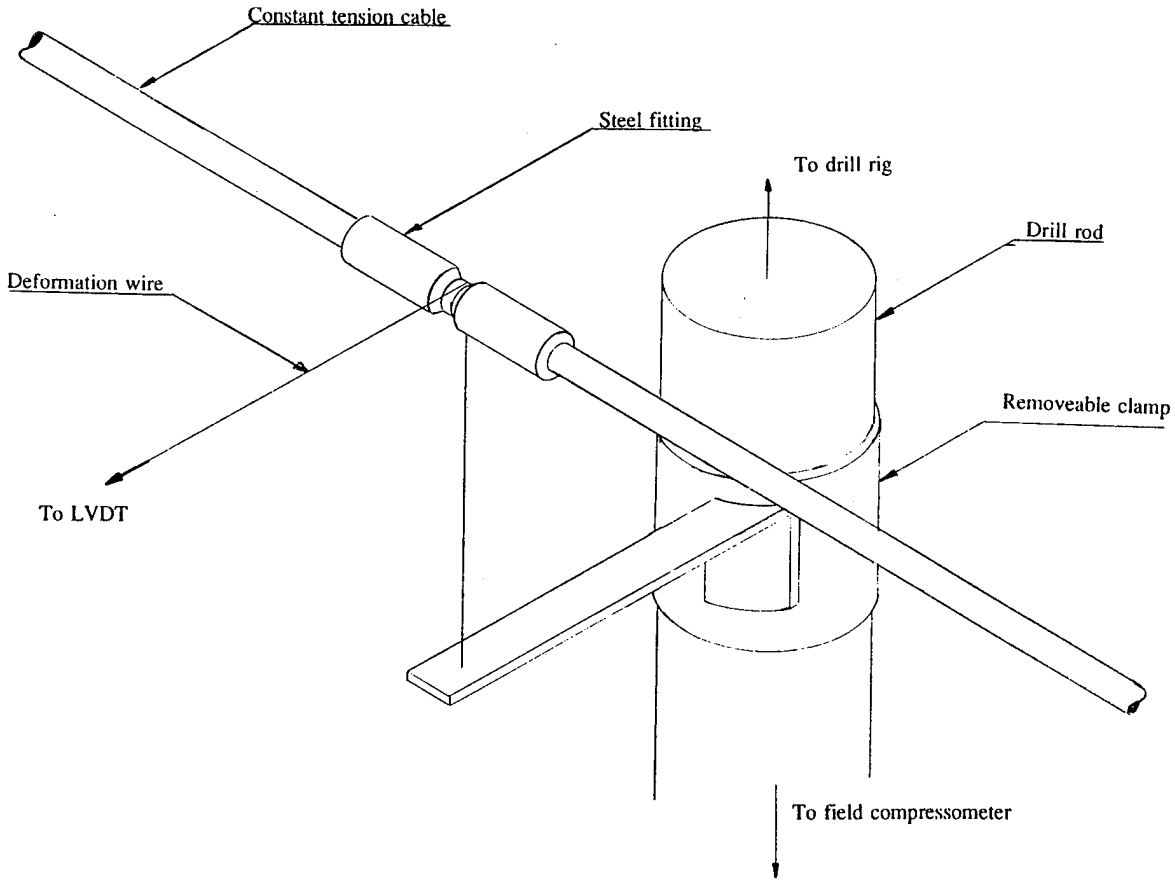

Figure 10 Detail of the deformation measurement system

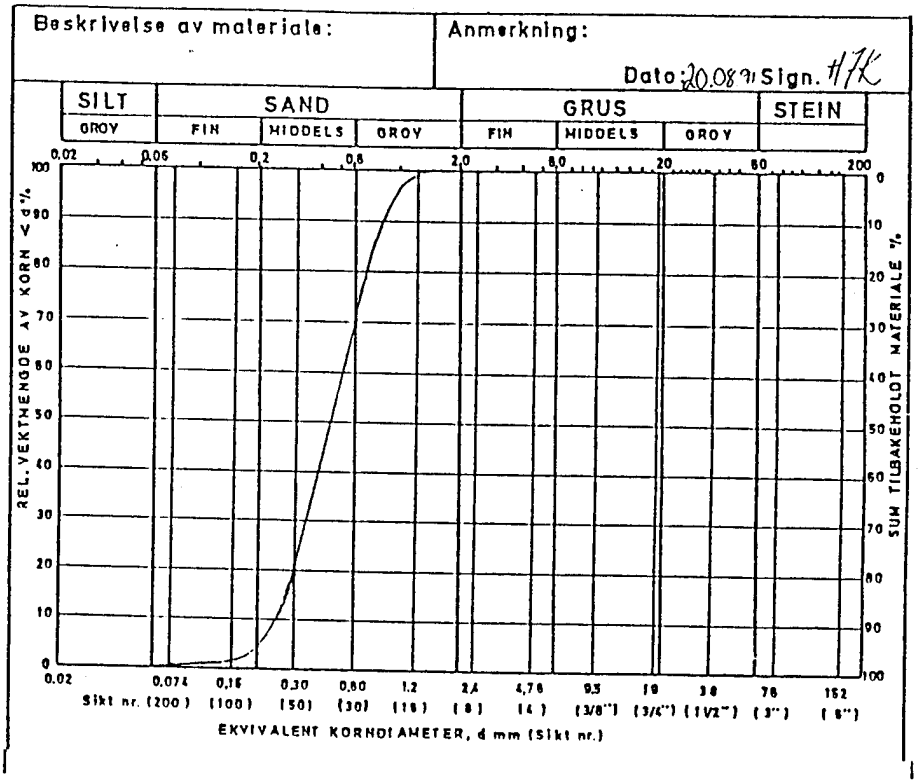

Figure 11 Grain size distribution, Hokksund sand

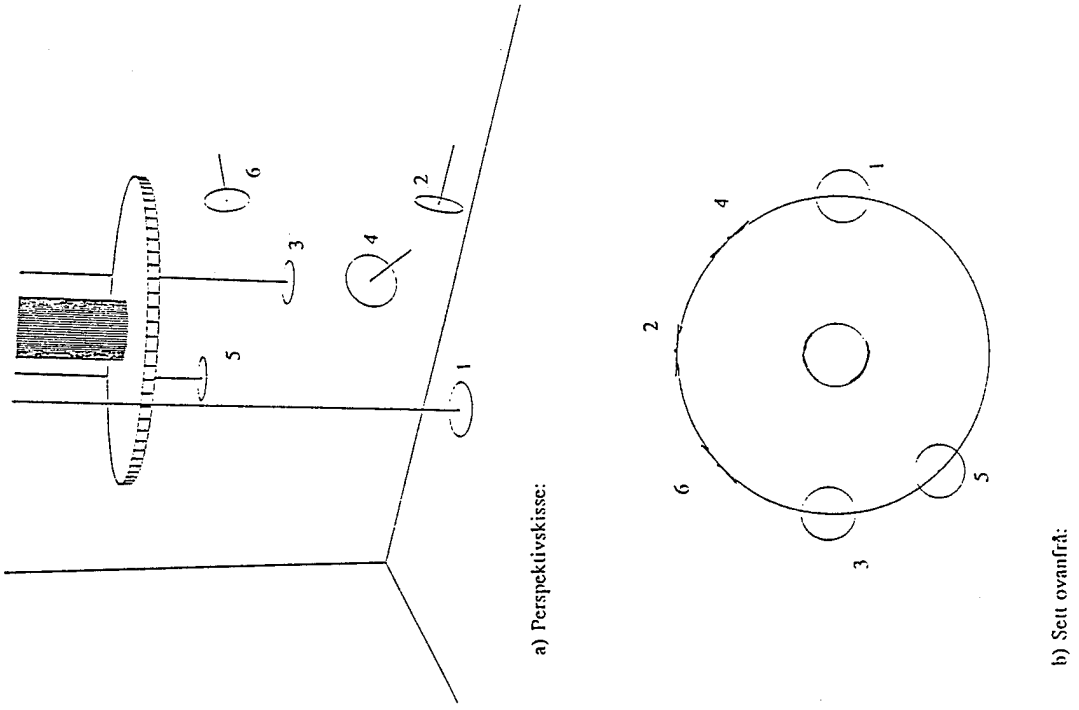

Figure 12 Placement of deformation plates (Kvalsvik, 1991)

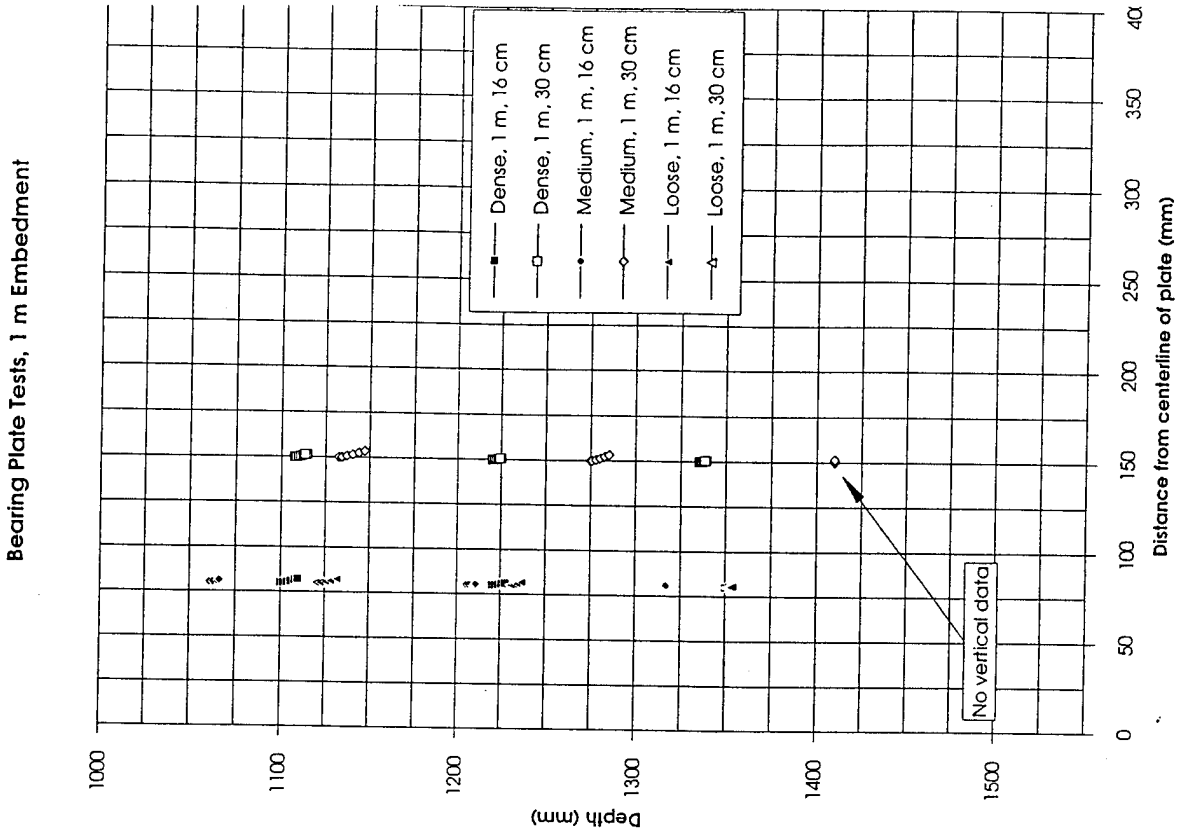

Figure 13 Deformation patterns, shallow embedment - true scale

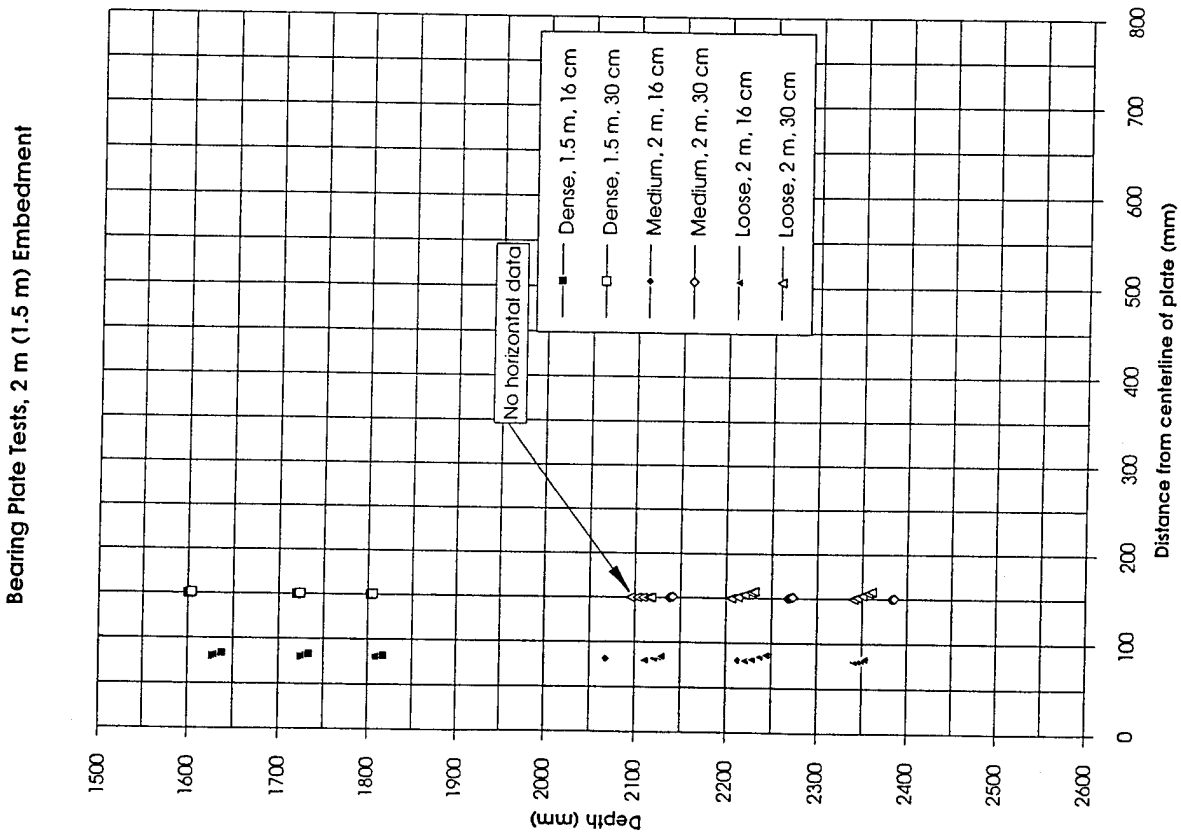

Figure 14 Deformation patterns, deep embedment - true scale

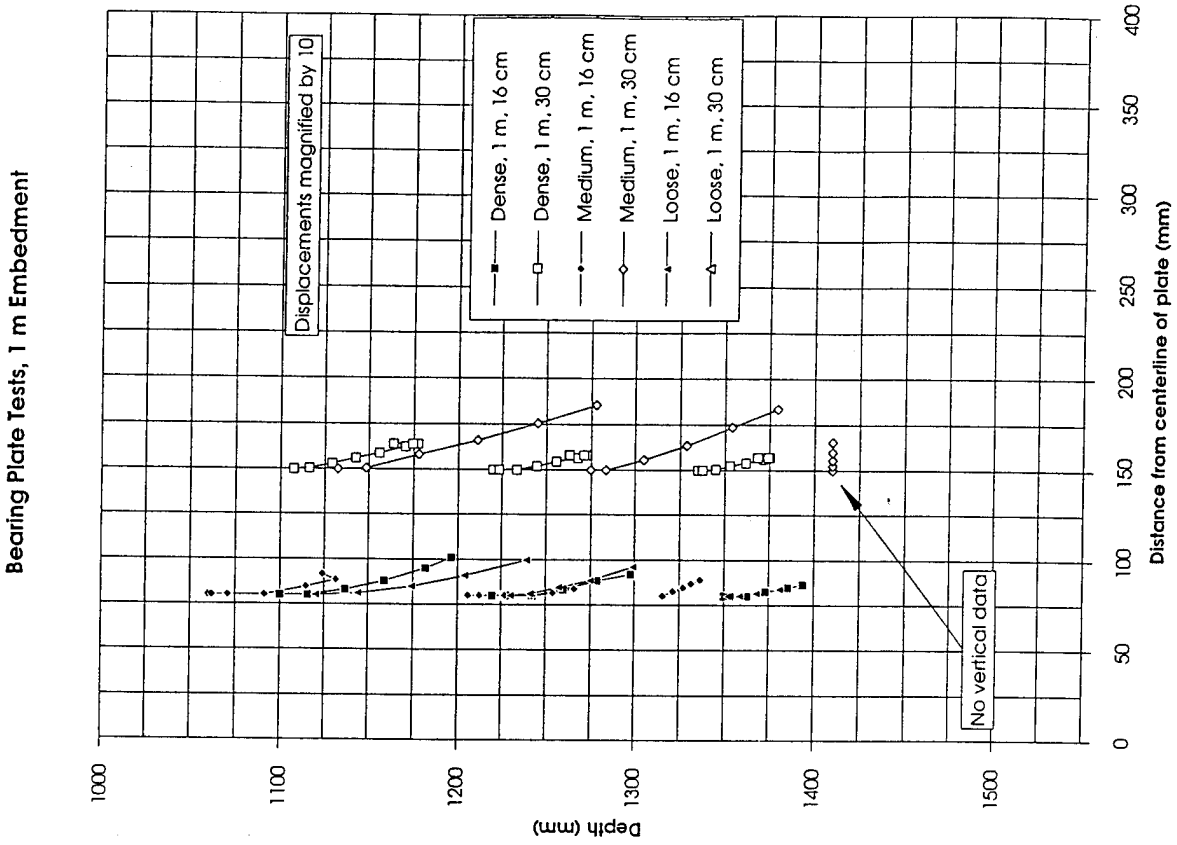

Figure 15 Deformation patterns, shallow embedment - exagerated scale

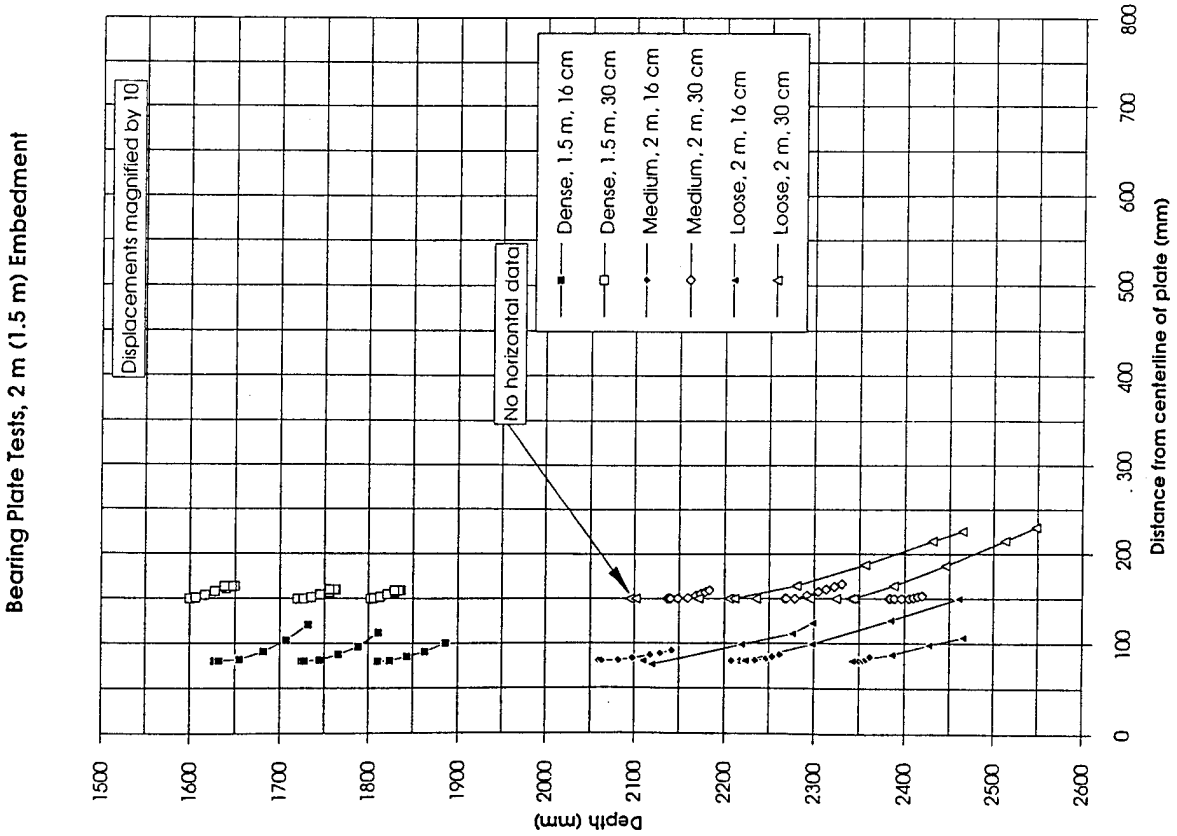

Figure 16 Deformation patterns, deep embedment - exaggerated scale

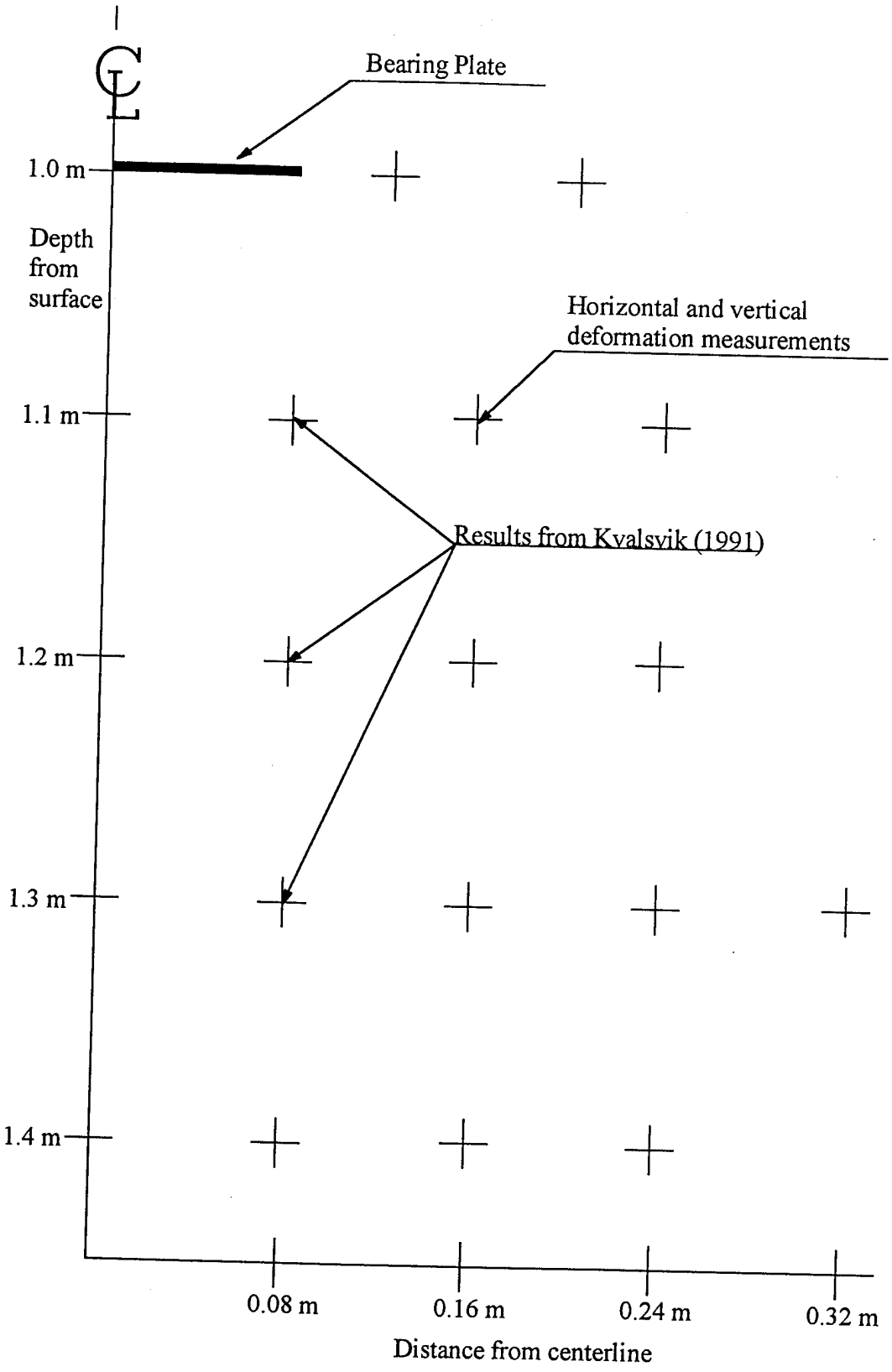

Figure 17 Deformation measurement locations (Hoff, 1991)

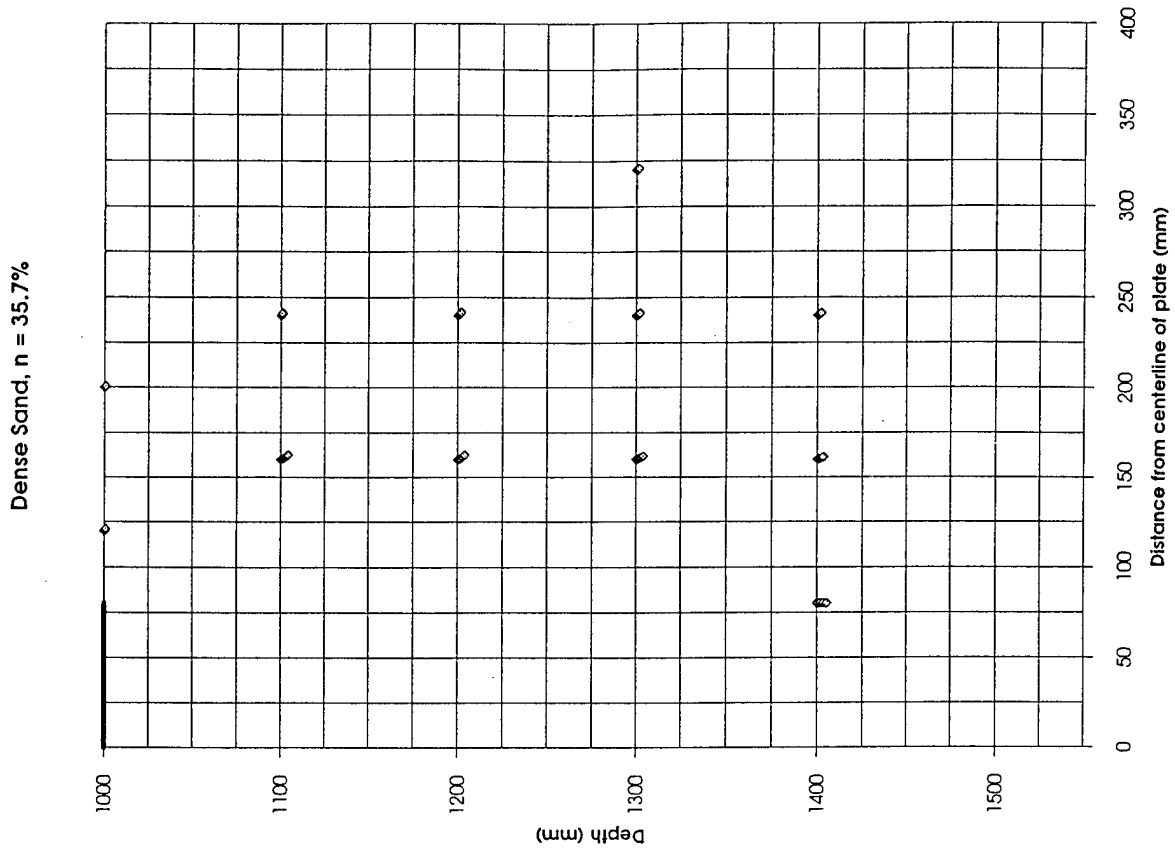

Figure 18 Deformation patterns, dense sand

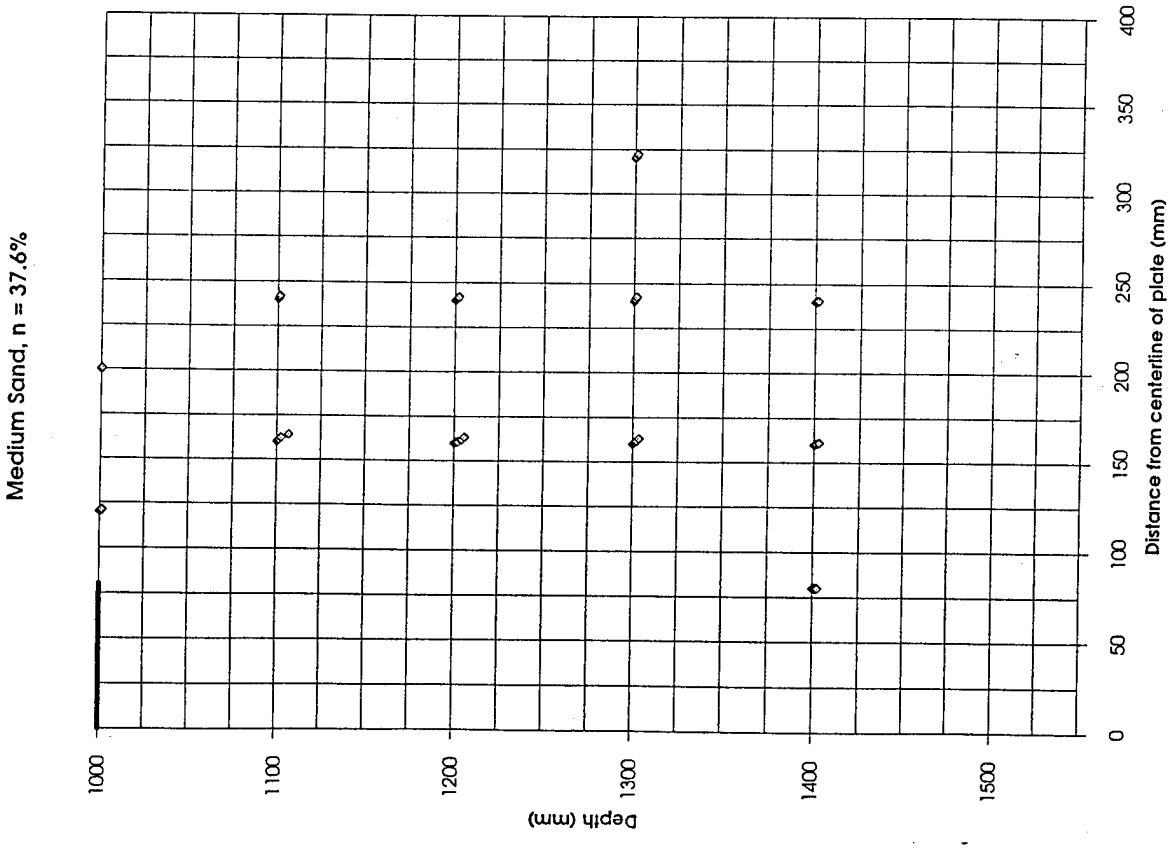

Figure 19 Deformation patterns, medium sand

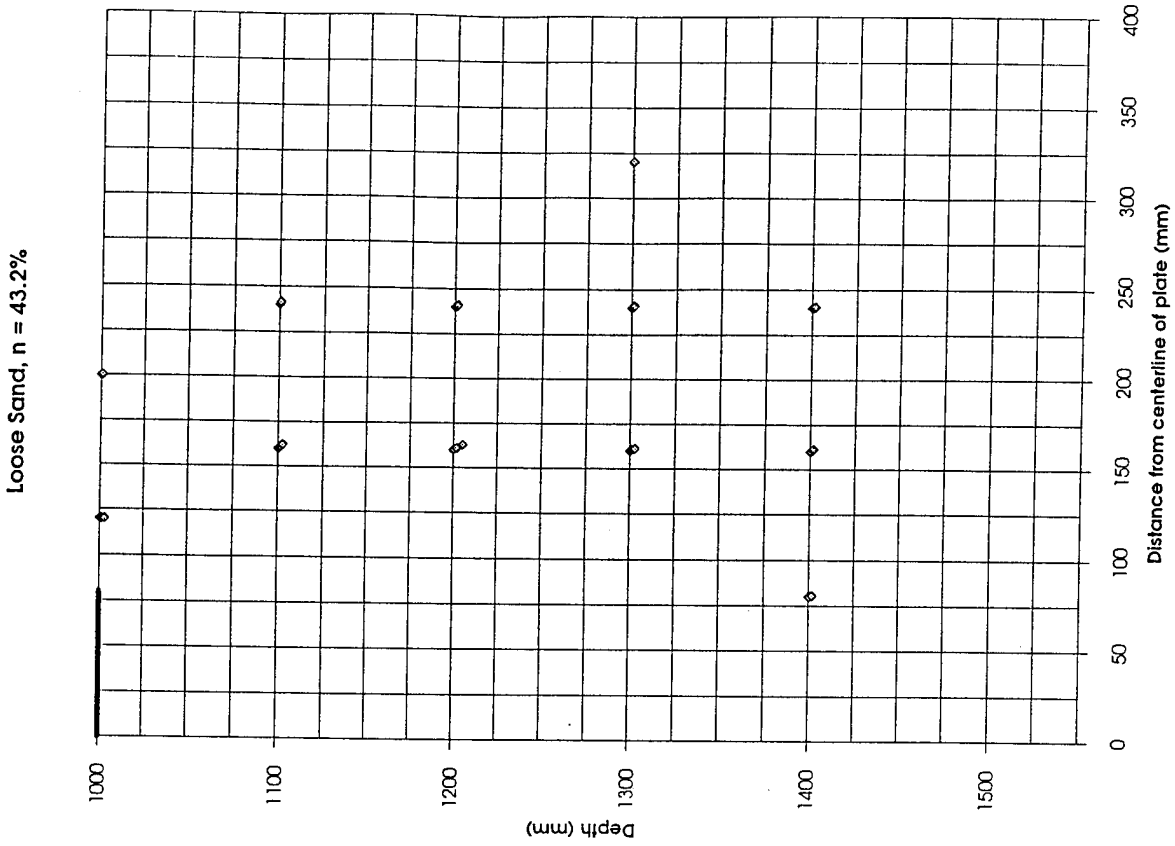

Figure 20 Deformation patterns, loose sand

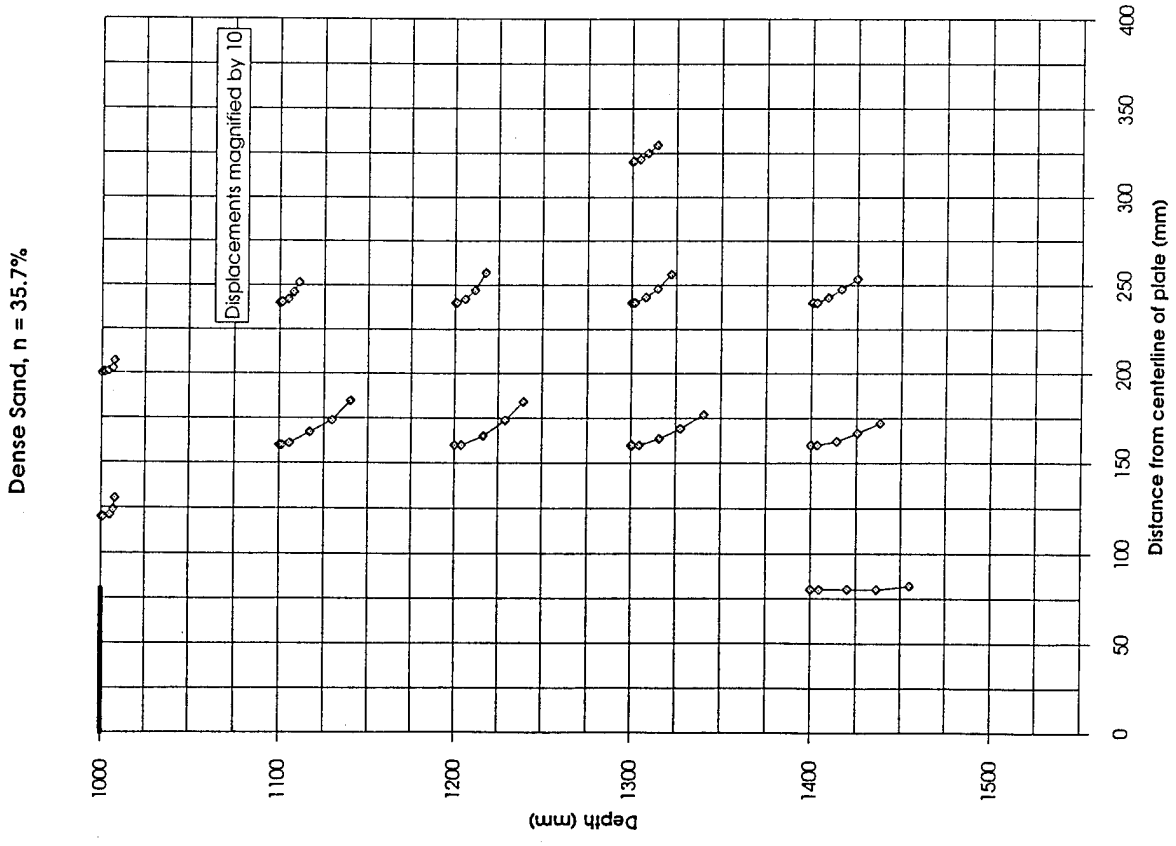

Figure 21 Deformation patterns, dense sand -exaggerated scale

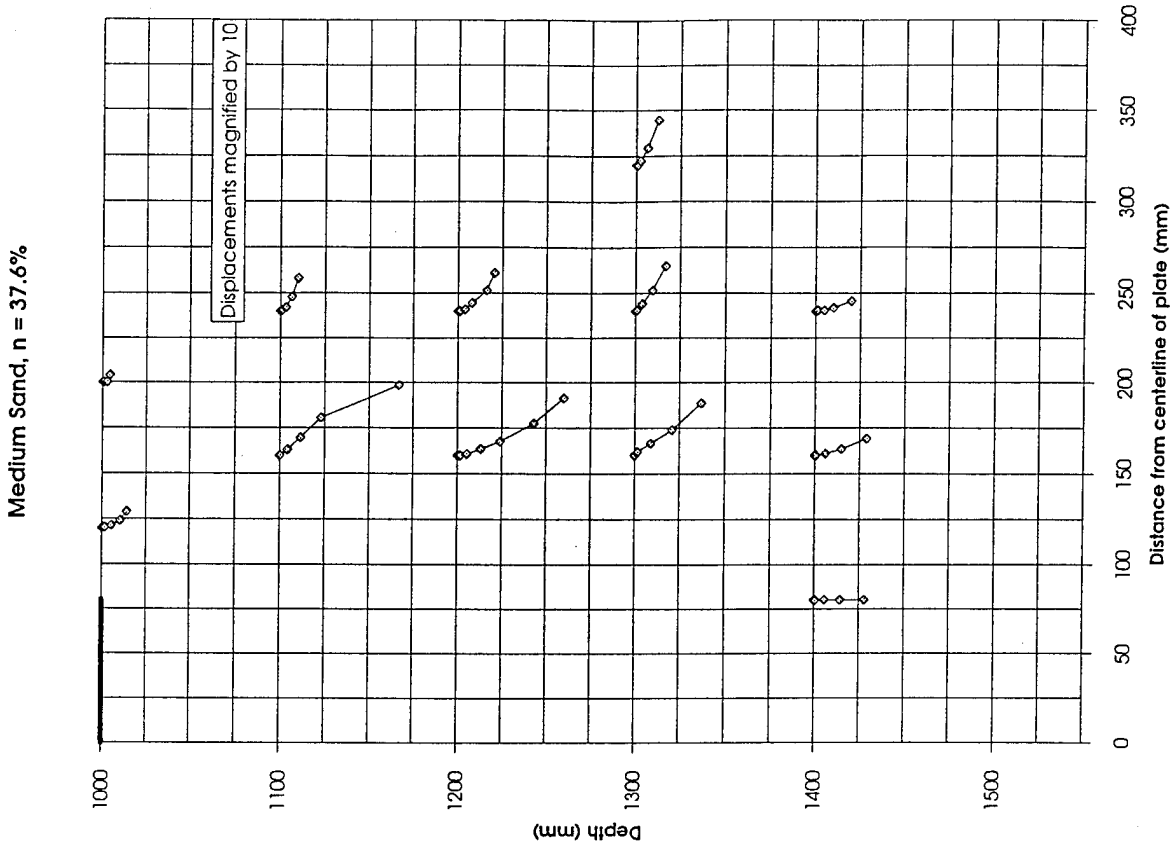

Figure 22 Deformation patterns, medium sand - exaggerated scale

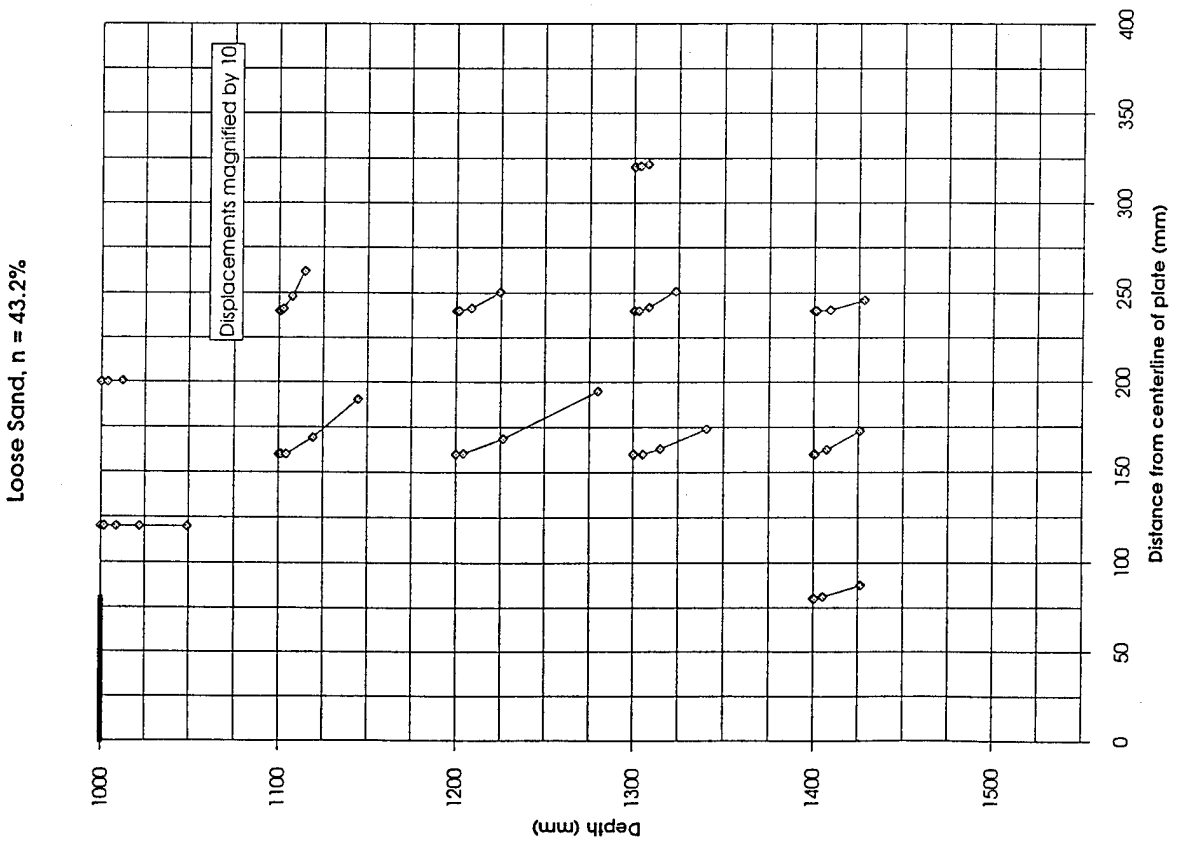

Figure 23 Deformation patterns, loose sand - exaggerated scale

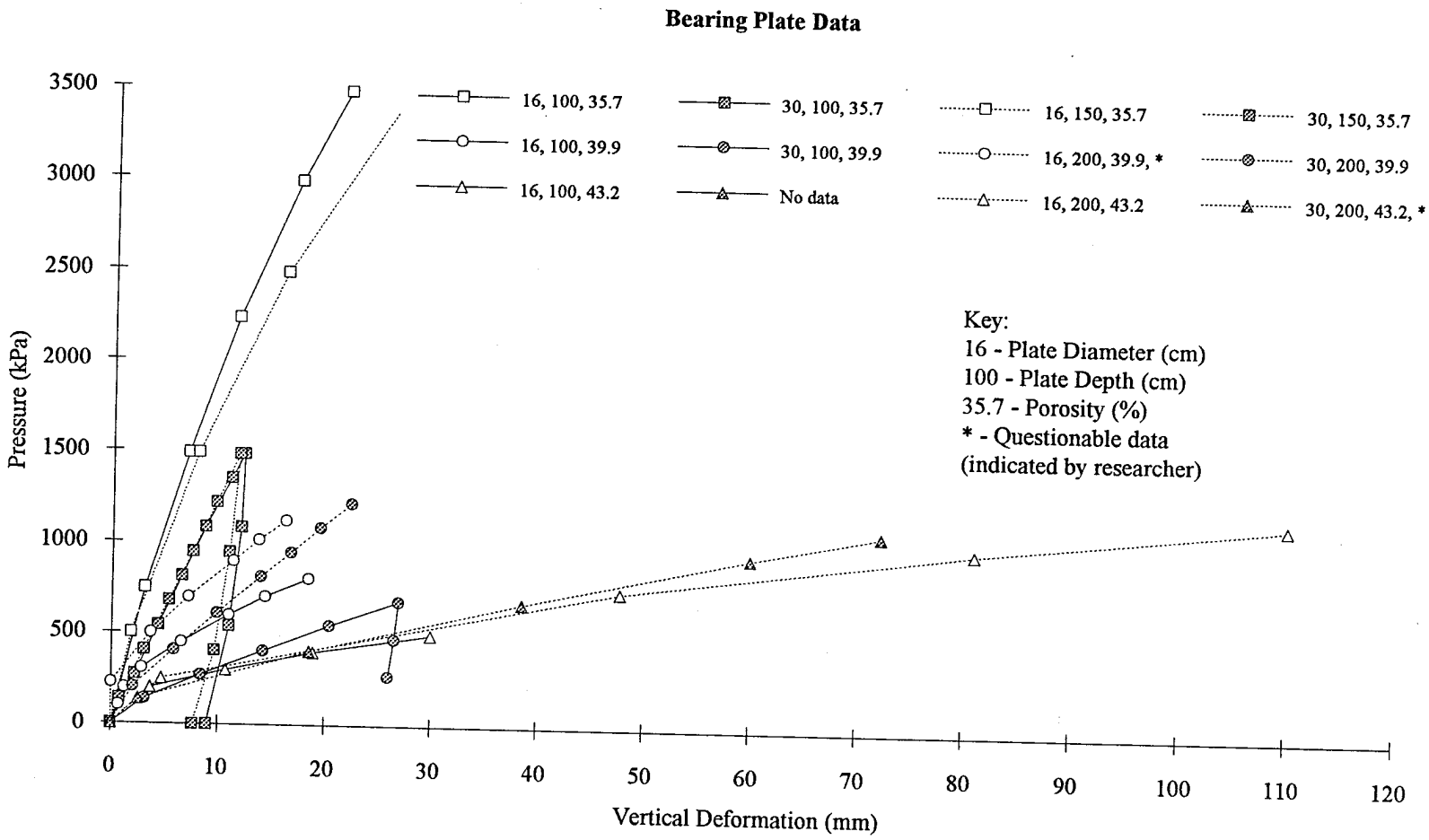

Figure 24 Load-deformation curves (after Kvalsvik, 1991)

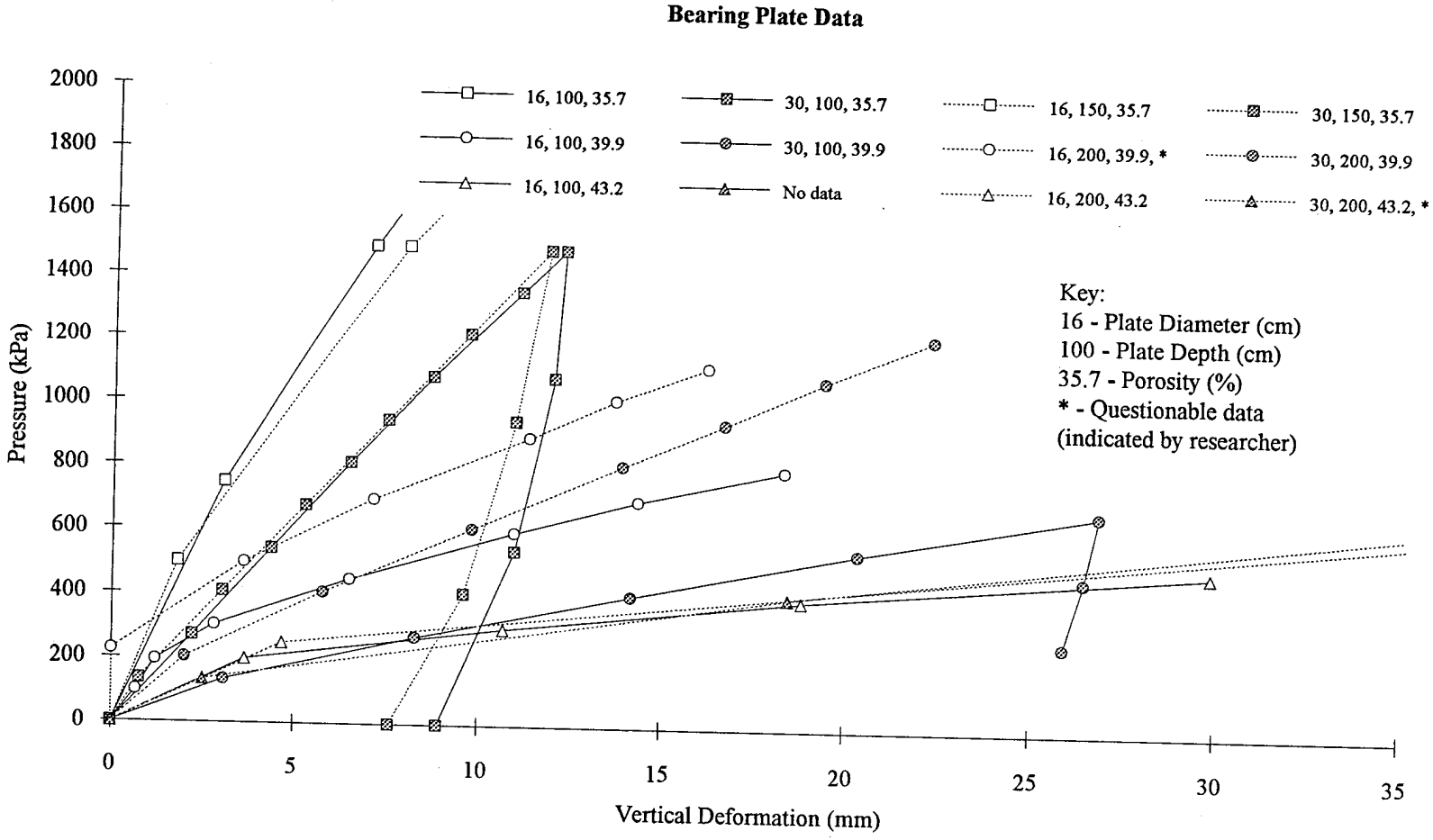

Figure 25 Detail of Figure 24

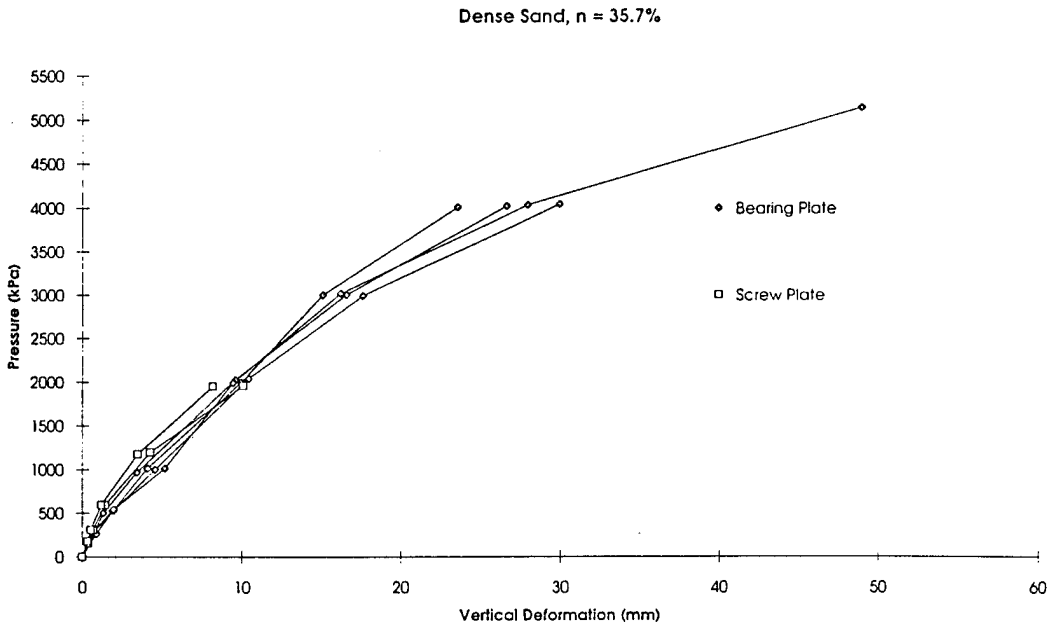

Figure 26 Load-deformation curves, dense soil (after Hoff, 1993)

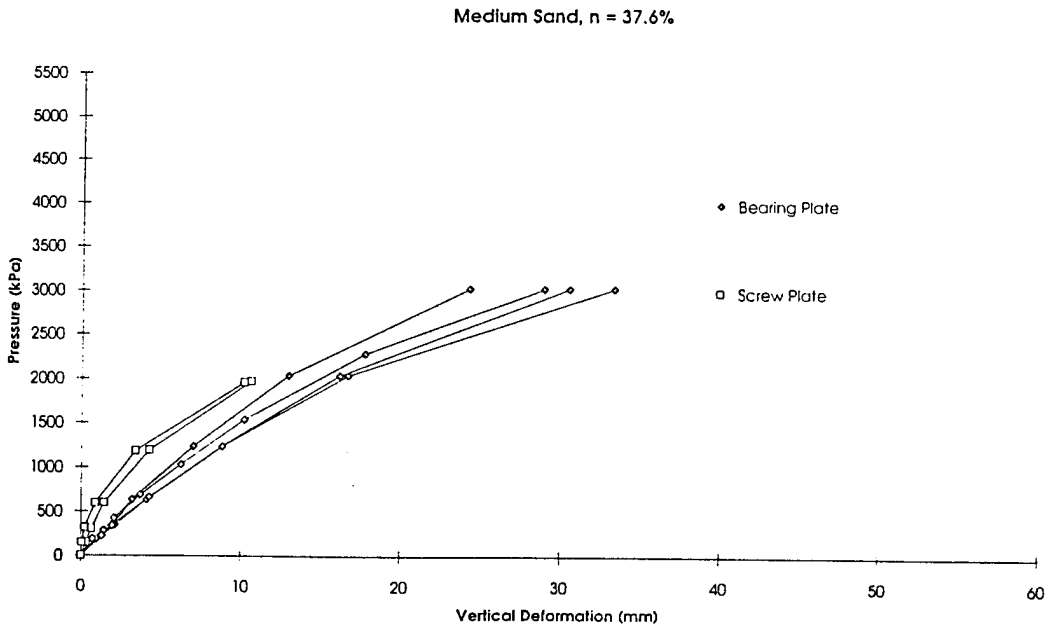

Figure 27 Load-deformation curves, medium soil (after Hoff, 1993)

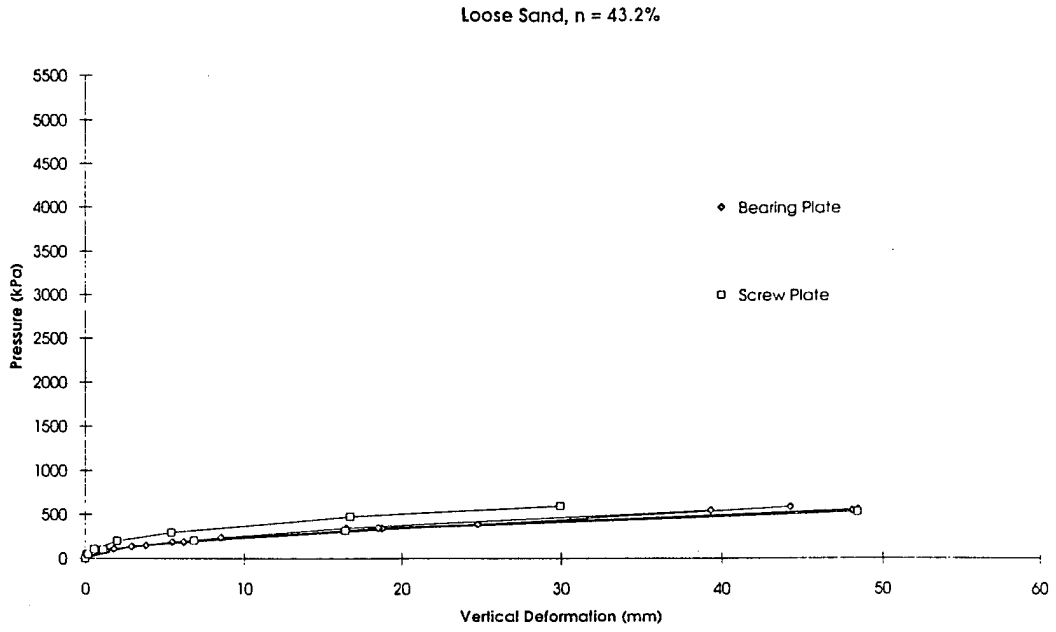

Figure 28 Load-deformation curves, loose soil (after Hoff, 1993)

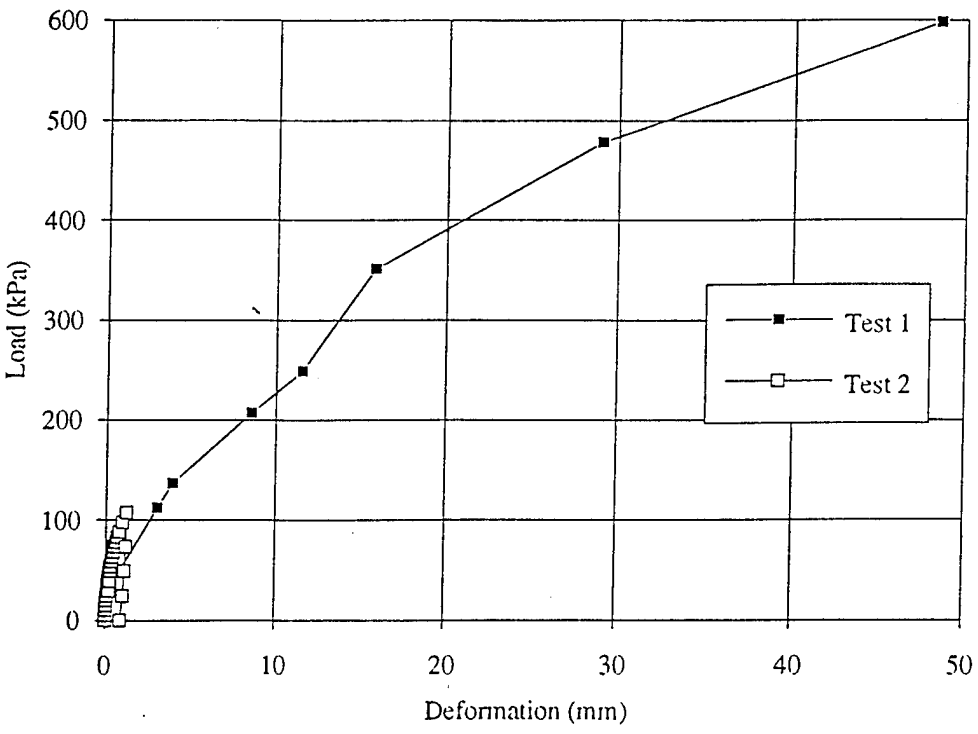

Figure 29 Bearing plate results, loose sand

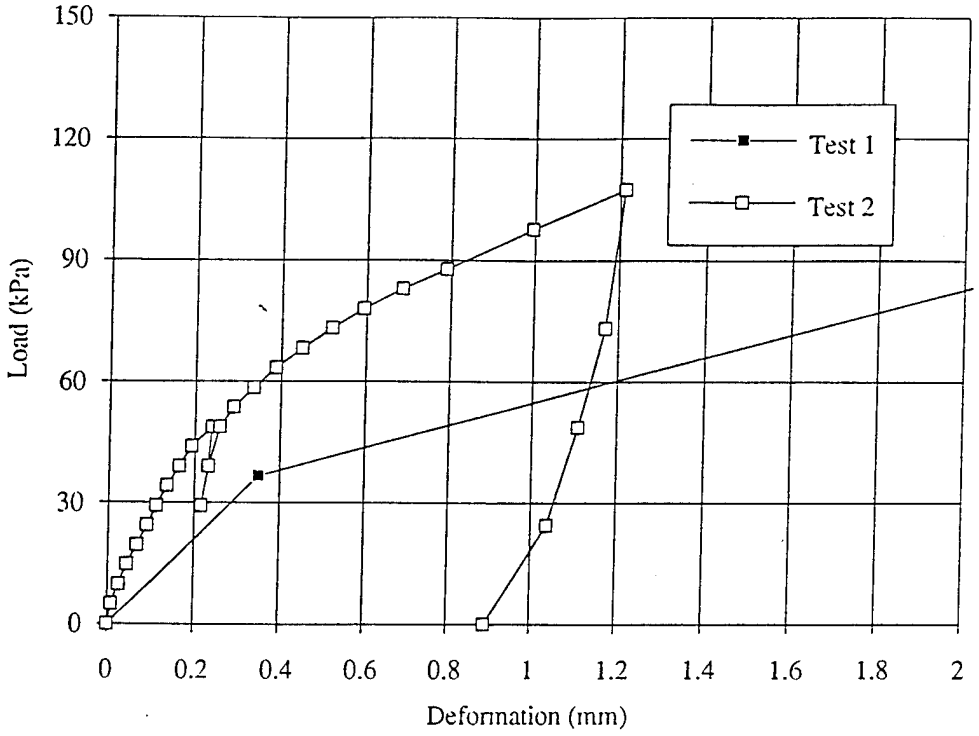

Figure 30 Detail of bearing plate data, loose sand

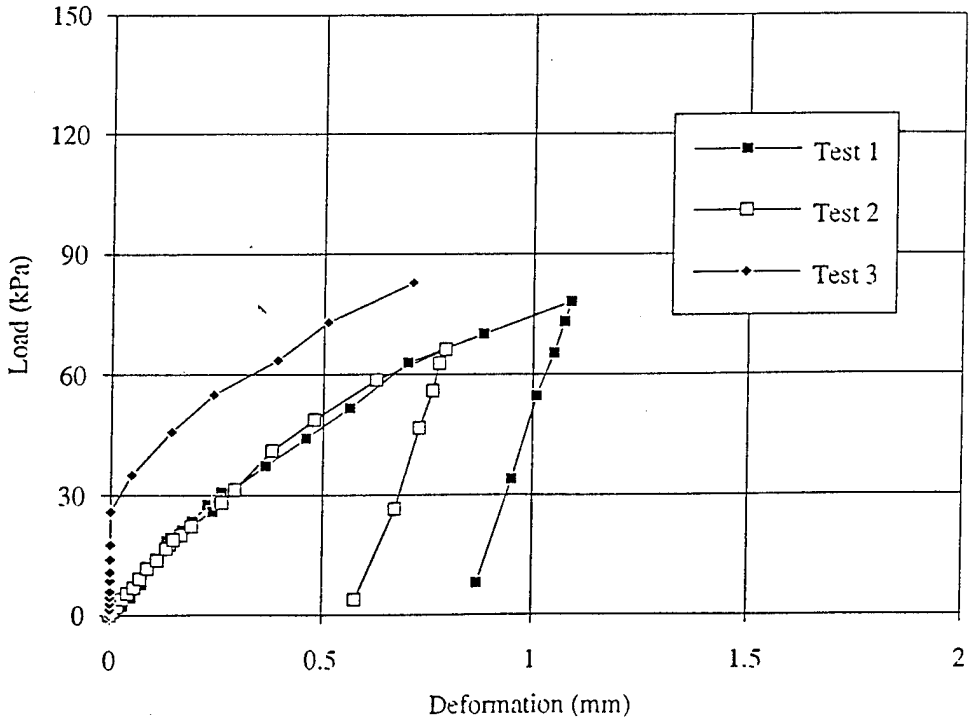

Figure 31 Field compressometer results, loose sand

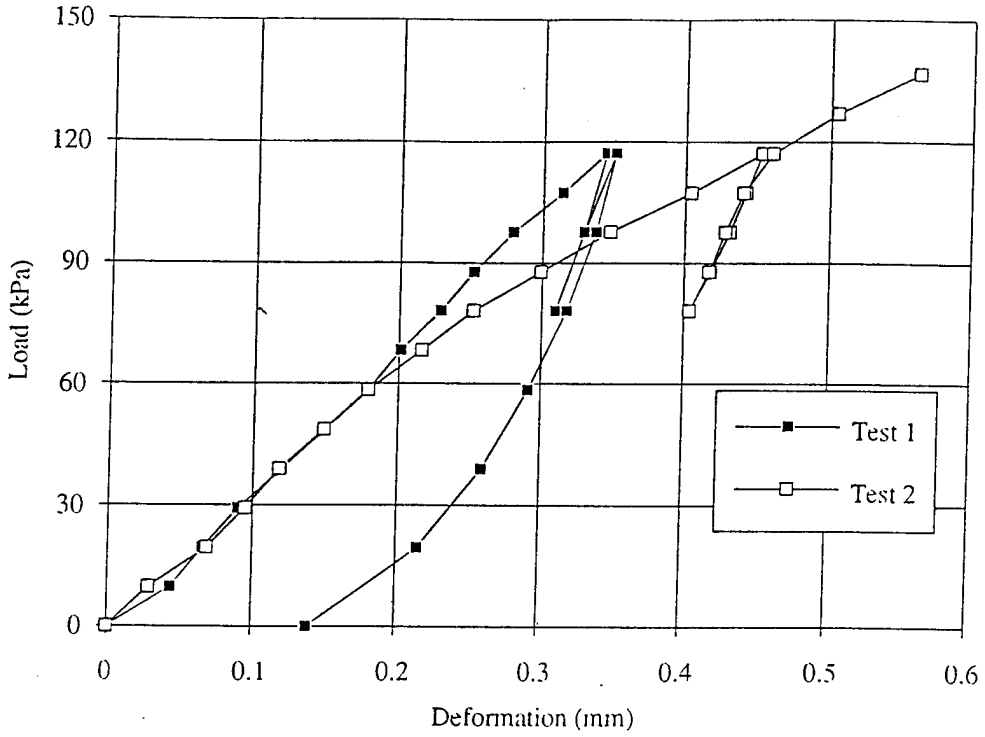

Figure 32 Bearing plate results, medium sand

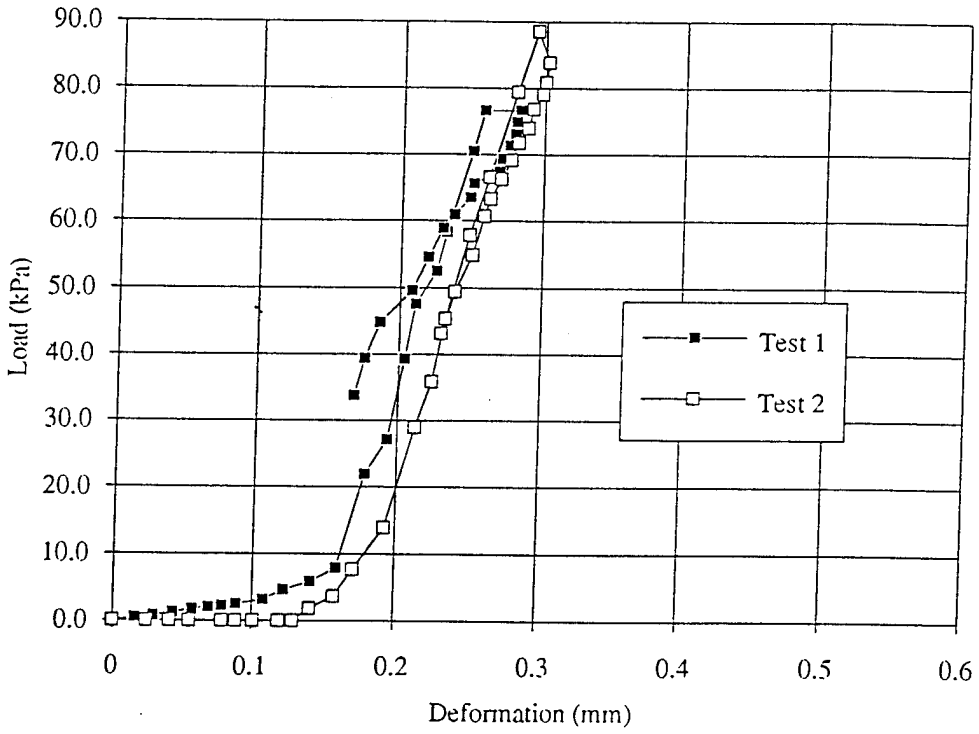

Figure 33 Field compressometer data, medium sand

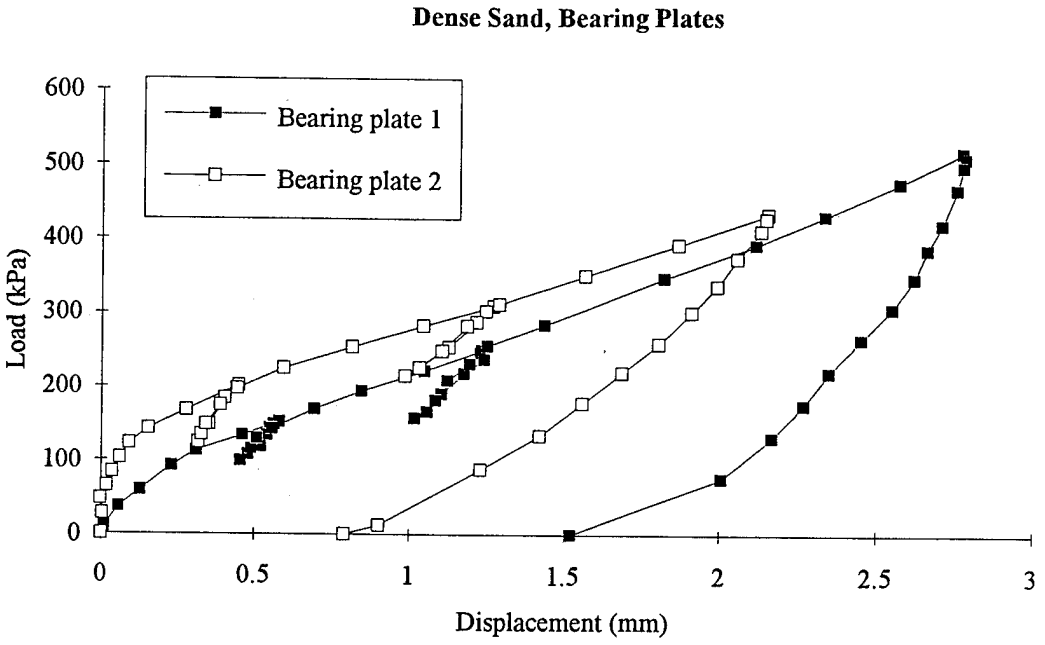

Figure 34 Bearing plate results, dense sand

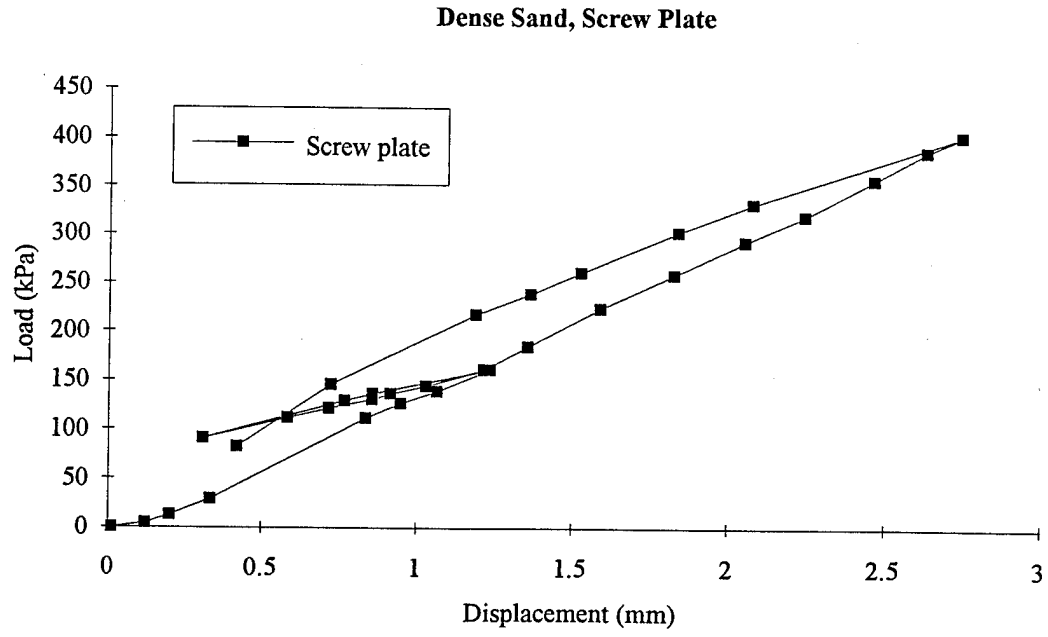

Figure 35 Screw plate response, dense sand

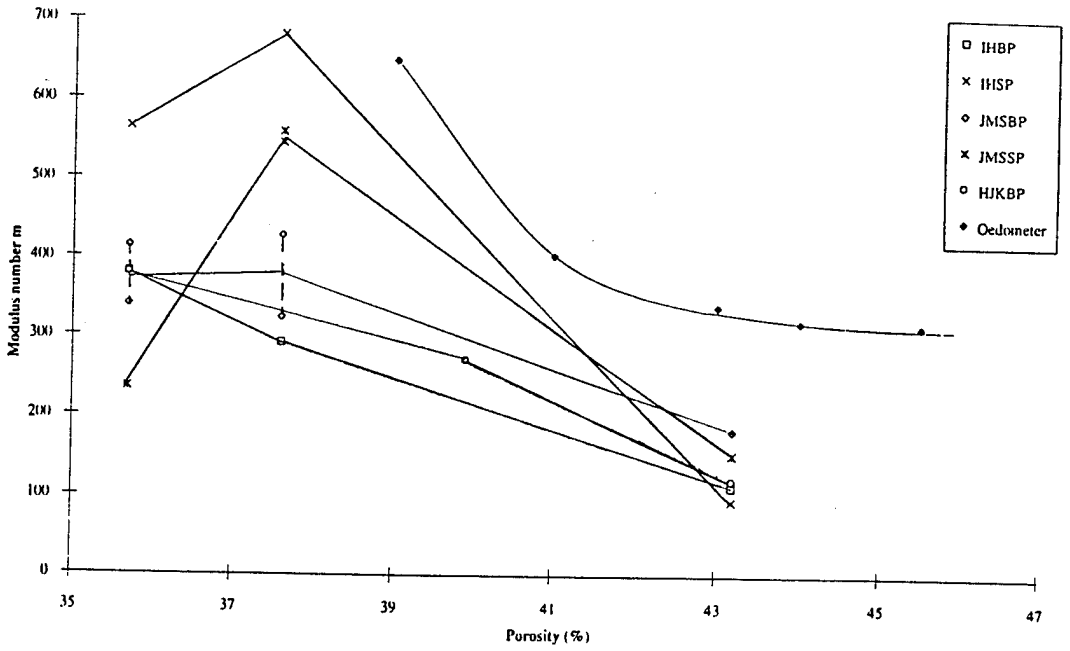

Figure 36 Modulus number estimates

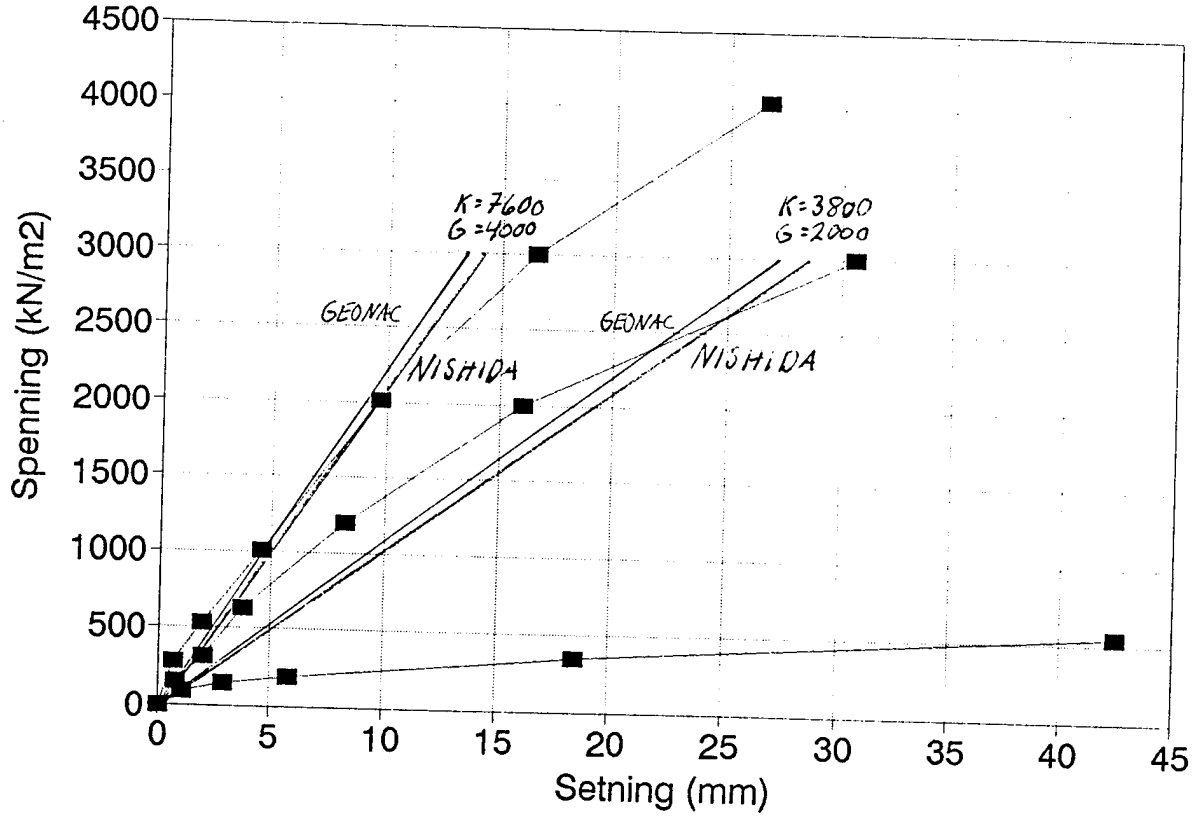

Figure 37 Elastically calculated displacements and measured displacements (Hoff, 1993)

Figure 38a Elasto-Plastic response, Coulomb criteria, $\gamma > 0$ (Nordal, 1983)

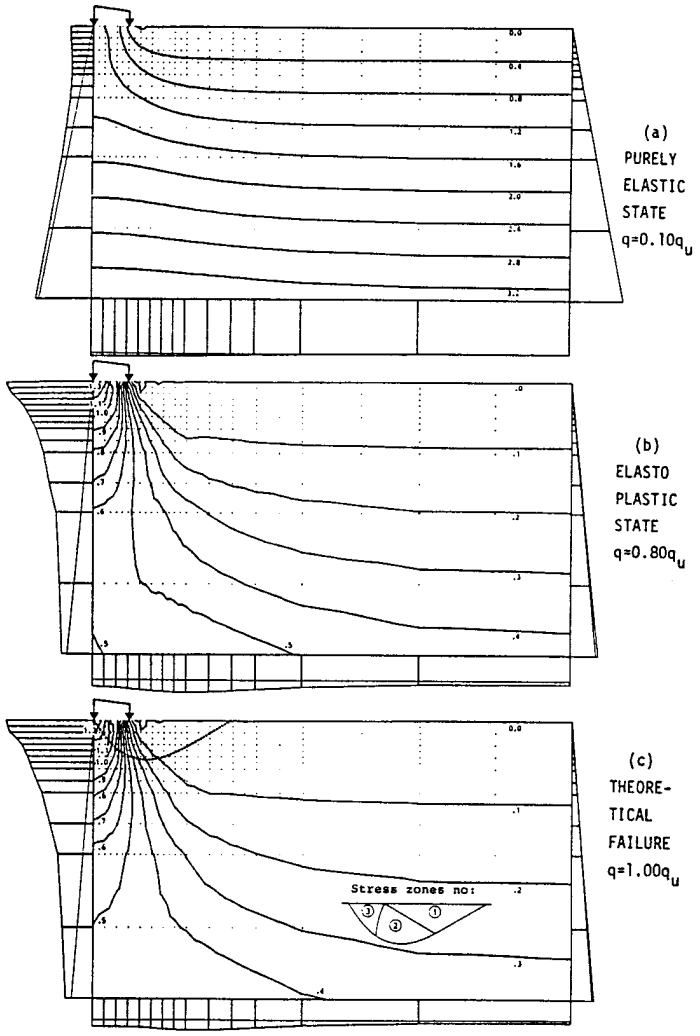

Vertical stresses (σ_z/q) as computed by PLASOL. (a-ϕ, $\gamma \neq 0$, Fig.6.23)

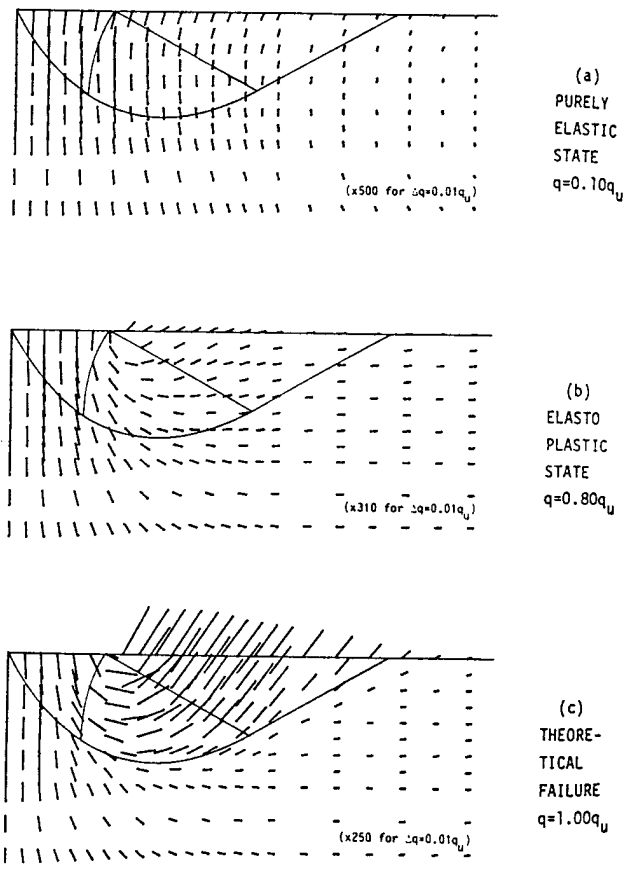

Velocity fields as computed by PLASOL. The upper left corner of the element mesh is shown. The slip-line field is indicated as a reference. (a-ϕ, $\gamma \neq 0$, Fig.6.23)

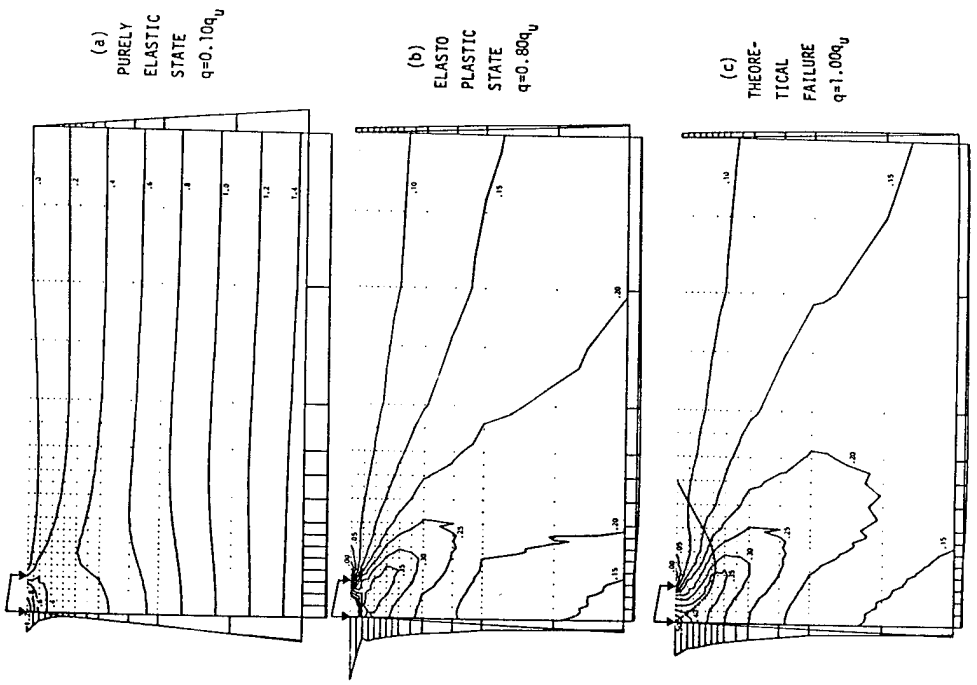

Fig.6.28 Horizontal stresses (σ_x/q) as computed by PLASOL. (a-ϕ, $\gamma \neq 0$, Fig.6.23)

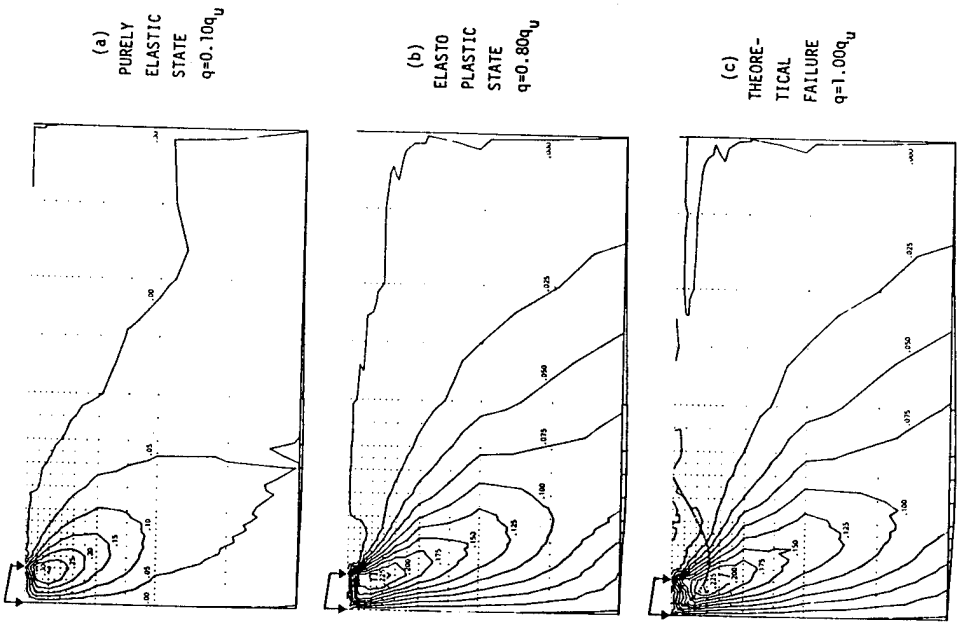

Fig.6.29 Shear stresses on horizontal and vertical planes (τ_{zx}/q) as computed by PLASOL. (a-ϕ, $\gamma \neq 0$, Fig.6.23)

Figure 38b Elasto-Plastic response, Coulomb criteria, $\gamma > 0$ (Nordal, 1983)

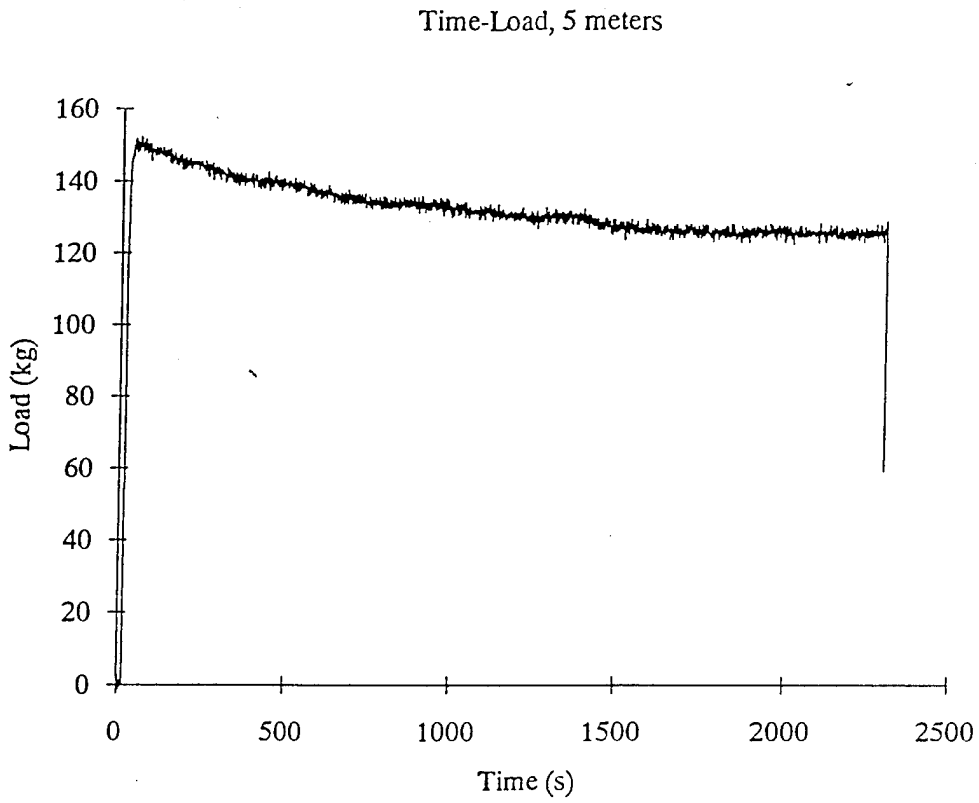

Figure 39 Time history of applied load, 5 m depth, first load increment

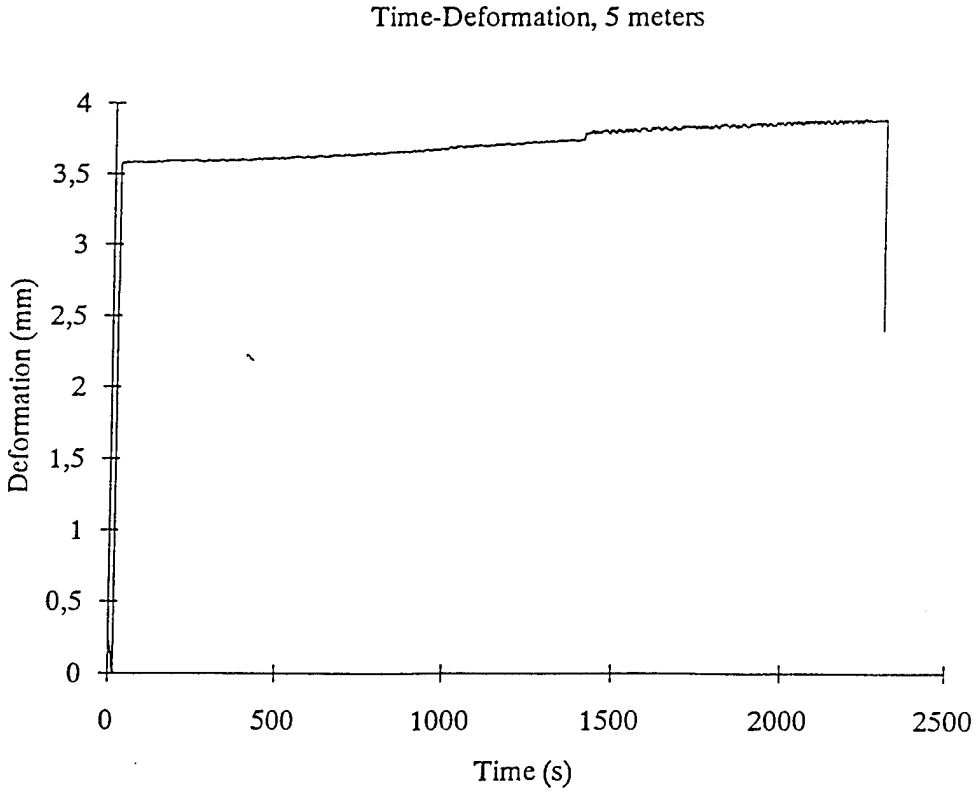

Figure 40 Time history of deformation, 5 m depth, first load increment

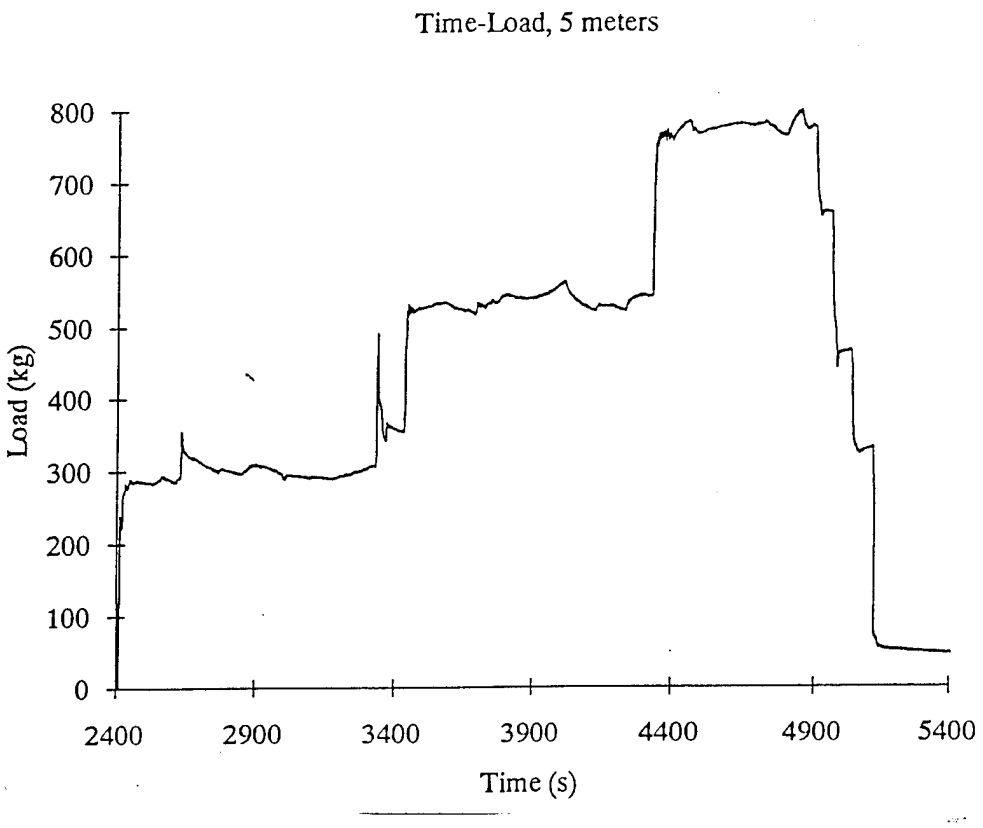

Figure 41 Time history of applied load, 5 m depth, remaining load increments

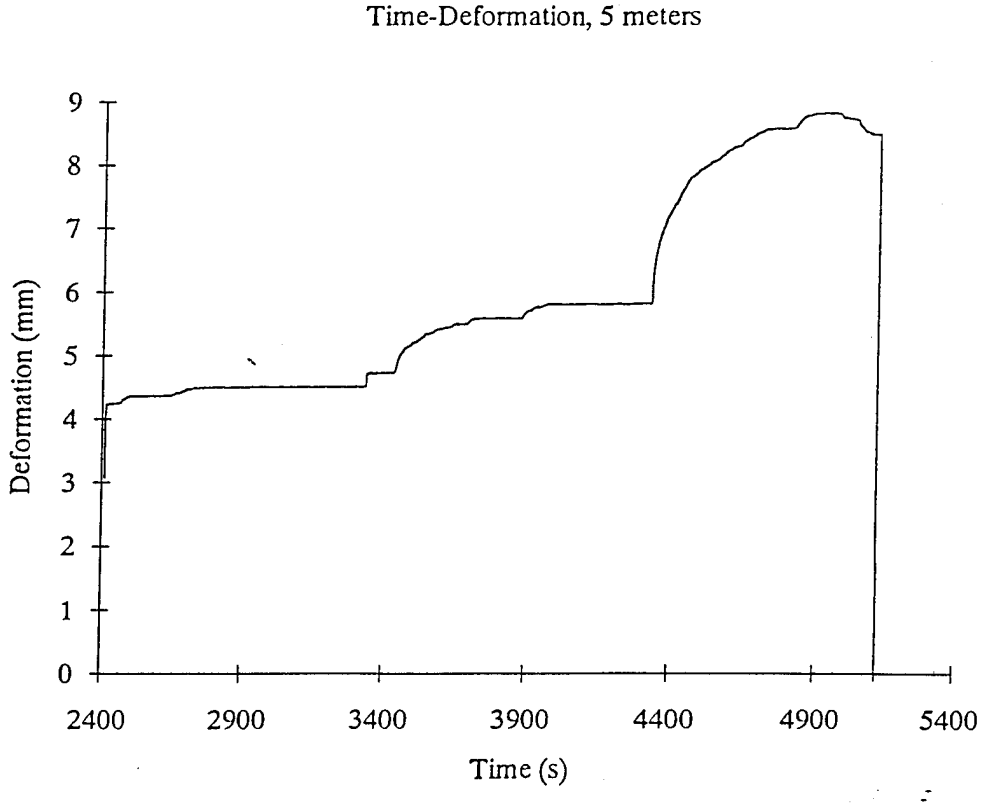

Figure 42 Time history of deformation, 5 m depth, remaining load increments

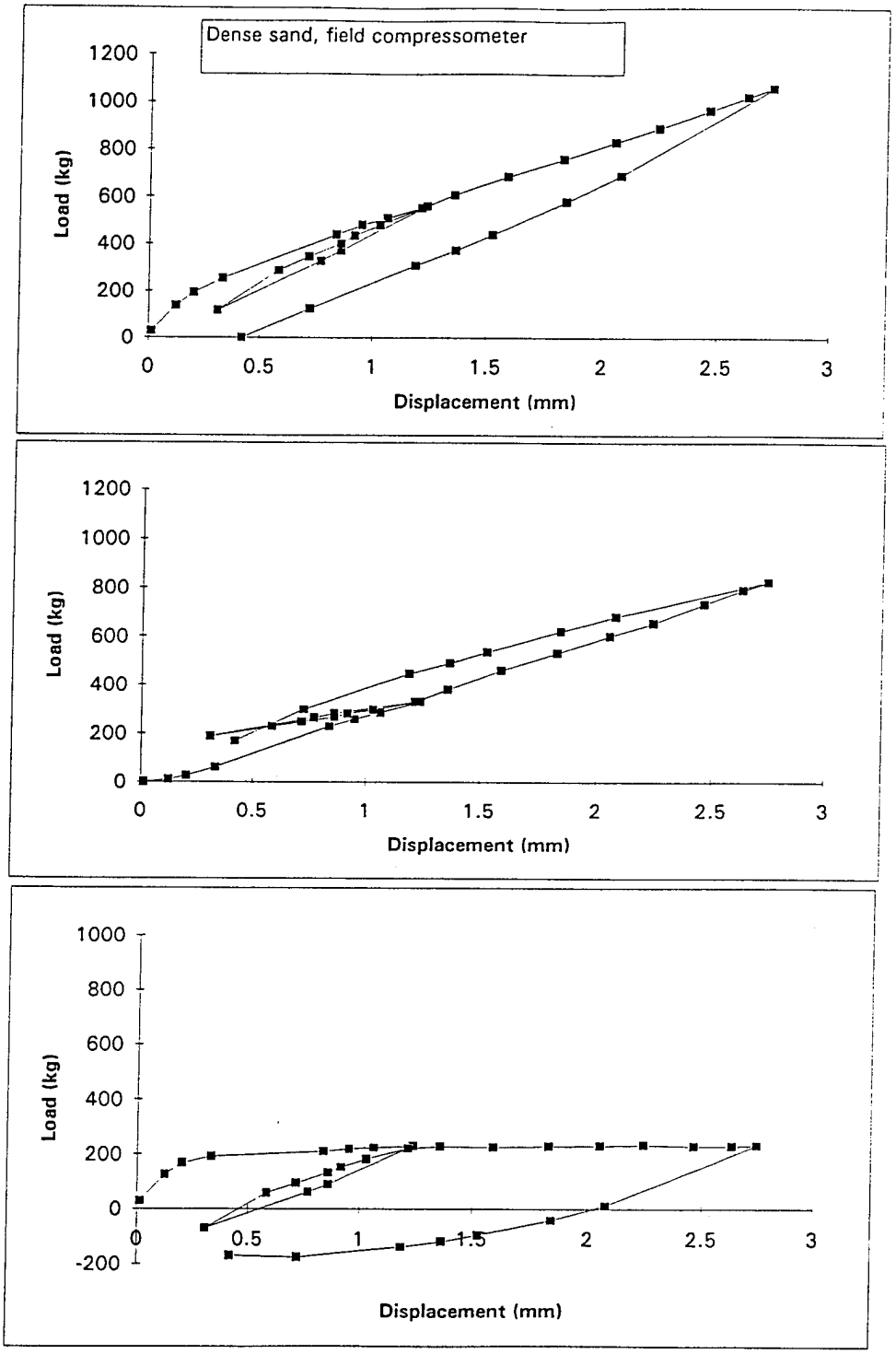

Figure 43 Friction effects in the dense sand test

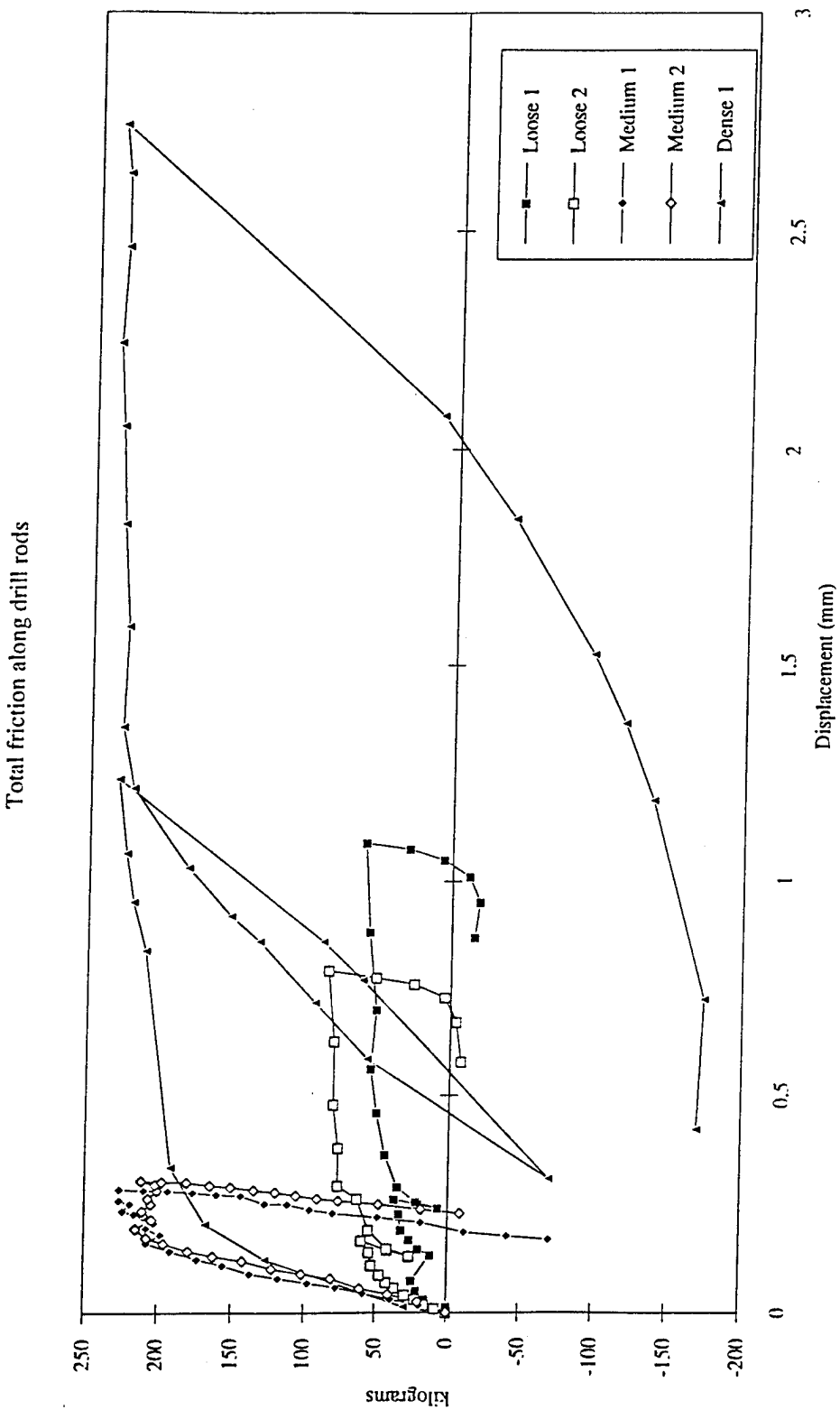

Figure 44 Friction versus deformation, all laboratory screw plate tests